SCUOLA DI DOTTORATO
UNIVERSITÀ DEGLI STUDI DI MILANO-BICOCCA

Department of Material Science

PhD program: Materials Science and Nanotechnology Cycle: XXXV

Exploiting H-ferritin nanoconjugates to improve cancer immunotherapy and drugs delivery

Surname: Barbieri Name: Linda

Registration number: 792243

Tutor: Prof. Miriam Colombo

Co-tutor: Prof. Davide Prosperi

Coordinator: Prof. Marco Bernasconi

ACADEMIC YEAR 2022/2023

Table of contents

ABSTRACT *6*

ACRONYMS *8*

GENERAL INTRODUCTION *12*

1. Cancer **12**

1.1 Brain cancer 14

1.1.1 Gliomas and glioblastoma 16

1.1.2 Therapy for glioblastoma 18

1.2 Breast cancer and triple-negative breast cancer 19

1.2.1 Breast cancer treatment 22

2. Nanotechnology **23**

2.1 Nanomedicine 25

2.1.1 *In vivo* and *in vitro* diagnostic 26

2.1.2 Regenerative medicine and tissue engineering 27

2.1.3 Drug delivery system (DDS) 28

2.2. Tumour targeting 29

2.3 Nanoparticles for cancer treatment 32

2.3.1 Ferritin 34

Structure 35

Physiological role 36

Main types of ferritin 37

Ferritin receptor 38

Ferritin as a nanovector 40
Problems regarding ferritin clinical translation 42

3. References 44

CHAPTER ONE: Evaluation of HFn-mAb nanoconjugates-mediated anticancer activity in 3D tumor models.....57

1. Introduction 58

1.1 Cancer immunotherapy 58
1.2 Cancer treatment using immunotherapy 61
1.2.1 Oncolytic viruses 62
1.2.2 Cancer vaccines 63
1.2.3 Immune checkpoint inhibitors 64
1.2.4 Adoptive cell therapy 64
1.2.5 Monoclonal Antibodies 65
Antibody-dependent cell-mediated cytotoxicity 69
Cetuximab 70
1.2.6 Immunotherapy strategies for glioblastoma and triple negative breast cancer 71
1.3 3D cultures 72

2. Aim of the project 76

3. Materials and Methods 77

4. Results 89

5. Discussion 125

6. Supporting information.....128

7. References 130

CHAPTER TWO: Cisplatin loading inside HFn: a two methods comparison 137

1. Introduction 138

1.1 Cisplatin.....138

1.2 Drug loading inside HFn 140

2. Aim of the project 143

3. Materials and methods 144

4. Results 146

5. Discussion 156

6. References 158

LIST OF PUBLICATIONS..... 161

Abstract

Cancer is a leading cause of disease worldwide and glioblastoma and triple negative breast cancer represent two types of tumors with poor prognosis and a high risk of recurrence. The therapeutic options currently in use are still subject to failure, due to (1) the poor selectivity of drugs, which compromises dose escalation to more therapeutically active levels and (2) the development of resistance by different mechanisms that cells put in place to defend themselves from the action of drugs. In this scenario, nanoparticles can be developed as new therapeutic strategies or to overcome the limitations of the treatments currently in use.

In my PhD project, I exploited the unique features of a nanoparticle based on recombinant heavy-chain ferritin cages (HFn) to improve the therapeutic treatments already available for these tumors. HFn can be a promising candidate for this study because 1) it is biocompatible; 2) it can be loaded with drugs; 3) it can be easily modified by exploiting the functional groups on its surface; 4) it exhibits tumor targeting by recognition of TfR1, overexpressed in 98% of human cancers and directly correlated with tumor stage or cancer progression; 5) HFn is able to cross the blood-brain barrier (BBB) exploiting the same TfR1 receptor, also found overexpressed on the BBB endothelial wall. My work is divided into two main subprojects, all sharing the use of HFn.

In **Chapter 1,** the functional groups present on the surface of HFn were exploited for the conjugation of the monoclonal antibody cetuximab, studying the maintenance of its anticancer activity against a 3D tumor model in comparison with unconjugated cetuximab. Cancer spheroids of glioblastoma and triple negative breast cancer were selected and produced for this study. Then we

focused on the documented ability of cetuximab to promote an indirect anticancer effect (ADCC) through the activation of immune systems cells. ADCC activation was evaluated both in live imaging and with an end-point assay monitoring the caspase production as a direct measure of cellular apoptosis. The co-incubation of cancer spheroids, HFn-mAb nanoconjugate and immune system cells showed that not only conjugated cetuximab maintained its anticancer effect but caused a higher apoptotic effect in comparison with cetuximab alone. Moreover, a preliminary biodistribution *in vivo* experiment showed a specific tumor accumulation of the nanoconjugate.

In **Chapter 2**, HFn nanocages were exploited for the encapsulation of a chemotherapeutic drug, cisplatin. We compared a pH-based and a temperature-based encapsulation strategy and, even though the encapsulation efficiency and HFn recovery seemed to be higher with the second protocol, the protein stability was compromised. This result led to the choice to use pH-encapsulated cisplatin to perform future *in vitro* cytotoxicity studies on 2D and 3D models of triple negative breast cancer.

In this project, ferritin's external surface and inner cavity were exploited to create nanoconjugates with potential anticancer effects. In the future, we also plan to co-administer HFn-mAb and cisplatin-loaded HFn in order to combine the immune system activation with the chemotherapeutic activity of this drug.

Acronyms

ADCC	Antibody-Dependent Cell-mediated Cytotoxicity
ADCs	Antibody-drug conjugates
ADCP	Antibody-dependent Cellular Phagocytosis
ACT	Adoptive Cell Therapy
ALL	Acute Lymphoblastic Leukemia
ANOVA	Analysis of variance
APCs	Antigen Presenting Cells
AuNPs	Gold nanoparticles
BBB	Blood Brain Barrier
BC	Breast cancer
BSA	Bovine Serum Albumin
CAR	Chimera Antigen Receptor
CDC	Complement-Dependent Cellular Cytotoxicity
CSF	Cerebrospinal Fluid
CISP	Cisplatin
CNS	Central Nervous System
CT	Computed tomography
CTLA-4	Cytotoxic T Lymphocyte-associated Antigen-4
CTX	Cetuximab
DCs	Dendritic cells
DDS	Drug Delivery System
DLS	Dynamic Light Scattering
DMEM	Dulbecco's Modified Eagle Medium
DOL	Degree of Labeling

DOX	Doxorubicin
E	Effector cells
ECM	Extracellular Matrix
EGFR	Epidermal Growth Factor Receptor
Epf	Epifluorescence
EPR	Enhanced Permeability and Retention
ER	Estrogen Receptor
EU	Endotoxin Unit
Fab	Variable Fraction
FBS	Fetal Bovine Serum
Fc	Constant Fraction
FDA	Food and Drug Administration
FITC	Isothiocyanate Fluorescein
FPLC	Fast Protein Liquid Chromatography
GBM	Glioblastoma Multiforme
HFn	Heavy chain Ferritin
HER-2	Human Epidermal Growth Factor Receptor 2
HPV	Human Papilloma Virus
ICIs	Immune Checkpoints Inhibitors
ICP-MS	Inductively coupled plasma-mass spectrometry
IgG	Immunoglobulin G
IL-2	Interleukin 2
IPTG	Isopropyl ß-D-1-thiogalactopyranoside
i.v.	Intravenous
LAL	Limulus Amebocyte Lysate
mAb	Monoclonal Antibody

Mal	Maleimide
MEM	Minimum Essential Medium
MGMT	Methylguanine Methyltransferase
MHC	Major Histocompatibility Complex
MDR	Multi Drug Resistance
MRI	Magnetic Resonance Imaging
NHS	N-HydroxySuccinimide
NK	Natural Killer
NPs	Nanoparticles
PD1	Programmed Cell Death Protein 1
PEG	Polyethylene glycol
PET	Positron emission tomography
PBMC	Peripheral Blood Mononuclear Cells
PBS	Phosphate Buffered Saline
pCR	Pathologic Complete Response
PR	Progesterone Receptor
Rb	Retinoblastoma
RBD	Receptor Binding Domain
Rt	Radiotherapy
RT	Room Temperature
SDS-PAGE	Sodium Dodecyl Sulphate - PolyAcrylamide Gel Electrophoresis
SEC	Size Exclusion Chromatography
T	Target cells
TCR	T Cells Receptor
TERM	Tissue Engineering and Regenerative Medicine
Tf	Transferrin

TfR1	Transferrin Receptor 1
TLR4	Toll-like receptor 4
TMZ	Temozolomide
TNBC	Triple Negative Breast Cancer
TTFields	Tumor-Treating Fields
TZ	Trastuzumab
UNTR	Untreated
VEGF	Vascular Endothelial Growth Factor
WHO	World Health Organization

General introduction

1. Cancer

A tumor is defined as any abnormal proliferation of cells, which may be either benign or malignant. A benign tumor, also called a neoplasm, remains confined to its primary location and do not invade nearby tissue or distant part of the body. Benign tumors tend to grow slowly and have distinct borders. A malignant tumor, however, is capable of both invading surrounding normal tissue and spreading to distant sites of the body via the circulatory or lymphatic systems creating the so-called metastasis. Only malignant tumors are properly referred to as cancers, and it is their ability to invade and metastasize that makes cancer so dangerous and difficult to treat.[1]

In recent years, cancer has become one of the most important health issues and the second top leading cause of mortality after heart disease.[2] According to the Global Cancer Observatory, approximately 30 million cancer patients will die from cancer each year by 2030.[3] In addition to the high mortality of cancer, the economic burden on families of cancer patients and society is enormous. Therefore, efforts on cancer prevention, diagnosis, and treatment are of great importance.[4]

The most validated hypothesis regarding cancer onset is the multistep clonal evolution by which cancer evolves starting from an initial mutation in a single normal cell that acquires selective growth advantages over other cells. As a consequence, the mutated cell starts to proliferate, accumulating genomic instability during generations.[5] Through this process, cancer cells acquire some new biological features that enable them to become tumorigenic and

malignant. The characteristics that distinguished a cancer cell from a normal one are known as hallmarks of cancer and, over the years, they were used as targets to develop anticancer drugs (Fig1). These features include sustaining proliferative signaling, evading growth suppressors, resisting cell death, enabling replicative immortality, inducing angiogenesis, activating invasion, metastasis, energy metabolism reprogramming and evading immune surveillance.[6] A deep understanding of all these cancer hallmarks could help in the development of new pharmacological treatments.

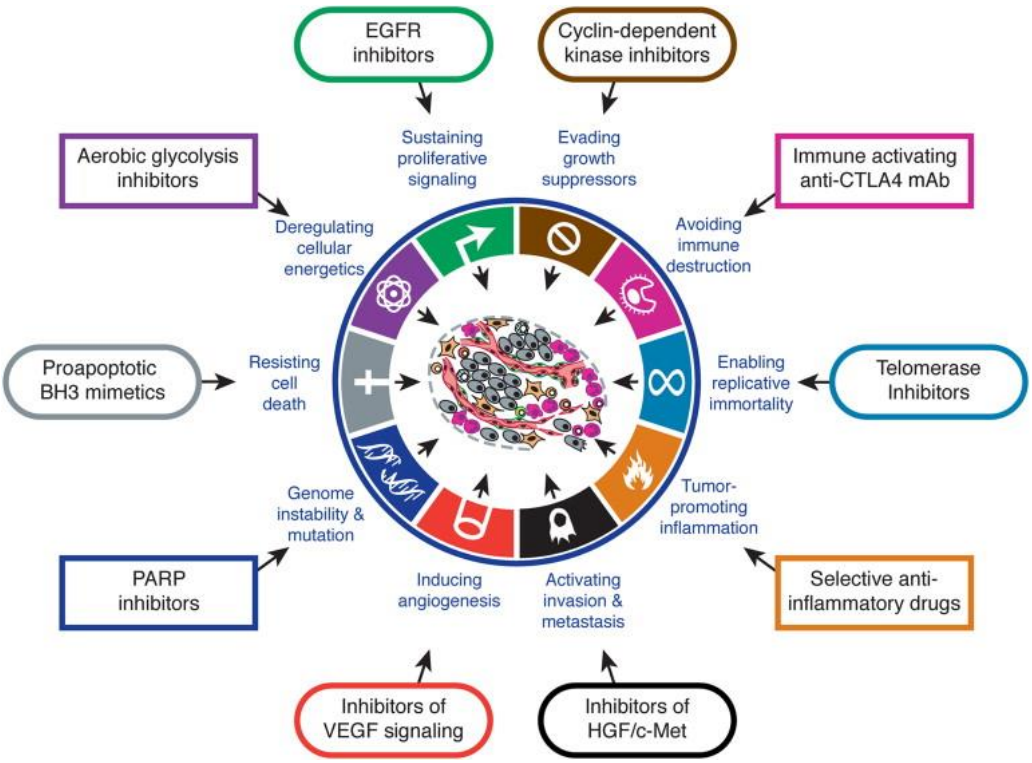

Figure 1: Cancer hallmarks and target elements for therapy. Scheme of all the modifications involved in cancer onset and progression and drugs that have been developed to target each of them. Reproduced with permission from the corresponding paper.[6]

1.1 Brain cancer

Malignant and non-malignant brain and other central nervous system (CNS) tumors comprise over 100 histologically distinct subtypes with varying descriptive epidemiology, clinical characteristics, treatments, and outcomes.[7] Broadly, brain tumours can be divided into two categories: primary brain tumors derived from cells intrinsic to the central nervous system and metastases derived from extracranial sites. Malignant gliomas, including glioblastomas, represent approximately 30% of primary brain tumors (Fig2). Although primary malignant brain tumors are rare (approximately 2% of all cancers in adults), they have a high fatality rate: only one-third of individuals survive at least 5 years after diagnosis.[8,9] The remaining 70% of primary brain tumors are non-malignant, the most common of which is meningioma, which has the potential to become malignant. Brain metastases from extracranial sites, including lung, breast, and melanoma, are more common than primary brain tumors, with increasing frequency over time in part due to increased survival after diagnosis, active CNS surveillance in patients with cancer and advances in diagnostic imaging modalities.[10] The exact incidence of brain metastases is unknown even though various studies put it around 9.6% of all cancers.[11,12]

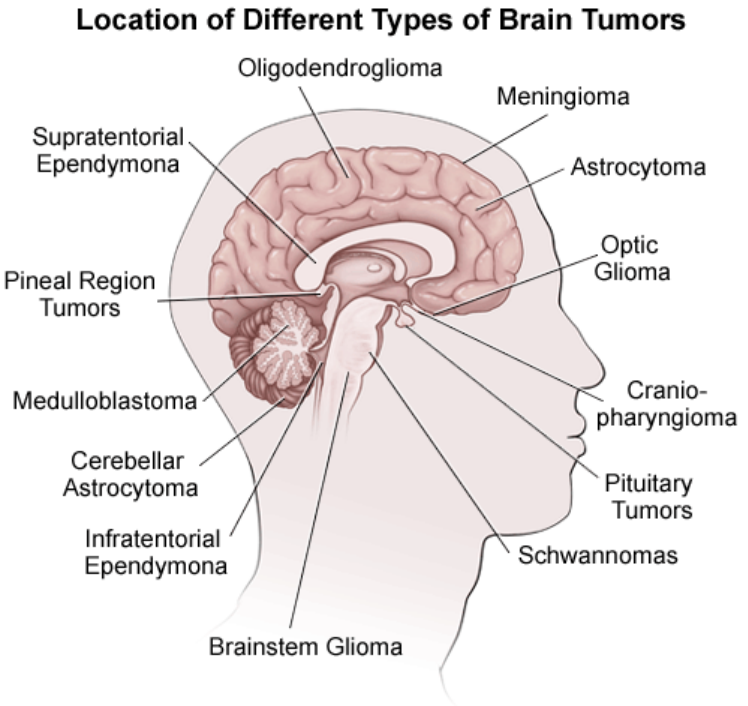

Figure 2: Primary brain tumors. Illustration of the most common primary brain tumors with an indication of their origin. Reproduced with permission from the corresponding paper.[13]

Brain tumors are classified according to the World Health Organization (WHO) CNS tumors system introduced in 2016. This classification incorporates signature molecular genetic alterations to the classic histology. This combined phenotypic and genotypic classification generated new integrated diagnoses, where the histopathological name is followed by the genetic features (e.g., glioblastoma, IDH-wildtype). Moreover, WHO grade determination is still made on the basis of histologic criteria: grades ranging from I to IV, where I is the least aggressive and IV the most aggressive (Fig3).[14,15]

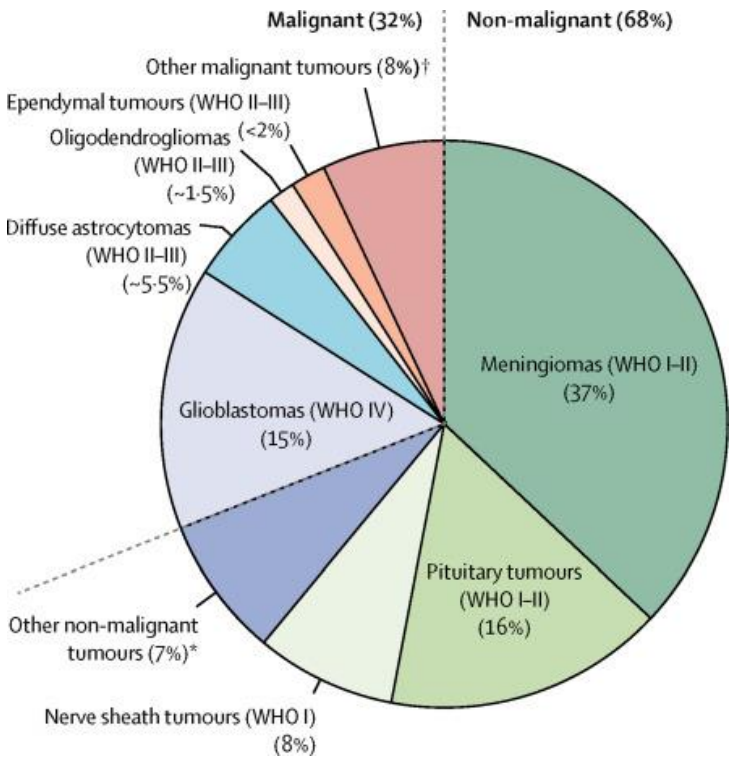

Figure 3: Simplified representation of yearly incidence of primary brain tumors among adults from 2010–2014 and its WHO classification. Reproduced with permission from the corresponding paper.[15]

1.1.1 Gliomas and glioblastoma

Gliomas are tumors of neuroectodermal origin arising from glial or precursor cells and account for almost 80% of all malignant primary brain tumors in adults.[15] The vast majority of glial neoplasms in adult patients are diffuse gliomas. Such gliomas are characterized by diffusely infiltrative growth within the CNS parenchyma.[16] Gliomas are classified as ependymomas, astrocytomas (including glioblastoma [GBM]), oligodendrogliomas, mixed gliomas, and a few others, such as optic nerve and brain stem gliomas.[17] The WHO classification

system groups gliomas into 4 histological grades defined by increasing degrees of undifferentiation, anaplasia, and aggressiveness.[18] In the last classification, the diffuse gliomas included the grade II and III astrocytic tumors, the grade II and III oligodendrogliomas, the grade IV glioblastomas, as well as the related diffuse gliomas of childhood.[14]

Glioblastoma is the most malignant and frequently occurring type of primary glioma and is characterized histologically by considerable cellularity and mitotic activity, vascular proliferation, and necrosis.[18] Although GBM is a rare tumor with a global incidence of less than 10 per 100,000 people, its poor prognosis with a survival rate of 14-15 months after diagnosis makes it a crucial public health issue.[19]

GBM is genetically and transcriptionally heterogeneous, but previous studies have demonstrated concordant genetic alterations. These mutations represent a set of deregulated signaling pathways, including growth factor (receptor tyrosine kinase [RTK]/phosphatidylinositide 3-kinase [PI3K]/Ras), p53, and retinoblastoma (Rb) signaling pathways. In the growth factor signaling pathway, EGFR is frequently activated with variant III deletion of the extracellular domain in GBM.[20] The majority of GBM tumors have genetic alterations in all three pathways, which help to fuel cell proliferation and enhance cell survival while allowing the tumor cell to escape from cell-cycle checkpoints, senescence, and apoptosis.[21] GMB is also cellular heterogeneous and, among the different tumoral cell populations, the glioma stem cells are thought to contribute the most to tumor spreading, invasion, proliferation, and maintenance seeming to be responsible for cancer chemo-radio resistance.[22]

1.1.2 Therapy for glioblastoma

Major challenges in therapy of GBM are associated with the location of the disease, with its complex and heterogeneous biology, and also with the failure of many chemotherapeutics drugs to cross the blood-brain barrier. All these characteristics prevent the possibility to find a unique standard therapy for all the patients thus determining the need for a multidisciplinary approach.[23] Current standard therapy includes maximal safe surgical resection, followed by concurrent radiotherapy (Rt) with temozolomide (TMZ) (Temodar®), an oral alkylating chemotherapy agent, and then adjuvant chemotherapy with TMZ.[24] The extent of surgical resection carries prognostic value: one-year survival is significantly higher for patients with more than 90% tumor resection compared to those with less than 90% tumor resection.[25] However, extensive and complete surgical resection of GBM is difficult because these tumors are highly diffusive, invasive and vascularized. Moreover, they are often located in eloquent areas of the brain, including areas that control speech, motor function, and the senses. Because of the high degree of invasiveness, radical resection of the primary tumor mass is not curative, and infiltrating tumor cells invariably remain within the surrounding brain, leading to later disease progression or recurrence.[26] After surgery, since a phase III clinical trial carried out in 2005, patients are treated with a combination of Rt and temozolomide. Even if the median survival of patients who received TMZ plus Rt is extended to 14.6 months versus 12.1 months with Rt alone, it is now well-known that response to alkylating therapy with temozolomide differs among patients with the same histological diagnosis of GBM and depends on the methylation of the methylguanine methyltransferase (MGMT) promoter. Hegi et al. (2005) showed that patients with methylated MGMT not only have a better prognosis but also

respond better to alkylator therapy. However, despite maximal initial resection and multimodality therapy, recurrence is expected to appear in the majority of cases.[23–27] In 2009 the U.S. Food and Drug Administration (FDA) approved the anti-vascular endothelial growth factor (VEGF) antibody bevacizumab for the treatment of recurrent glioblastoma on the basis of two phase II studies showing a progression-free survival benefit. However, two phase III clinical trials evaluating its role in the treatment of newly diagnosed disease did not demonstrate an overall survival benefit when bevacizumab was added to standard therapy.[28] Recently with the introduction of the tumor-treating fields (TTFields) approach, median overall survival has increased to 20.9 months after surgery. TTFields is an innovative technology that delivers low-intensity, intermediate-frequency alternating electrical fields to tumor cells thus interrupting cell division and causing apoptosis.[29] Nevertheless, recurrence is expected in 90% of cases within 12 months after diagnosis.[22]

1.2 Breast cancer and triple-negative breast cancer

Breast cancer (BC) is the most frequent malignancy in women worldwide and it is so common that alone accounts for 25% of all cancers in females.[30] BC remains curable in almost 70–80% of patients with early-stage cancer that is contained in the breast or that has only spread to the axillary lymph nodes. By contrast, the advanced (metastatic) disease is not considered curable using currently available therapeutic options whose main goals remain to prolong survival and control symptoms.[30]

From a molecular point of view, breast cancer is universally considered a very heterogeneous disease characterized by different histopathological and biological features that necessarily lead to different clinical outcomes.

Molecular dissimilarities can occur either between different patients with the same tumor type (intertumor heterogeneity), or within the same patient (intratumor heterogeneity).[31,32] Because of this heterogeneity both in morphological features and in clinical behavior, different classification systems exist. Histological classification categorized BC considering both the site of origin (ducts or lobules) and the invasiveness pattern (non-invasive/in situ or invasive/infiltrating) (Fig4).

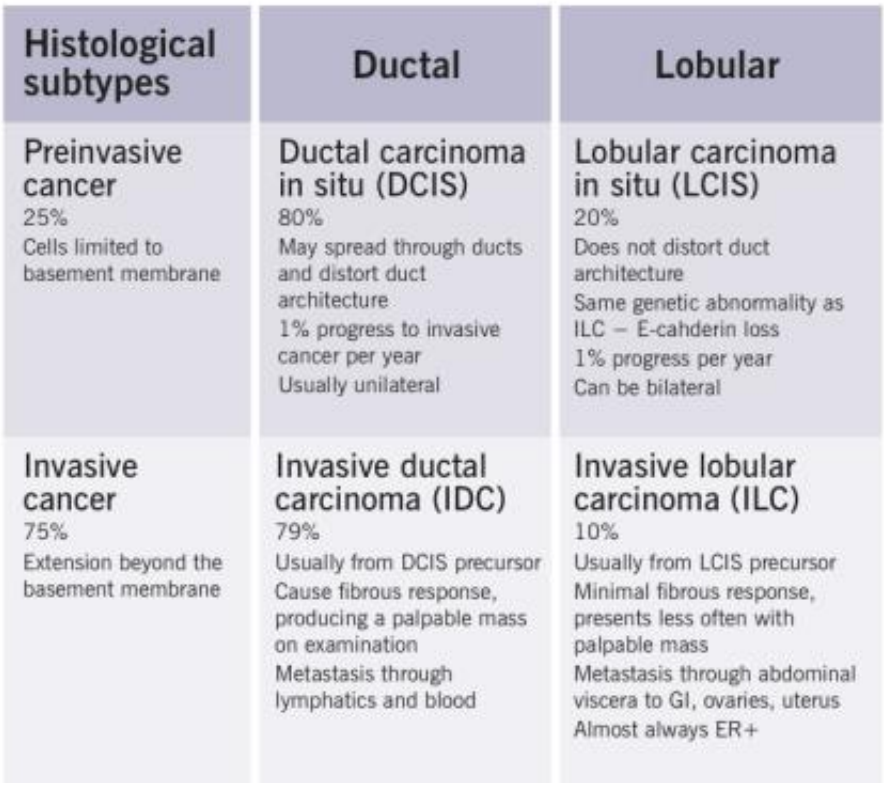

Figure 4: Histological classification of breast cancers. Reproduced with permission from the corresponding paper. [33]

From a molecular point of view five different subtypes can be distinguished: basal-like (triple-negative breast cancers), HER2-enriched, luminal A, luminal B

and normal-like. This classification is mainly based on the expression of specific molecular markers, including estrogen receptor (ER), progesterone receptor (PR) and human epidermal growth factor receptor 2 (HER2) (Fig5).[34]

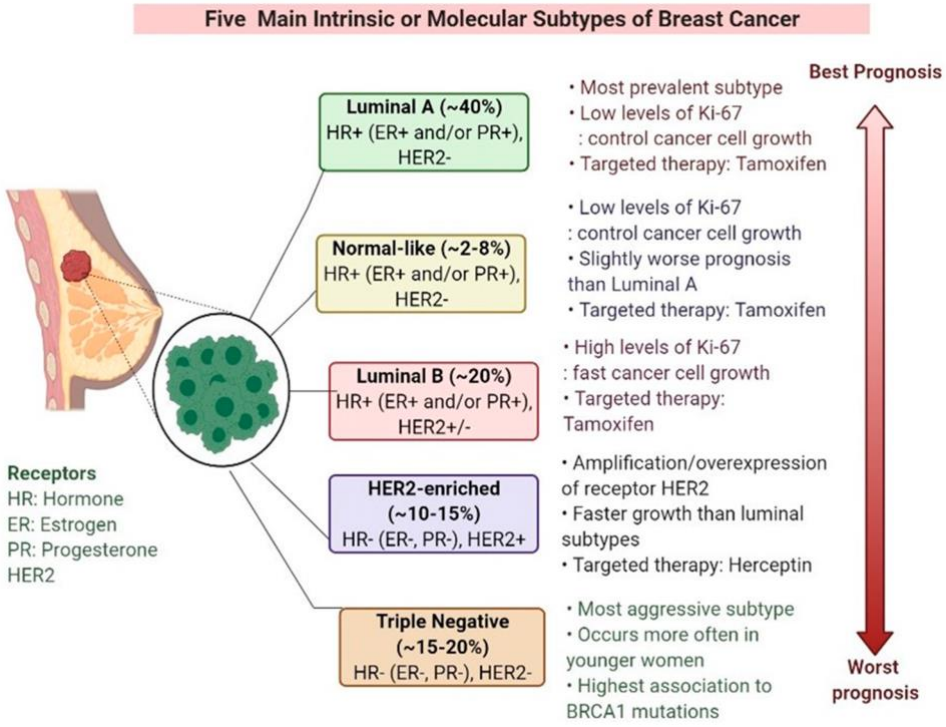

Figure 5: Molecular classification of breast cancer. Reproduced with permission from the corresponding paper.[35]

The highest mortality rate associated with breast cancer has been observed in **triple-negative breast cancers** (TNBC) which account for 15%-20% of all breast cancer cases. TNBC is characterized by a high histological grade and proliferation rate and it is associated with a lack of ER, PR, and HER2 expression. Furthermore, the tumor suppressor gene p53 and several DNA repair genes, particularly the BRCA genes, are either mutated or abnormally expressed in TNBC. Clinically, TNBC tends to act more violently than other types of breast cancer and is

characterized by a high risk of relapse, short progression-free survival and overall survival.[35,36]

1.2.1 Breast cancer treatment

The great heterogeneity of BC is also reflected in the choice of therapeutic strategy that can include surgery, radiation, chemotherapy, and other treatments. The primary mean of local and regional breast cancer treatment remains surgical intervention which involves breast-conserving surgery or mastectomy.[37] Following surgery, the next step in managing early-stage breast cancer is to lower the risk of recurrence and to get rid of any remaining cancer cells which are undetectable but responsible for both local and distant recurrence of cancer. Treatment given after surgery is called adjuvant therapy and may include radiation therapy, chemotherapy, targeted therapy, and/or hormonal therapy.[38] The same treatments may be given when surgery is not possible or in case of a metastatic breast cancer recurrence. Focusing on hormonal therapy, standard adjuvant endocrine therapy for luminal and normal-like BC is based on Tamoxifen which over the years has led to a 40-50% reduction of the 10-year recurrence risk.[39] Furthermore HER2+ breast cancer patients respond very well to treatment with Trastuzumab (TZ), a monoclonal antibody that binds to the receptor avoiding its activation.[40] Regarding TNBC, chemotherapy is currently the only systemic treatment option. Taxane and anthracycline-based regimens represent the standard care in TNBC therapy, while platinum-based chemotherapy has shown promising results in the neoadjuvant and metastatic settings.[35] Despite the aggressive nature of TNBC, 20% of patients present a pathologic complete response (pCR) after neoadjuvant chemotherapy. However, patients that did not achieve pCR suffer

an early recurrence which usually determines also the development of visceral and brain metastases.[41] The differences in clinical outcomes following adjuvant treatment imply that a subset of TNBCs is sensitive to chemotherapy while the majority become resistant during treatment or are intrinsically less susceptible.[42] To improve therapeutic benefits in TNBC treatment, various agents have been explored in clinical studies. They include immuno- and targeted therapies in the networks of tumor stroma, DNA damage response, cell surface or intracellular receptors, and signaling pathways as well as cell surface markers for selective drug delivery, and antibody-drug conjugates.[41]

2. Nanotechnology

Nanotechnology is a multidisciplinary field of research and innovation that deals with materials at the atomic and molecular levels. In particular, according to the US National Nanotechnology Initiative, nanotechnology is specifically related to the understanding and control of matter at a length scale of approximately 1–100 nanometers.[43] The concept of "nanotechnology" was introduced in 1959 at the American Physical Society meeting by the American physicist Richard Feynman during his famous lecture entitled "There's plenty of room at the bottom". With his speech Feynman raised the possibility of manipulating matter on the small-scale, interfering with the biological system at the atomic level.[44] Interestingly the term nanotechnology was coined in 1974 by Professor Norio Taniguchi. "*Nanotechnology* – he said – *mainly consists of the processing of separation, consolidation, and deformation of materials by one atom or one molecule*".[45]

In 2004 the Royal Society and Royal Academy of Engineering defined nanoscience and nanotechnologies in this way: "*Nanoscience is the study of phenomena and manipulation of materials at atomic, molecular and macromolecular scales, where properties differ significantly from those at a larger scale*" and "*Nanotechnologies are the design, characterization, production and application of structures, devices and systems by controlling shape and size at nanometer scale*".[46] In fact, at the nanometric level materials have peculiar physical properties that differ from those of the same material at a larger size (Fig5). Moreover, this is also the typical range size of biological molecules: atoms are below a nanometer in size, whereas many molecules, including some proteins, range from a nanometer upwards.

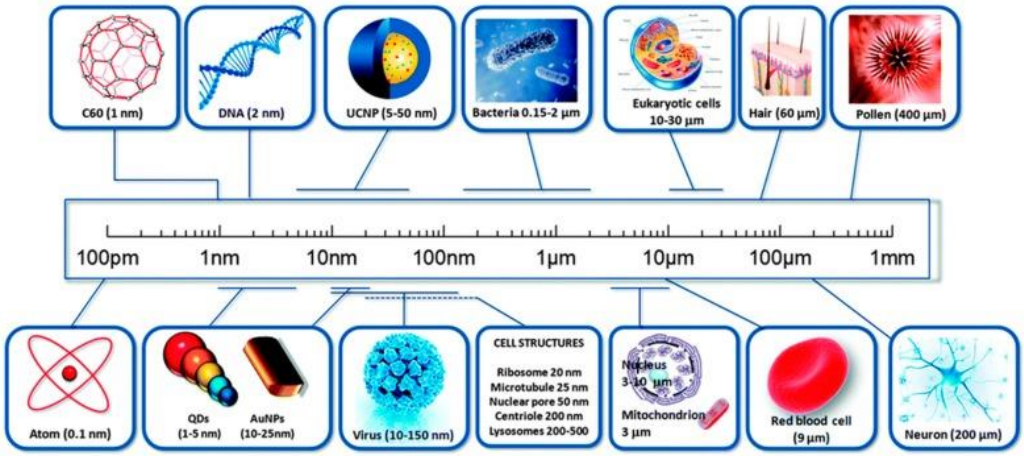

Figure 5: A comparison of sizes of nanomaterial. Reproduced with permission from the corresponding paper.[45]

Nanoparticles (NPs) have distinctive size-dependent properties which are mainly due to their high surface-to-volume ratio. As a particle decreases in size, a greater proportion of atoms are found at the surface compared to that inside.

This increased surface-to-volume ratio is very important in biological systems because it results in an improvement in the chemical reactivity of NPs with molecular targets along with an increase in the surface area available for functionalization. Moreover, the behavior of matter at the nano-level is dominated by the quantum effect, which affects the optical, electrical, and magnetic properties of nanoparticles.[47,48]

During the last decade, nanotechnology gained a lot of interest involving different research fields such as electronics, transportation, energy and environment, spatial exploration, cosmetics, and even medicine.[49]

2.1 Nanomedicine

Nanomedicine can be defined as the design and development of therapeutics and/or diagnostic agents in the nanoscale range, with the possibility, by moving within biological systems, to transport and deliver a variety of biomedical entities for treatment, prevention, and diagnosis of many diseases.[50] Nanoparticles, due to their small size, may cross biological barriers and specifically interact with target molecules at the sub-cellular scale and, for example, release locally a therapeutic drug.[51] NPs could be exploited also for the diagnosis of a certain disease thus becoming *theranostic* agents. In fact, nanomedicine aims to offer new approaches to *Find, Fight* and *Follow* a certain disease which means detection, therapy and monitoring which represent the stages of early diagnosis, medicine and therapy control.[52]

Furthermore, nanotechnologies have been exploited to overcome lots of medicine's limitations, especially in cancer treatment. Indeed, conventional therapies (surgery, radiation and chemotherapies) are often effective in

reducing tumor mass, but they usually have systemic toxicities and side effects due to their nonselective nature which causes damage also to healthy cells. Moreover, nanomedicine, through the intervention on a single cell, could help to recognize and detect a tumor before the angiogenic switch and so under the current threshold for clinical detection.[53,54]

2.1.1 *In vivo* and *in vitro* diagnostic

A key focus in nanomedicine involves the use of nanomaterials as contrast agents for anatomical and functional imaging. Nanoparticles possess certain size-dependent properties, particularly with respect to optical and magnetic parameters, which can be manipulated to achieve a detectable signal. Moreover, NPs can be engineered to localize in specific tissues. For all these reasons different categories of NPs have been tested in imaging techniques such as computed tomography (CT), magnetic resonance imaging (MRI), and positron emission tomography (PET) in order to obtain more clear images and try to detect even single cancer cells.

Due to their intrinsic properties, magnetic nanoparticles have been largely studied as MRI contrast agents. Thanks to their low toxicity profile, several of these nanoformulations have been approved for clinical applications. Most of them are superparamagnetic iron oxide nanoparticles (SPION) coated with different ligands. One example is Resovist®, a liver-specific MRI contrast agent made by SPION coated with carboxydextran.[55] Ongoing studies aim at increasing targeting specificity by adding bioactive molecules to the SPION surface.[56]

Nanoparticles can also be coated with ligands to enable the biorecognition of certain substances in the bloodstream or the identification of specific cells inside the body, thus becoming nanosensors.

2.1.2 Regenerative medicine and tissue engineering

Due to many drawbacks of tissue and organ transplantation such as limited donor availability, the need for immunosuppression and insufficient success rate (rejection of the transplant), there is an increasing demand for tissue engineering and regenerative medicine (TERM) solutions.[57] The use of scaffolds, biomaterials synthesized with natural or semisynthetic polymer with the aim to mimic the extracellular matrix (ECM) and thus foster cell function and tissue growth, is one of the leading research areas in tissue engineering. NPs can be incorporated into those scaffolds to facilitate tissue regeneration through their dimension and biomimetic composition. Moreover, nanomaterials can be tuned to reproduce the complexity and functionality of a native EMC at a nanoscale which is fundamental to providing cell support and releasing a wide variety of soluble factors for the cell-cell interactions in a tissue.[58] For example, gold nanoparticles have been incorporated into scaffolds and have shown promising features to improve biomaterials' mechanical properties as well as to promote cell proliferation and differentiation (Fig6). Moreover, it has been shown that they can also improve electrical communication between cardiac cells.[57,59]

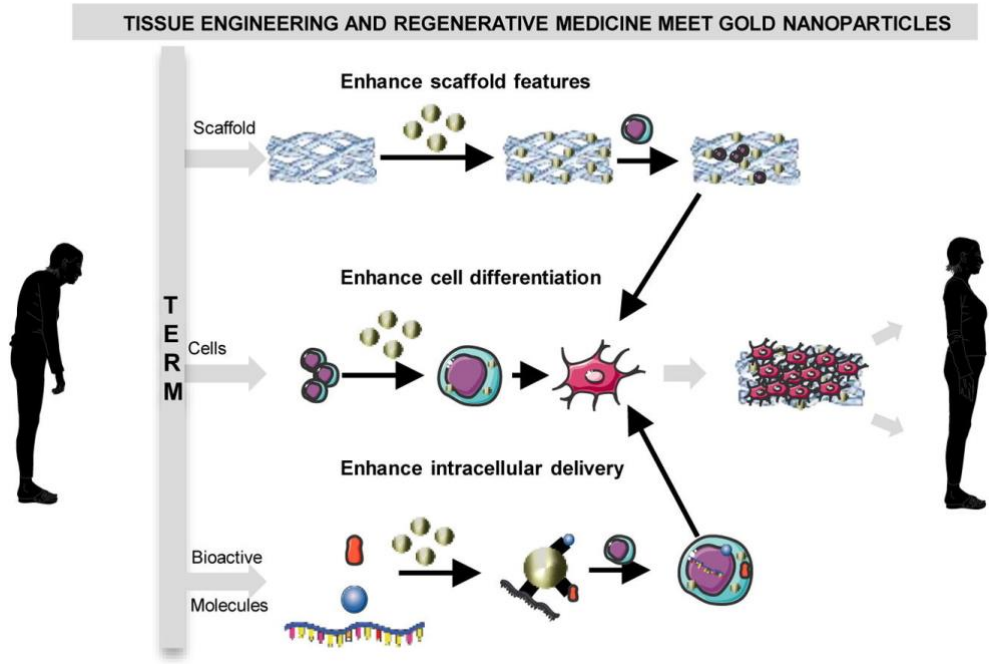

Figure 6: Scheme representing the importance of introducing gold nanoparticles (AuNPs) in TERM. TERM combines three elements: scaffold, cells and bioactive molecules for engineered or repaired tissue. The addition of AuNPs in each element aims to enhance scaffold features (mechanical, adhesive), cell differentiation and intracellular delivery of bioactive molecules in order to bring an ideal microenvironment for the regeneration of the damaged tissue. Reproduced with permission from the corresponding paper.[59]

2.1.3 Drug delivery system (DDS)

A drug delivery system (DDS) comprises the administration and delivery of pharmaceutical compounds, such as therapeutic drugs, to a specific area in the body, thus minimizing its side effects on healthy tissues.[60] In addition, DDS protects the carrier from rapid degradation or clearance and enhances drug concentration in target tissues, therefore, lower doses of the drug are required.

Several nanomaterials such as liposomes, polymers, dendrimers, magnetic and protein-based nanoparticles are used as carriers for drug delivery. To effectively deliver drugs to the targeted tumor tissue, nanoparticles must have the ability to remain in the bloodstream for a considerable time without being eliminated. The fate of injected nanoparticles can be controlled by adjusting their size and surface characteristics. In fact, the size of a nanoparticle used as DDS should be large enough to prevent their rapid leakage into blood capillaries and renal clearance but small enough to escape capture by macrophages that are lodged in the reticuloendothelial system. Regarding the surface, NPs should have a hydrophilic one to escape macrophage capture.[61,62] The justification for the use of nanoparticles as DDS lies in at least three mechanisms: Enhanced Permeability and Retention (EPR) of nanoparticles in solid tumors; the possibility of transporting insoluble drugs in the blood through stable colloidal systems and the controlled release thereof.[63,64] Exploiting all these characteristics, NPs can improve the pharmacokinetic profile of some classic medicines making them more effective, increasing patient compliance, and reducing healthcare costs and side effects.[60]

2.2. Tumor targeting

The idea of targeted therapy was first introduced by Paul Erlich in the first 1900s, with the so-called “magic bullet concept”. He described a hypothetical drug capable to go straight to its intended cell targets, thus efficiently killing pathogens without affecting healthy cells. NPs and nanotechnologies in general can be tuned to obtain all these characteristics and bring a high payload of a drug to the site of interest, thus reducing side effects and extending the maximal

allowable dose.[65] There are two main strategies by which targeting can be achieved, namely passive and active targeting.

Passive targeting describes the accumulation of a drug or drug-carrier system into the tumor tissue via a biological mechanism known as EPR (Fig7). This effect was first described in 1986 by Matsumura and Maeda: they observed that the anticancer protein neocarzinostatin, conjugated to a polymeric matrix, exhibited greater accumulation in tumor tissues than free neocarzinostatin.[66,67] This accumulation is based on anatomical differences between healthy and tumor vasculature. Fast-growing cancer cells have an increasing need for nutrients and oxygen which leads to the development of leaky vessels characterized by high disorganization, dilated with numerous pores, enlarged gap junctions between endothelial cells, and compromised lymphatic drainage.[61,62,65] Together with nutrients, these pores allow the extravasation and accumulation of nanoparticles with sizes of up to 400 nm in the tumor interstitial space. From the moment of its discovery, EPR effect was validated and became the pillar of the research in cancer nanomedicine. However, when this strategy was put to the utmost test of clinical trials, many nano-based formulations failed to produce the promised tumor accumulations especially because EPR effect is not common in all tumors and there are many large tumors cases displaying a high degree of pathophysiological heterogeneity, which limits the penetration of nanoparticles. Moreover, the random nature of EPR effect makes it difficult to control the process and can result in the onset of multiple-drug resistance (MDR) mechanisms.[66,67]

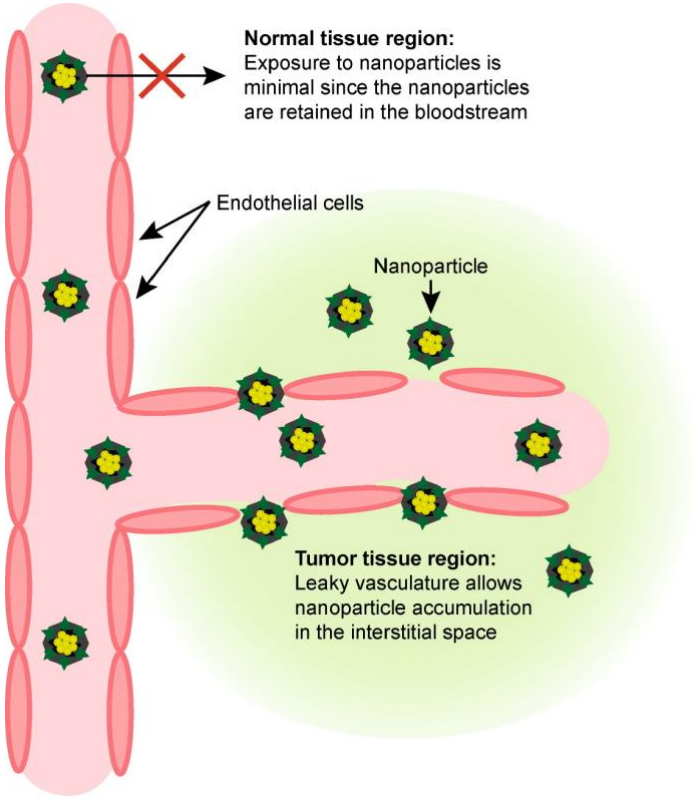

Figure 7: Schematic representation of the EPR effect. Normal tissue vasculatures are lined by tight endothelial cells, thereby preventing nanoparticle drugs from escaping or extravasation, whereas tumor tissue vasculatures are leaking and hyperpermeable allowing preferential accumulation of nanoparticles in the tumor interstitial space. Reproduced with permission from the corresponding paper.[68]

On the other side, to guarantee that the transported drug is effectively internalized by cancer cells, **active targeting** can be exploited. It is based on the conjugation of targeting moieties (such as ligands, peptides or antibodies) on the surface of nanocarriers for the crossing of biological barriers, specific tumor homing, increased retention at the target site, and internalization in cancer cells by triggering receptor-mediated endocytosis.[69] Moreover, since glycoproteins

cannot remove polymer-drug conjugates that have entered the cells via endocytosis, this active targeting mechanism provides an alternative route for overcoming multiple-drug resistance.[68] For this mechanism to be selective and successful some factors must be considered: first, to minimize or avoid off-target effects of the transported agent on healthy tissue, the antigen chosen as a target should be expressed exclusively and also homogeneously on tumor cells; second, the presence of protein corona adsorbed on the surface of the nanoparticle should not prevent the recognition between the receptor and the targeting moiety.[70] Even if the number of available targeting ligands is very high and can be potentially tailored to each disease, active targeting technologies have resulted in few clinically validated products. This result could be related to the extreme heterogeneity of tumors which requires the development of a new class of NPs bearing versatile moieties or different ligands simultaneously in other to obtain a complete response to therapy.[65]

2.3 Nanoparticles for cancer treatment

Cancer remains the second leading threat to human survival in the world and it was responsible for an anticipated 9.6 million deaths in 2018.[71] Over the past few decades, major advances in the knowledge about the molecular biology and cellular basis of cancer have been made. However, translating this understanding into clinically useful therapeutic options is still a challenge. The main reasons behind the failure of lots of pharmacological strategies include dose-limiting toxicity, poor specificity towards tumor cells or tissues, and induction of drug resistance. Nanotechnologies can play a role in enhancing the

efficient delivery of the anticancer drug to the affected tissues by increasing efficacy and reducing the side effects.[72,73]

Nanoparticles currently tested for cancer diagnosis and therapy belong to the inorganic or organic category. In the first category, there are iron oxide, gold, silica NPs and quantum dots which are mainly used for imaging and thermal ablation purposes; polymeric NPs, liposomes, dendrimers, micelles and protein-based NPs belong to the second category and they are mainly used as DDS but also for vaccine development.[74]

In 1995, Doxil® (liposomal doxorubicin) became the first nanoparticle-based drug for cancer treatment to receive clinical approval in the United States. Since then, other liposomal formulations entered the clinic such as Vyxeos™, made by liposomal daunorubicin and cytarabine, which received FDA approval in 2017 for therapy-related acute myeloid leukemia. Interestingly, all the formulations approved to date are made of liposomes with the exception of Abraxane® (albumin-bound paclitaxel nanoparticle) approved for lung, breast and pancreatic cancer, and NanoTherm®, an iron oxide nanoparticles formulation approved only in Europe to treat glioblastoma (Table 1).[66,74,75]

Table 1: Nanomedicines approved for the treatment of various cancers. Reproduced with permission from the corresponding paper.[66]

Number	Name	Drug	Nanoparticle type	Approval	Indication	Ref.
Cancer						
1	Vyxeos™	Daunorubicin + cytarabine	Liposome	FDA (2017)	Newly diagnosed t-AML or AML-MRC	[15]
2	Onivyde®	Irinotecan	PEGylated liposome	FDA (2015)	Post gemcitabine metastatic pancreatic cancer	[16]
3	NanoTherm®	Iron Oxide	Iron oxide NP	Europe (2012)	Glioblastoma	[17]
4	Marqibo®	Vincristine sulfate	Liposome	FDA (2012)	Acute lymphoid leukemia	[18]
5	Genexol-PM®	Paclitaxel	Polymeric micelle	South-Korea (2007)	NSCLC, breast and ovarian cancers	[19]
6	Abraxane®	Paclitaxel	Albumin NP	FDA (2005)	Breast, lung and pancreatic cancers	[20]
7	Eligard®	Leuprolide acetate	Polymeric nanoparticle	FDA (2002)	Advanced prostate cancer	[21]
8	Myocet®	Doxorubicin	Liposome	Europe (2000) Canada (2001)	Metastatic breast cancer	[22]
9	Mepact®	Mifamurtide	Liposome	Europe (2000)	Non-metastatic resectable osteosarcoma	[23]
10	Depocyt®	Cytarabine	Liposome	FDA (1999)	Lymphomatous malignant meningites	[24]
11	Lipo-Dox®	Doxorubicin	PEGylated liposome	Taiwan (1998)	Kaposi sarcoma, ovarian and breast cancers	[25]
12	DaunoXome®	Daunorubicin	Liposome	FDA (1996)	HIV-related kaposi sarcoma	[26]
13	Doxil®	Doxorubicin	PEGylated liposome	FDA (1995)	Ovarian cancer, multiple myeloma, HIV-related Kaposi's sarcoma	[27]
14	Oncaspar®	L-asparaginase	PEGylated protein conjugate	FDA (1994)	Acute lymphoblastic leukemia	[28]
15	SMANCS	Neocarzinostatin	Polymeric conjugate	Japan (1993)	Liver and renal cancers	[29]
Diagnostic						
16	Resovist®	SPION coated with carboxydextran	Superparamagnetic iron oxide NP	Europe (2001) Japan (2002)	Imaging agent (MRI)	[30]
17	Feridex®	SPION coated with dextran	Superparamagnetic iron oxide NP	FDA (1996)	Imaging agent (MRI)	[30]
18	GastroMark™	SPION coated with silicone	Superparamagnetic iron oxide NP	FDA (1996)	Imaging agent (MRI)	[31]

AML-MRC: AML with myelodysplasia-related change; NP: Nanoparticle; NSCLC: Non-small-cell lung cancer; SMANCS: Styrene co-maleic acid conjugated NeoCarzinoStatin; SPION: Superparamagnetic iron oxide nanoparticles; t-AML: Therapy-related acute myeloid leukemia.

2.3.1 Ferritin

Among all classes of biological nanoparticles, we focused on ferritin which is a globular protein present in the majority of living species due to its fundamental role in iron metabolism. It was discovered and named in 1937, more than 80 years ago, by Laufberger who isolated ferritin from the horse spleen.[76] It is ubiquitously expressed in archaea, eubacteria, plants, invertebrates and mammals, with the only notable exception of yeasts.[77]

Mammalian ferritin is mainly present intracellularly in the cytosol, as well as in the nucleus and mitochondria, while extracellular ferritin is found in serum, synovial and cerebrospinal fluid (CSF). It performs some basic functions of the cell, both storage and protection, primarily related to its ability to bind and sequester intracellular iron.[78]

Structure

The first X-ray diffraction data of horse spleen ferritin were reported in 1943 and the structure in 1984, but it was not until 1991 that the crystal structure of human ferritin (1FHA) was first reported.[79] The studies conducted by Lawson revealed that ferritin is a round-shape protein constituted by 24 self-assembling subunits that create a hollow cage-like structure of around 12 nm in diameter with an interior cavity of 8 nm (Fig8).[80] Structural analysis shows that the protein cage is composed of dimers arranged with a 4, 3, 2 symmetry with 8 hydrophilic pores at the connection of three subunits and 6 hydrophobic channels at the connection of four subunits.[81]

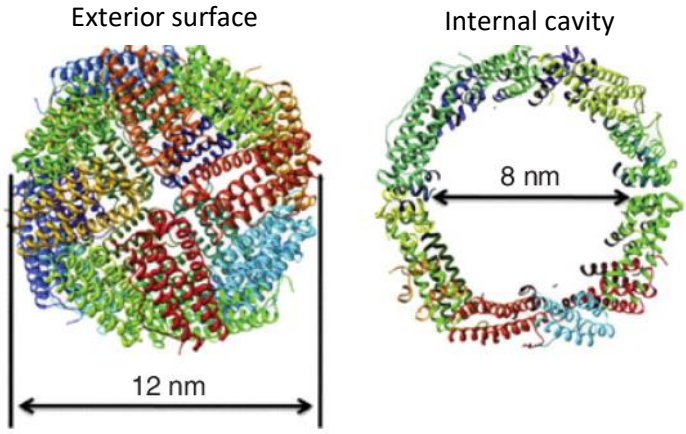

Figure 8: Ribbon diagrams of the exterior surface and internal cavity of human heavy chain ferritin. Reproduced with permission from the corresponding paper. [82]

In mammals, ferritins are generally hetero-polymers composed of two different types of subunits, the heavy (H) and the light (L) (183 and 175 amino acids, respectively, in the human chains).[83] The predominance of one subunit above the other varies in a consistent and tissue-specific way. In general, the liver contains L-rich ferritin, whereas the heart contains ferritin rich in the H subunit.[84] This tissue-specific distribution is due to the fact that each subunit has a define role in iron uptake and storage: H- chain contains the ferroxidase center, while L-chain facilitates the deposition of Fe(III) inside ferritin cavity to form a mineral core (ferrihydrite).[85]

Physiological role

In most tissues, ferritins are mainly present in the cytosol, nucleus, and mitochondria, and play a role in iron storage as well as iron homeostasis. It's worth mentioning that most of the iron present in living organisms is tightly complex in proteins because iron is both potentially toxic and essential for living.[86] Ferritin can internalize up to 4500 Fe(II) atoms transforming them into an inert mineral, making this protein very important in protecting cells from the damage caused by reactive oxygen species, which are produced by Fe(II) oxidation during the Fenton reaction (Fig9).[87,88] Thus ferritin can act as an antioxidant agent and as an iron storage system within cells.[85]

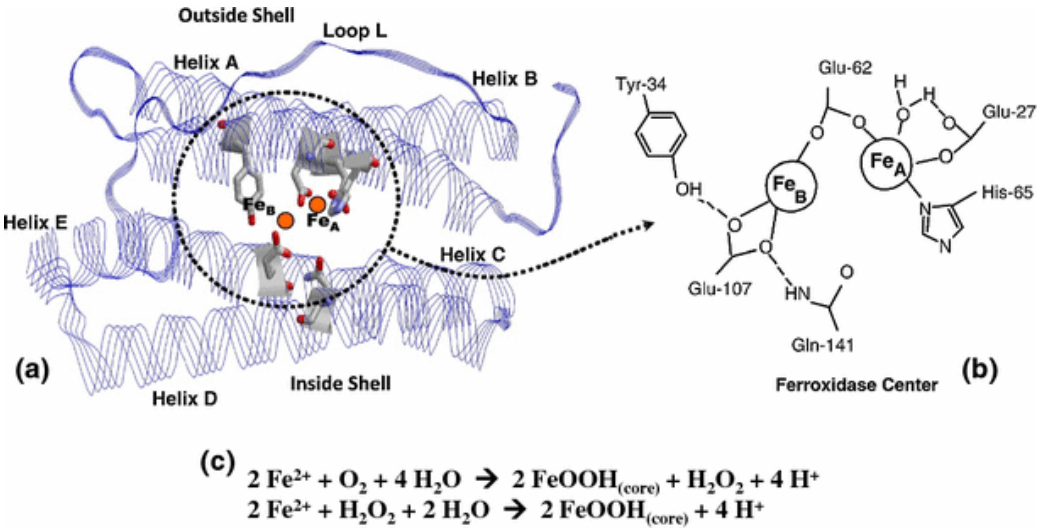

Fenton reaction: Fe^{2+}+ H2O2 → Fe^{3+} + OH^- + ·OH

Figure 9: A) Schematic diagram of the ferroxidase center buried inside the α-helix bundle of the ferritin H chain. B) Highlight of the residues forming the di-iron ferroxidase center. C) Oxidation reactions taking place at the FtH dinuclear ferroxidase center. The site can use either O_2 or H_2O_2 to produce iron core, using the same reagents as the toxic Fenton reaction. Reproduced with permission from the corresponding paper.[81]

Main types of ferritin

Ferritin is present in most tissues as a cytosolic protein, although a mitochondrial form has recently been described and nuclear localization and functions have been proposed. Both these types of ferritin have properties similar to those of cytosolic H-ferritin. In particular nuclear ferritin has a specialized role in DNA protection because its presence correlates with higher resistance to UV and H_2O_2-induced DNA damage. Moreover, this type of ferritin has a role in the regulation of iron accessibility to nuclear components and transcriptional regulation.[89,90] Mitochondrial ferritin function consists mainly in

protecting these organelles from iron-induced damage. The presence of a mitochondrial ferritin in mammals is particularly interesting because these organelles are tightly involved in iron trafficking and have a key role in important cellular activities, including respiration, production of ROS and regulation of apoptotic pathways.[91,92] Mammalian ferritins were also found in body fluids such as serum (10 – 200 μg L^{-1}), urine and cerebrospinal fluid.[93] They are mainly composed of L-subunits and appear to be encoded by the same gene of tissue L-ferritin. Serum ferritin showed similar immunologic reactivity, molecular size and isoelectric focusing characteristics as that of ferritin extracted from the liver or spleen even if it is capable to load much less iron than the cytosolic one. The source of serum ferritin is still unclear, but it seems to be primarily derived from macrophages.[94] Clinically, serum ferritin level is a useful index of body iron status and it can be used to diagnose iron deficiency. Low levels of this protein correlate with iron deficiency anemia and kidney disease while high amounts indicate a state of iron overload which can be determined by hemochromatosis and acute or chronic inflammation.[77] Moreover, in cancer patients the increase in serum ferritin is often associated with more progressive disease and shorter survival. On the other side, a return to normal levels correlates with a response to chemotherapeutic therapy in patients affected by head and neck tumors or breast cancer.[95,96]

Ferritin receptor

The main physiological receptor of ferritin is the human transferrin receptor 1 (TfR1, also named CD71). TfR1 comprises 760 residue subunits that can be divided into a globular extracellular region, a hydrophobic intramembranous region and the remaining residues within the cytoplasm. Consisting of two

monomers, TfR1 is linked by two disulfide bridges, forming a 190 kDa molecule (Fig10).[97]

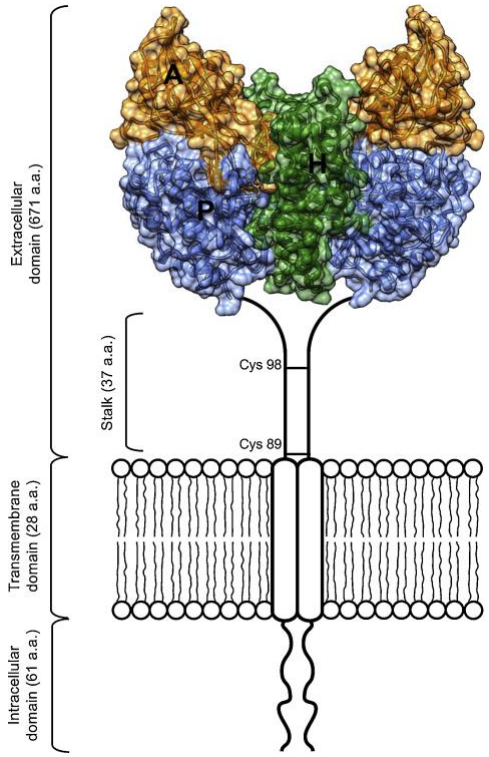

Figure 10: Scheme of the TfR1 homodimer on the cell surface consisting of two monomers linked by disulfide bridges. The TfR1 contains an intracellular domain, a transmembrane domain and a large extracellular domain. The extracellular domain of TfR1 consists of three subdomains: apical (A, orange), helical (H, green) and protease-like domain (P, blue). Reproduced with permission from the corresponding paper.[98]

It was originally identified as the receptor for transferrin (Tf) but, in 2010, Seaman's group discovered that it specifically binds also to the H-ferritin with little or no binding to L-ferritin. After the interaction with its ligands, transferrin or ferritin, the receptor internalizes via clathrin-mediated endocytosis.[99] The demonstration that TfR1 can bind H-ferritin, as well as Tf, raises the possibility

that this dual receptor function may coordinate the processing and use of iron by these iron-binding molecules.

It has been shown that the expression of TfR1 in proliferating cells, such as cancer cells, may be up to 100-fold higher than in normal cells.[100] This could be attributed to the increased need for iron as a cofactor of the ribonucleotide reductase enzyme involved in DNA synthesis of rapidly dividing cells.[101] In particular, in brain cancer TfR1 mediated ROS formation and iron accumulation, facilitate the proliferation of glioma and glioma-induced death of neurons.[102] The expression levels of TfR1 can be used as a biomarker for diagnosis and treating breast cancer patients at the early stage. In fact, Singh et al. found that TfR1 expressions in benign and normal lesions were significantly lower than those in invasive carcinoma and premalignant lesions.[103]

The fact that TfR1 is overexpressed in a variety of malignancies and is efficiently internalized makes it an excellent target for tumor diagnosis and treatment.[104] The strategies for targeting this receptor can be achieved by employing Anti-TfR1 monoclonal antibodies or conjugated-antibodies, H-ferritin nanoparticles and conjugated Tf as carriers to deliver chemotherapeutic drugs, imaging dyes, and radionuclides to treat or detect tumors.[105]

Ferritin as a nanovector

A study conducted in 2010 demonstrated that human HFn without any additional targeting ligands was able to distinguish cancerous cells from normal cells with a sensitivity of 98% and a specificity of 95% in 474 clinical samples from patients with nine different types of cancer revealing its intrinsic tumor-targeting properties.[105] Since then, HFn nanocages have started to be more extensively explored for tumor-targeted delivery of therapeutic drugs and

diagnostic molecules by combining the intrinsic tumor-targeting property and the unique nanocage structure of human HFn.[106] In fact, an HFn without Fe inside known as apoferritin has an empty inner cavity that can be exploited as a reaction chamber for synthesizing nanoparticles and for loading therapeutic drugs and diagnostic molecules. The first chemotherapeutic drug that was loaded inside ferritin is doxorubicin (DOX) and, since 2005, the HFn(DOX) nanocarriers have been extensively studied. HFn(DOX) formulation not only dramatically reduces DOX cardiotoxic effect by improving drug accumulation at the tumor site, but it is also superior to free DOX or Doxil™ in controlling tumor burden in preclinical models of cancer.[107–109] In the field of tumor imaging, HFn has been explored as a delivery platform for imaging probes, particularly for metal-based contrast agents. For example, my research group developed and validated a manganese-based contrast agent named Mn@HFn-RT that proved to efficiently and selectively target breast cancer cells *in vitro* and *in vivo* using very low metal dosages and exhibiting rapid clearance after diagnosis.[110]

It is also possible to modify the surface of the ferritin cage, either genetically or chemically, through the addition of peptides, protein tags or other different functionalities. Despite its natural targeting towards cancer cells, primary amines available on the surface of HFn were exploited to couple peptides, antibodies or fluorophores.[106,111]

HFn nanoparticles can be promising candidates also for effective brain tumor therapy. In fact, TfR1 is not only overexpressed on cancer cells but is also constitutively expressed on capillary endothelial cells, choroid plexus epithelial cells and neurons that require iron for metabolic processes. Thus, HFn is capable to cross the blood-brain barrier without disassembly, leading to the release of

the cargo directly to the tumor cells.[112,113] HFn can be also used to facilitate the delivery of therapeutic mAbs across the BBB.[114]

Recently, during the COVID-19 pandemic, ferritin was also exploited to design and development vaccines that induce more robust neutralizing antibodies response and long-term memory.[115,116] For example, Zhang group conjugated a *Helicobacter pylori* ferritin to the receptor binding domain (RBD) and/or heptad repeat (HR) subunits of the Severe Acute Respiratory Syndrome Coronavirus-2 (SARS-CoV-2) spike protein. These nanoparticles vaccines proved to be of significant immunogenicity, high protection efficiency, broad spectrum and potential safety.[117]

Problems regarding ferritin clinical translation

Over the past decade, hundreds of ferritin-based formulations have been developed that cover a broad range of chemo-therapeutic drugs and diagnostic reagents. Biocompatibility, efficient cargo loading of different molecules and drugs and its natural tumor targeting towards TfR1 make ferritin an ideal tool to treat and diagnose tumors. Nevertheless, to date, ferritin nanoparticles have not yet reached the clinical stage. Ferritin nanoparticles utilized in pre-clinical studies are usually produced as recombinant proteins in *E.coli* strains engineered to express only the human H subunit. Using a bacterium system has some advantages such as the possibility to obtain large quantities of the desired protein, but on the other side to ensure that the nanoparticles are not contaminated by endotoxins which can trigger an immune response and impact experiment results, additional purification procedures must be required. In addition, the immune response may be triggered if cargo loading significantly perturbs the protein architecture of ferritin or the surface-targeting ligands are

not engineered appropriately. These considerations lead to a high cost of production that can limit its clinical translation. The preparation of ferritin nanocarriers is still at the laboratory stage, and how to achieve industrialization is a problem to be solved in the future. Another limitation resides in the drug loading procedure which is critical to standardize in a precisely controllable manner to then scale up the manufacturing process for clinical application. Moreover, ferritin nanoparticles showed a low encapsulation capacity for hydrophobic compounds which leak out from ferritin just after the encapsulation process. Also, the exact principles and kinetic mechanism of payload release from ferritin vehicles *in vitro* and *in vivo* should be explored more thoroughly in order to quantitatively determine the ferritin-based drug delivery pathway. Although there are still some problems to be solved to make ferritin nanocarriers ready to be used in clinical applications, the increasing number of experimental evidences in support of the use of ferritin as a nano-delivery platform will speed up its translation from bench to bedside.[118–120]

3. References

1. Cooper, G. M. The Cell. **8**, 103–108 (2000).
2. Yahya, E. B. & Alqadhi, A. M. Recent trends in cancer therapy: A review on the current state of gene delivery. *Life Sci* **269**, (2021).
3. Sung, H. *et al.* Global Cancer Statistics 2020: GLOBOCAN Estimates of Incidence and Mortality Worldwide for 36 Cancers in 185 Countries. *CA Cancer J Clin* **71**, 209–249 (2021).
4. Cheng, Z., Li, M., Dey, R. & Chen, Y. Nanomaterials for cancer therapy: current progress and perspectives. *J Hematol Oncol* **14**, (2021).
5. Nowell, P. C. The clonal evolution of tumor cell populations. *Science* **194**, 23–28 (1976).
6. Hanahan, D. & Weinberg, R. A. Hallmarks of cancer: The next generation. *Cell* **144**, 646–674 (2011).
7. Miller, K. D. *et al.* Brain and other central nervous system tumor statistics, 2021. *CA Cancer J Clin* **71**, 381–406 (2021).
8. Voisin, M. R., Sasikumar, S., Mansouri, A. & Zadeh, G. Incidence and prevalence of primary malignant brain tumours in Canada from 1992 to 2017: an epidemiologic study. *CMAJ Open* **9**, E973–E979 (2021).
9. McKinney, P. A. Brain tumours: incidence, survival, and aetiology. *J Neurol Neurosurg Psychiatry* **75**, ii12–ii17 (2004).
10. Gimple, R. C., Yang, K., Halbert, M. E., Agnihotri, S. & Rich, J. N. Brain cancer stem cells: resilience through adaptive plasticity and hierarchical heterogeneity. *Nat Rev Cancer* **22**, 497–514 (2022).
11. Nayak, L., Lee, E. Q. & Wen, P. Y. Epidemiology of brain metastases. *Curr Oncol Rep* **14**, 48–54 (2012).

12. Barnholtz-Sloan, J. S. *et al.* Incidence proportions of brain metastases in patients diagnosed (1973 to 2001) in the Metropolitan Detroit Cancer Surveillance System. *J Clin Oncol* **22**, 2865–2872 (2004).
13. Brain Tumors: Introduction | Spectrum Health Lakeland. https://www.spectrumhealthlakeland.org/lakeland-ear-nose-and-throat/ent-health-library/Content/34/17824-1/.
14. Louis, D. N. *et al.* The 2021 WHO Classification of Tumors of the Central Nervous System: a summary. *Neuro Oncol* **23**, 1231–1251 (2021).
15. Lapointe, S., Perry, A. & Butowski, N. A. Primary brain tumours in adults. *The Lancet* **392**, 432–446 (2018).
16. Perry, A. & Wesseling, P. Histologic classification of gliomas. *Handb Clin Neurol* **134**, 71–95 (2016).
17. Davis, M. E. Epidemiology and Overview of Gliomas. *Semin Oncol Nurs* **34**, 420–429 (2018).
18. Omuro, A. & DeAngelis, L. M. Glioblastoma and other malignant gliomas: a clinical review. *JAMA* **310**, 1842–1850 (2013).
19. Hanif, F., Muzaffar, K., Perveen, K., Malhi, S. M. & Simjee, S. U. Glioblastoma Multiforme: A Review of its Epidemiology and Pathogenesis through Clinical Presentation and Treatment. *Asian Pac J Cancer Prev* **18**, 3 (2017).
20. Kim, H. J., Park, J. W. & Lee, J. H. Genetic Architectures and Cell-of-Origin in Glioblastoma. *Front Oncol* **10**, 3097 (2021).
21. Chen, J., McKay, R. M. & Parada, L. F. Malignant glioma: Lessons from genomics, mouse models, and stem cells. *Cell* **149**, 36–47 (2012).
22. Giambra, M. *et al.* The peritumoral brain zone in glioblastoma: where we are and where we are going. *J Neurosci Res* **101**, 199–216 (2023).

23. Mrugala, M. M. Advances and Challenges in the Treatment of Glioblastoma: A Clinician's Perspective. *Discov Med* **15**, 221–230 (2013).
24. Davis, M. E. Glioblastoma: Overview of disease and treatment. *Clin J Oncol Nurs* **20**, 1–8 (2016).
25. Carlsson, S. K., Brothers, S. P. & Wahlestedt, C. Emerging treatment strategies for glioblastoma multiforme. *EMBO Mol Med* **6**, 1359–1370 (2014).
26. Oronsky, B., Reid, T. R., Oronsky, A., Sandhu, N. & Knox, S. J. A Review of Newly Diagnosed Glioblastoma. *Front Oncol* **10**, 2292 (2021).
27. Hegi, M. E. *et al.* MGMT gene silencing and benefit from temozolomide in glioblastoma. *N Engl J Med* **352**, 997–1003 (2005).
28. Ou, A., Yung, W. K. A. & Majd, N. Molecular Mechanisms of Treatment Resistance in Glioblastoma. *Int. J. Mol. Sci* **22**, 351 (2021).
29. Carrieri, F. A., Smack, C., Siddiqui, I., Kleinberg, L. R. & Tran, P. T. Tumor Treating Fields: At the Crossroads Between Physics and Biology for Cancer Treatment. *Front Oncol* **10**, (2020).
30. Harbeck, N. *et al.* Breast cancer. *Nature Reviews Disease Primers 2019 5:1* **5**, 1–31 (2019).
31. Ellsworth, R. E., Blackburn, H. L., Shriver, C. D., Soon-Shiong, P. & Ellsworth, D. L. Molecular heterogeneity in breast cancer: State of the science and implications for patient care. *Semin Cell Dev Biol* **64**, 65–72 (2017).
32. Turashvili, G. & Brogi, E. Tumor Heterogeneity in Breast Cancer. *Front Med (Lausanne)* **4**, (2017).

33. Breast cancer pathogenesis and histologic vs. molecular subtypes | McMaster Pathophysiology Review. http://www.pathophys.org/breast-cancer/breastcancer-copy/.

34. Godoy-Ortiz, A. *et al.* Deciphering her2 breast cancer disease: Biological and clinical implications. *Front Oncol* **9**, (2019).

35. Singh, D. D., Kumar Yadav, D., Amico, G. D. ', Vanella, L. & Marino Gammazza, A. TNBC: Potential Targeting of Multiple Receptors for a Therapeutic Breakthrough, Nanomedicine, and Immunotherapy. *Biomedicines 2021, Vol. 9, Page 876* **9**, 876 (2021).

36. Lee, K. L., Kuo, Y. C., Ho, Y. S. & Huang, Y. H. Triple-Negative Breast Cancer: Current Understanding and Future Therapeutic Breakthrough Targeting Cancer Stemness. *Cancers 2019, Vol. 11, Page 1334* **11**, 1334 (2019).

37. Mcdonald, E. S., Clark, A. S., Tchou, J., Zhang, P. & Freedman, G. M. Clinical Diagnosis and Management of Breast Cancer. *J Nucl Med* **57**, 9–16 (2016).

38. Darby, S. *et al.* Effect of radiotherapy after breast-conserving surgery on 10-year recurrence and 15-year breast cancer death: meta-analysis of individual patient data for 10,801 women in 17 randomised trials. *Lancet* **378**, 1707–1716 (2011).

39. Davies, C. *et al.* Long-term effects of continuing adjuvant tamoxifen to 10 years versus stopping at 5 years after diagnosis of oestrogen receptor-positive breast cancer: ATLAS, a randomised trial. *The Lancet* **381**, 805–816 (2013).

40. Baselga, J., Perez, E. A., Pienkowski, T. & Bell, R. Adjuvant trastuzumab: a milestone in the treatment of HER-2-positive early breast cancer. *Oncologist* **11 Suppl 1**, 4–12 (2006).

41. Won, K. A. & Spruck, C. Triple-negative breast cancer therapy: Current and future perspectives (Review). *Int J Oncol* **57**, 1245 (2020).
42. Nedeljković, M. & Damjanović, A. Mechanisms of Chemotherapy Resistance in Triple-Negative Breast Cancer—How We Can Rise to the Challenge. *Cells 2019, Vol. 8, Page 957* **8**, 957 (2019).
43. Porter, A. L., Youtie, J., Shapira, P. & Schoeneck, D. J. Refining search terms for nanotechnology. *Journal of Nanoparticle Research* **10**, 715–728 (2008).
44. Feynman, R. P. There's Plenty of Room at the Bottom. (1960).
45. Bayda, S. *et al.* molecules The History of Nanoscience and Nanotechnology: From Chemical-Physical Applications to Nanomedicine. *Molecules* **25**, 112 (2020).
46. Nanoscience and nanotechnologies: opportunities and uncertainties. (2004). https://royalsociety.org/topicspolicy/publications/2004/nanoscience-nanotechnologies/
47. Liu, Y., Miyoshi, H. & Nakamura, M. Nanomedicine for drug delivery and imaging: A promising avenue for cancer therapy and diagnosis using targeted functional nanoparticles. *Int J Cancer* **120**, 2527–2537 (2007).
48. Kim, B. Y. S., Rutka, J. T. & Chan, W. C. W. Nanomedicine. *New England Journal of Medicine* **363**, 2434–2443 (2010).
49. Salata, O. v. Applications of nanoparticles in biology and medicine. *J Nanobiotechnology* **2**, 1–6 (2004).
50. Sanna, V., Pala, N. & Sechi, M. Targeted therapy using nanotechnology: focus on cancer. *Int J Nanomedicine* **9**, 467–483 (2014).

51. Garbayo, E. *et al.* Nanomedicine and drug delivery systems in cancer and regenerative medicine. *Wiley Interdiscip Rev Nanomed Nanobiotechnol* **12**, (2020).
52. Riehemann, K. *et al.* Nanomedicine-Challenge and Perspectives. *Angewandte Chemie International Edition* **48**, 872–897 (2009).
53. Shukla, A. & Maiti, P. Nanomedicine and versatile therapies for cancer treatment. *MedComm (Beijing)* **3**, (2022).
54. Nanotechnology and its Applications in Medicine | Enhanced Reader.
55. Reimer, P. & Balzer, T. Ferucarbotran (Resovist): a new clinically approved RES-specific contrast agent for contrast-enhanced MRI of the liver: properties, clinical development, and applications. *Eur Radiol* **13**, 1266–1276 (2003).
56. Veiseh, O., Gunn, J. W. & Zhang, M. Design and fabrication of magnetic nanoparticles for targeted drug delivery and imaging. *Adv Drug Deliv Rev* **62**, 284–304 (2010).
57. Fathi-Achachelouei, M. *et al.* Use of Nanoparticles in Tissue Engineering and Regenerative Medicine. *Front Bioeng Biotechnol* **7**, (2019).
58. Shi, J., Votruba, A. R., Farokhzad, O. C. & Langer, R. Nanotechnology in Drug Delivery and Tissue Engineering: From Discovery to Applications. *Nano Lett* **10**, 3223–3230 (2010).
59. Vial, S., Reis, R. L. & Oliveira, J. M. Recent advances using gold nanoparticles as a promising multimodal tool for tissue engineering and regenerative medicine. *Curr Opin Solid State Mater Sci* **21**, 92–112 (2017).
60. Hong, S. *et al.* Protein-Based Nanoparticles as Drug Delivery Systems. *Pharmaceutics* **12**, 604 (2020).

61. Cho, K., Wang, X., Nie, S., Chen, Z. & Shin, D. M. Therapeutic Nanoparticles for Drug Delivery in Cancer. *Clinical Cancer Research* **14**, 1310–1316 (2008).

62. Wilczewska, A. Z., Niemirowicz, K., Markiewicz, K. H. & Car, H. Nanoparticles as drug delivery systems. *Pharmacological Reports* **64**, 1020–1037 (2012).

63. Carissimi, G., G. Montalbán, M., G. Fuster, M. & Víllora, G. Nanoparticles as Drug Delivery Systems. in *21st Century Nanostructured Materials - Physics, Chemistry, Classification, and Emerging Applications in Industry, Biomedicine, and Agriculture*, IntechOpen, (2022).

64. Kingsley, J. D. *et al.* Nanotechnology: A focus on nanoparticles as a drug delivery system. *Journal of Neuroimmune Pharmacology* **1**, 340–350 (2006).

65. Houshmand, M. *et al.* Nanocarriers as Magic Bullets in the Treatment of Leukemia. *Nanomaterials* **10**, 276 (2020).

66. Greish, K., Mathur, A., Bakhiet, M. & Taurin, S. Nanomedicine: Is it lost in translation? *Ther Deliv* **9**, 269–285 (2018).

67. Salvioni, L. *et al.* Thirty Years of Cancer Nanomedicine: Success, Frustration, and Hope. *Cancers (Basel)* **11**, (2019).

68. Nie, S., Xing, Y., Kim, G. J. & Simons, J. W. Nanotechnology applications in cancer. *Annu Rev Biomed Eng* **9**, 257–88 (2007).

69. Bazak, R., Houri, M., el Achy, S., Kamel, S. & Refaat, T. Cancer active targeting by nanoparticles: a comprehensive review of literature. *J Cancer Res Clin Oncol* **141**, 769–784 (2015).

70. Barui, A. K., Oh, J. Y., Jana, B., Kim, C. & Ryu, J.-H. Cancer-Targeted Nanomedicine: Overcoming the Barrier of the Protein Corona. *Adv Ther (Weinh)* **3**, 1900124 (2020).

71. Madamsetty, V. S., Mukherjee, A. & Mukherjee, S. Recent trends of the bio-inspired nanoparticles in cancer theranostics. *Front Pharmacol* **10**, 1264 (2019).

72. Marques, A. C., Costa, P. J., Velho, S. & Amaral, M. H. Functionalizing nanoparticles with cancer-targeting antibodies: A comparison of strategies. *Journal of Controlled Release* **320**, 180–200 (2020).

73. Rasool, M. *et al.* New challenges in the use of nanomedicine in cancer therapy. (2022) doi:10.1080/21655979.2021.2012907.

74. Anselmo, A. C., Mitragotri, S. & Samir Mitragotri, C. Nanoparticles in the clinic. *Bioeng Transl Med* **1**, 10–29 (2016).

75. Mahmoudi, K., Bouras, A., Bozec, D., Ivkov, R. & Hadjipanayis, C. Magnetic hyperthermia therapy for the treatment of glioblastoma: a review of the therapy's history, efficacy and application in humans. *Int J Hyperthermia* **34**, 1316–1328 (2018).

76. Arosio, P., Elia, L. & Poli, M. Critical Review Ferritin, Cellular Iron Storage and Regulation. *IUBMB Life* **69**, 414–422 (2017).

77. Knovich, M. A., Storey, J. A., Coffman, L. G., Torti, S. v. & Torti, F. M. Ferritin for the clinician. *Blood Rev* **23**, 95–104 (2009).

78. Meyron-Holtz, E. G., Moshe-Belizowski, S. & Cohen, L. A. A possible role for secreted ferritin in tissue iron distribution. doi:10.1007/s00702-011-0582-0.

79. Bhaskar, S. & Lim, S. Engineering protein nanocages as carriers for biomedical applications. *NPG Asia Mater* **9**, e371–e371 (2017).

80. Lawson, D. M. *et al.* Solving the structure of human H ferritin by genetically engineering intermolecular crystal contacts. *Nature* **349**, 541–544 (1991).

81. Finazzi, D. & Arosio, P. Biology of ferritin in mammals: an update on iron storage, oxidative damage and neurodegeneration. *Arch Toxicol* **3**, 1787–1802 (2014).

82. Fan, K., Gao, L. & Yan, X. Human ferritin for tumor detection and therapy. *Wiley Interdiscip Rev Nanomed Nanobiotechnol* **5**, 287–98 (2013).

83. Pozzi, C. *et al.* Chemistry at the protein-mineral interface in L-ferritin assists the assembly of a functional (μ3-oxo)Tris[(μ2-peroxo)] triiron(III) cluster. *Proc Natl Acad Sci U S A* **114**, 2580–2585 (2017).

84. Rucker, P., Torti, F. M. & Torti, S. v. Role of H and L Subunits in Mouse Ferritin. *Journal of Biological Chemistry* **271**, 33352–33357 (1996).

85. He, D. & Marles-Wright, J. Ferritin family proteins and their use in bionanotechnology. *N Biotechnol* **32**, 651–657 (2015).

86. Harrison, P. M. & Arosio, P. The ferritins: molecular properties, iron storage function and cellular regulation. *Biochimica et Biophysica Acta (BBA) - Bioenergetics* **1275**, 161–203 (1996).

87. Theil, E. C. Ferritin protein nanocages—the story. *Nanotechnol Percept* **8**, 7 (2012).

88. Arosio, P., Ingrassia, R. & Cavadini, P. Ferritins: a family of molecules for iron storage, antioxidation and more. *Biochim Biophys Acta* **1790**, 589–599 (2009).

89. Alkhateeb, A. A. & Connor, J. R. Nuclear ferritin: A new role for ferritin in cell biology. *Biochimica et Biophysica Acta (BBA) - General Subjects* **1800**, 793–797 (2010).

90. Surguladze, N., Patton, S., Cozzi, A., Fried, M. G. & Connor, J. R. Characterization of nuclear ferritin and mechanism of translocation. *Biochemical Journal* **388**, 731–740 (2005).

91. Levi, S. & Arosio, P. Mitochondrial ferritin. *Int J Biochem Cell Biol* **36**, 1887–9 (2004).

92. Levi, S., Ripamonti, M., Dardi, M., Cozzi, A. & Santambrogio, P. Mitochondrial Ferritin: Its Role in Physiological and Pathological Conditions. *Cells* **10**, 1969 (2021).

93. Walters, G. O., Miller, F. M. & Worwood, M. Serum ferritin concentration and iron stores in normal subjects. *J Clin Pathol* **26**, 770 (1973).

94. Wang, W., Knovich, M. A., Coffman, L. G., Torti, F. M. & Torti, S. v. Serum ferritin: Past, present and future. *Biochim Biophys Acta* **1800**, 760–769 (2010).

95. Maxim, P. E. & Veltri, R. W. Serum ferritin as a tumor marker in patients with squamous cell carcinoma of the head and neck. *Cancer* **57**, 305–311 (1986).

96. Alkhateeb, A. A. *et al.* Elevation in Inflammatory Serum Biomarkers Predicts Response to Trastuzumab-Containing Therapy. *PLoS One* **7**, e51379 (2012).

97. Shen, Y. *et al.* Transferrin receptor 1 in cancer: a new sight for cancer therapy. *Am J Cancer Res* **8**, 916–931 (2018).

98. Luria-Pérez, R., Helguera, G. & Rodríguez, J. A. Antibody-mediated targeting of the transferrin receptor in cancer cells. *Boletín Médico del Hospital Infantil de México* **73**, 372–379 (2016).

99. Li, L. *et al.* Binding and uptake of H-ferritin are mediated by human transferrin receptor-1. *Proc Natl Acad Sci U S A* **107**, 3505–3510 (2010).

100. Fan, K., Gao, L. & Yan, X. Human ferritin for tumor detection and therapy. *Wiley Interdiscip Rev Nanomed Nanobiotechnol* **5**, 287–98 (2013).

101. Daniels, T. R., Delgado, T., Rodriguez, J. A., Helguera, G. & Penichet, M. L. The transferrin receptor part I: Biology and targeting with cytotoxic antibodies for the treatment of cancer. *Clinical Immunology* **121**, 144–158 (2006).

102. Chirasani, S. R. *et al.* Transferrin-receptor-mediated iron accumulation controls proliferation and glutamate release in glioma cells. *J Mol Med* **87**, 153–167 (2009).

103. Singh, M. *et al.* Differential expression of transferrin receptor (TfR) in a spectrum of normal to malignant breast tissues: Implications for in situ and invasive carcinoma. *Applied Immunohistochemistry and Molecular Morphology* **19**, 417–423 (2011).

104. Daniels, T. R., Delgado, T., Helguera, G. & Penichet, M. L. The transferrin receptor part II: Targeted delivery of therapeutic agents into cancer cells. *Clinical Immunology* **121**, 159–176 (2006).

105. Fan, K. *et al.* Magnetoferritin nanoparticles for targeting and visualizing tumour tissues. *Nat Nanotechnol* **7**, 459–464 (2012).

106. Khoshnejad, M. *et al.* Ferritin Nanocages with Biologically Orthogonal Conjugation for Vascular Targeting and Imaging. *Bioconjug Chem* **29**, 1209–1218 (2018).

107. Jiang, B. *et al.* GRP78-targeted ferritin nanocaged ultra-high dose of doxorubicin for hepatocellular carcinoma therapy. *Theranostics* **9**, 2167–2182 (2019).

108. Mazzucchelli, S. *et al.* Nanometronomic treatment of 4T1 breast cancer with nanocaged doxorubicin prevents drug resistance and circumvents cardiotoxicity. *Oncotarget* **8**, 8383–8396 (2016).

109. Mainini, F. *et al.* pharmaceutics Protein-Based Nanoparticles for the Imaging and Treatment of Solid Tumors: The Case of Ferritin Nanocages, a Narrative Review. *Pharmaceutics* **13**, (2021).

110. Tullio, C. *et al.* Development of an Effective Tumor-Targeted Contrast Agent for Magnetic Resonance Imaging Based on Mn/H-Ferritin Nanocomplexes. *ACS Appl Bio Mater* **4**, 7800–7810 (2021).

111. Truffi, M. *et al.* Ferritin nanocages: A biological platform for drug delivery, imaging and theranostics in cancer. *Pharmacol Res* **107**, 57–65 (2016).

112. Huang, C. W. *et al.* Integrin α2β1-targeting ferritin nanocarrier traverses the blood–brain barrier for effective glioma chemotherapy. *J Nanobiotechnology* **19**, 1–17 (2021).

113. Fan, K. *et al.* Ferritin Nanocarrier Traverses the Blood Brain Barrier and Kills Glioma. *ACS Nano* **12**, 4105–4115 (2018).

114. Rizzuto, M. A. *et al.* H-Ferritin nanoparticle-mediated delivery of antibodies across a BBB in vitro model for treatment of brain malignancies. *Biomater Sci* **9**, 2032–2042 (2021).

115. Wang, W., Huang, B., Zhu, Y., Tan, W. & Zhu, M. Ferritin nanoparticle-based SARS-CoV-2 RBD vaccine induces a persistent antibody response and long-term memory in mice. *Cell Mol Immunol* **18**, 749–751 (2021).

116. Joyce, M. G. *et al.* SARS-CoV-2 ferritin nanoparticle vaccines elicit broad SARS coronavirus immunogenicity. *bioRxiv* (2021)

117. Ma, X. *et al.* Nanoparticle Vaccines Based on the Receptor Binding Domain (RBD) and Heptad Repeat (HR) of SARS-CoV-2 Elicit Robust Protective Immune Responses. *Immunity* **53**, 1315-1330.e9 (2020).
118. Song, N. *et al.* Ferritin: A Multifunctional Nanoplatform for Biological Detection, Imaging Diagnosis, and Drug Delivery. *Acc Chem Res* **54**, 3313–3325 (2021).
119. Sun, X., Hong, Y., Gong, Y., Zheng, S. & Xie, D. Bioengineered ferritin nanocarriers for cancer therapy. *Int J Mol Sci* **22**, (2021).
120. Mainini, F. *et al.* pharmaceutics Protein-Based Nanoparticles for the Imaging and Treatment of Solid Tumors: The Case of Ferritin Nanocages, a Narrative Review. *Pharmaceutics* **13**, (2021).

CHAPTER ONE

Evaluation of HFn-mAb nanoconjugates-mediated anticancer activity in 3D tumor models

1. Introduction

1.1 Cancer immunotherapy

Cancer immunotherapy is a treatment developed to eliminate the primary mass of cancer and relevant peripheral metastases by re-educating the host immune system to recognize the cancer cells as "non-self" and consequently react against them. The idea that the immune system can recognize and control tumor growth can be traced back to 1893 when William Coley and colleagues conducted the first experimental immunotherapy treatment of cancer based on the observation that some patients carrying a bacterial infection exhibited more extensive tumor regression compared with uninfected individuals.[1,2] His achievements were largely unnoticed for over fifty years until 1945 when Ruth and John Graham worked and developed the first ever cancer vaccine.[3] Another milestone in cancer immunotherapy was set when, in 1957, Thomas and Burnet first proposed their theory of cancer immunosurveillance. They suggested that the immune system is capable of detecting and killing somatic cells transformed by spontaneous mutation. Even if at the time this hypothesis could not be experimentally tested because so little was known about the molecular and cellular basis of immunity, now many studies support this concept. Later on, the existence of T cells and their role was clarified in 1967 by Jacques Miller. Six years later dendritic cells (DC cells) and Natural Killer cells (NK cells) were discovered and described. In 1991 Van der Bruggen and colleagues identified the first human tumor antigen recognized by T lymphocytes.[4,5] These discoveries have led to the modification of cancer immunosurveillance into the wider immunoediting hypothesis. This process is based on the notion that the

immune system not only protects the host against tumor formation but also shapes tumor immunogenicity. Indeed, immunity has a dual action of host-protective and tumor-promoting on developing tumors.[6] Cancer immunoediting is comprised of three phases that function either independently or in sequence: elimination, equilibrium and escape (Fig1).

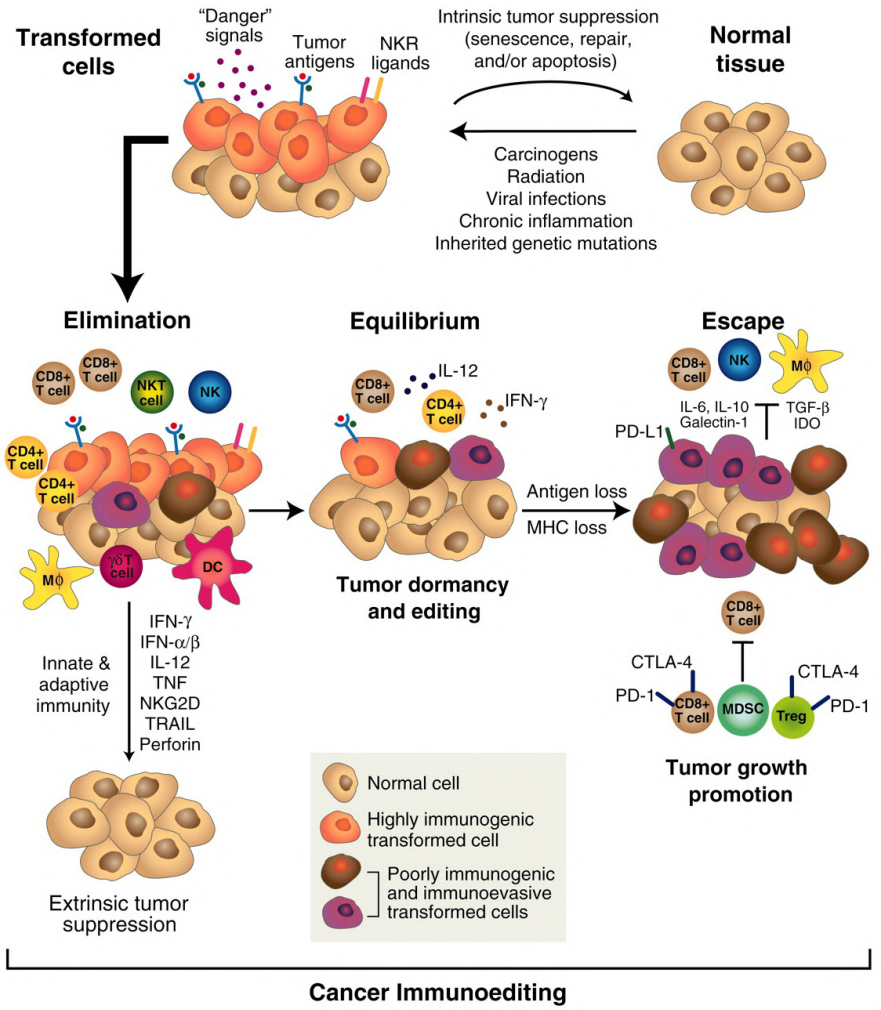

Figure 1: The cancer immunoediting process. Cancer immunoediting is an extrinsic tumor suppressor mechanism that engages only after a cellular transformation has occurred and intrinsic tumor suppressor mechanisms have failed. It consists of three

sequential phases: elimination, equilibrium, and escape. In the elimination phase, innate and adaptive immunity work together to destroy developing tumors long before they become clinically apparent. If this phase goes to completion, then the host remains free of cancer, and elimination thus represents the full extent of the process. If, however, a rare cancer cell variant is not destroyed in the elimination phase, it may then enter the equilibrium phase, in which its outgrowth is prevented by immunologic mechanisms and immunogenicity occurs. Equilibrium may also represent an end stage of the cancer immunoediting process and may restrain the outgrowth of occult cancers for the lifetime of the host. However, as a consequence of constant immune selection pressure placed on genetically unstable tumor cells held in equilibrium, tumor cell variants may eventually evade the immune system by a variety of mechanisms and become clinically detectable in the escape phase. Reproduced with permission from the corresponding paper.[6]

The **elimination phase** can be described as an updated version of the classical cancer immunosurveillance concept, in which innate and adaptive immune systems cooperate with each other to detect and eliminate transformed cells before they become clinically evident. The immune response starts when innate immunity cells became aware of the presence of a growing tumor because of local tissue disruption determined by angiogenesis, tissue-invasive growth or expression of stress ligands on the surface of tumor cells. The response proceeds with the activation of DC cells and their crosstalk with T cells which consequently mature in CD8+ T cytotoxic cells and CD4+ T helper cells.[6,7]

Malignant cells may, however, not be completely eradicated but instead enter into an **equilibrium phase** in which the immune system controls the tumor cell growth. During equilibrium, adaptive immunity constrains the growth of

clinically undetectable tumor cells and edits tumor cell immunogenicity. Thus, tumor cells remain in a latent state which could be prolonged also for decades. This latency may, however, be suddenly interrupted leading to the **escape phase** in which tumor cells that have acquired the ability to circumvent immune recognition and/or destruction emerge as progressively growing, visible tumors. Cancer cells escape can occur through many different mechanisms such as defects in antigen presentation machinery, the upregulation of negative regulatory pathways and the production of immunosuppressive cytokines such as vascular endothelial growth factor (VEGF).[5,7,8]

1.2 Cancer treatment using immunotherapy

A goal of immunotherapy is to balance the immune system to eliminate cancer cells while not producing unchecked autoimmune inflammatory responses that result in therapeutic limitations of immunotherapies**.** Each immunotherapy seeks to increase immune function and differs by various mechanisms of action by which they are categorized as active and passive. **Active immunotherapy** is the direct stimulation of the host immune system against cancer cells. These strategies include vaccination with tumor antigens and the use of oncolytic viruses or checkpoint inhibitors that will trigger an antitumor response. Moreover, these protocols are able to induce the generation of immunological memory of the antigen, thus creating a long-lasting antitumor effect. **Passive immunotherapies**, which are generally used in patients with weak immune system activation, produce specific but often short-lived responses that therefore require regular administration of these treatments. They include the infusion of tumor-specific antibodies, the systemic administration of cytokines and the adoptive transfer of pre-activated immune cells (Fig.2).[8,9]

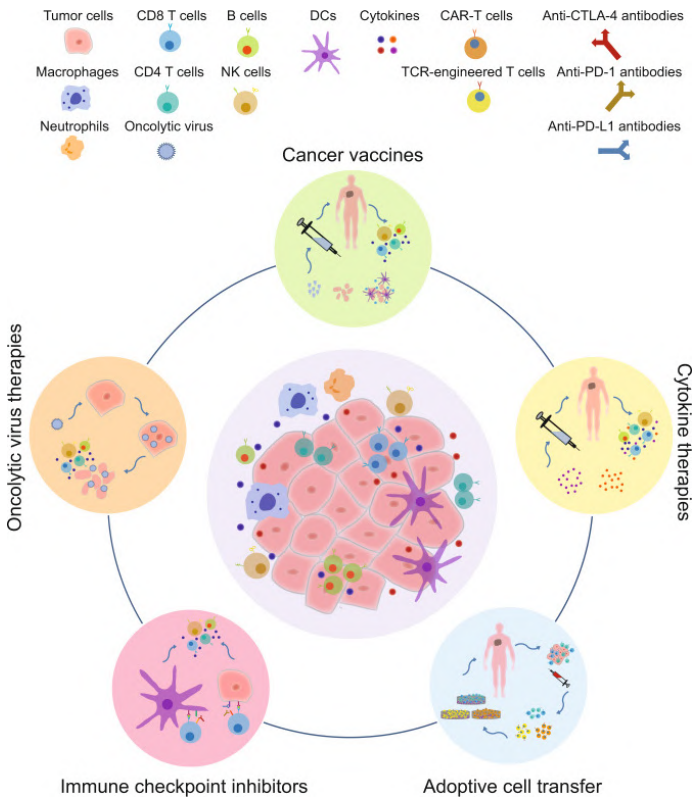

Figure 2: The major categories of immunotherapy. Different forms of cancer immunotherapy, including oncolytic virus therapies, cancer vaccines, cytokine therapies, adoptive cell transfer, and immune checkpoint inhibitors, have evolved and shown promise in clinical practice. Reproduced with permission from the corresponding paper.[8]

1.2.1 Oncolytic viruses

Oncolytic virus therapies consist of the use of genetically modified viruses to infect tumor cells and thus stimulate a proinflammatory environment to augment systemic antitumor immunity. Oncolytic viruses can kill infected cancer cells in many different ways, ranging from direct virus-mediated

cytotoxicity through a variety of cytotoxic immune effector mechanisms.[10] With advances in genetic engineering and virus transformation technologies, oncolytic virus therapies have made much progress in recent years. In particular, talimogene laherparepvec (T-Vec), also known as Imlygic, a genetically modified herpes simplex virus, has demonstrated impressive clinical benefits for patients with advanced melanoma and has been approved in 2015 for the treatment of unresectable metastatic melanoma.[8,11,12]

1.2.2 Cancer vaccines

Cancer vaccines can be subdivided into two broad categories on the basis of their approach to treating cancer: prophylactic and therapeutic cancer vaccines. Prophylactic therapy using cancer vaccines involves the process of targeting infections that are likely to result in the development of cancer. One of them is Gardasil which targets the Human Papilloma virus (HPV) that is found to be associated with cervical cancer. Therapeutic cancer vaccines, on the other hand, target the already existing cancer cells in the body. They are designed to expose patients to tumor antigens inducing a tumor-specific immune response that aims at stopping the cancer growth and preventing recurrences. Anti-cancer vaccines are categorized into different classes, including dendritic-based vaccines, antigen-based vaccines and whole cell vaccines. DC-based vaccines involve the reinfusion of isolated DCs pulsed with tumor antigens or tumor cell lysates and stimulated with a defined maturation cocktail *ex vivo*. One representative example is sipuleucel-T, a DC-based immunotherapy that has been approved for the treatment of advanced prostate cancer. Antigen-based vaccine exploits immunogenic peptides from tumor-specific or tumor-associated antigens to elicit the immune response. Furthermore, whole tumor

cells can also be utilized to produce vaccines and evoke spontaneous immune responses without having to identify the full range of tumor antigens.[5,11,13]

1.2.3 Immune checkpoint inhibitors

The role of checkpoints is to ensure that an immune inflammatory response is not constantly activated once foreign or tumor antigens have stimulated a response. In fact, T cells are activated by two stimuli: the first involves interaction between the T-cell receptor (TCR) on the T-cells membrane and MHC molecule-tumor peptide on antigen-presenting cells (APCs) membrane, while the second consists in the interaction of the costimulatory T-cell receptor CD28 with the B7 ligand expressed by APC cells. This interaction is tightly regulated or suppressed by inhibitory checkpoint receptor/ligand pairs to avoid collateral damage from autoimmunity. The two pairs of inhibitory receptor/ligands which have received the most attention in recent years are cytotoxic T lymphocyte-associated antigen-4 (CTLA-4) receptor with B7 ligand, and programmed cell death protein 1 (PD1) receptor with PD1-L1 ligand. The immune checkpoints inhibitors (ICIs) are a class of molecules, mainly mAbs, that selectively bind to CTLA-4 and PD-1 competing with their ligands thus avoiding activation. The first ICI to be approved by FDA was ipilimumab (against CTLA-4) and, due to its ability to enhance T-cell activation and induce durable responses, is used for the treatment of melanoma.[5,8,14]

1.2.4 Adoptive cell therapy

Adoptive cell therapy mostly involves the isolation and *in vitro* expansion of tumor-specific T-cells, followed by infusion back into the cancer patient usually

together with interleukin-2 (IL-2). These efforts have also extended to using natural killer cells since they display rapid and potent immunity to solid tumor metastasis and hematological cancers.[5]

In 2010 Rosemberg published data about the so-called chimera antigen receptor (CAR) therapy. This therapy makes use of autologous T cells, harvested from the body of the patient. After isolation, they are genetically engineered *ex vivo* by using either viral (retroviruses or adenovirus) or virus-free transfection methods. The gene-transfer methods such as electroporation, liposomes, transposons, nanoparticles or CRISPR-Cas9 are widely used to transfer certain genes to T-cells in order to modify them. After reinjection in the patient, CAR-T cells that meet the antigen get activated and proliferate *in vivo*, establishing also an immunological memory.[11] As of October 2021, there are four currently approved CAR-T products available for non-Hodgkin lymphomas, two for B-cell acute lymphoblastic leukemia and one for multiple myeloma which have shown high overall response rate and durable remissions in patients who have failed standard therapies.[15] However, there are still some barriers to effective CAR-T cells therapy which include toxicity of the treatment in terms of cytokine release syndrome and neurotoxic effects, as well as modest anti-tumor activity, antigen escape, restricted trafficking, limited tumor infiltration and autoreactivity against normal cell expressing low level of the antigen.[16]

1.2.5 Monoclonal Antibodies

Monoclonal antibodies (mAbs) are antibodies made by clones of a unique B cell, all of which bind to specific portions of an antigen also known as an epitope. They are circulating proteins composed of two main functional parts: a constant fraction (Fc) which is mainly involved in the activation of the immune system

and a variable fraction (Fab) which is responsible for the specific interaction with the antigen. Their basic structure is composed of two heavy and two light chains in the shape of a Y (Fig3).

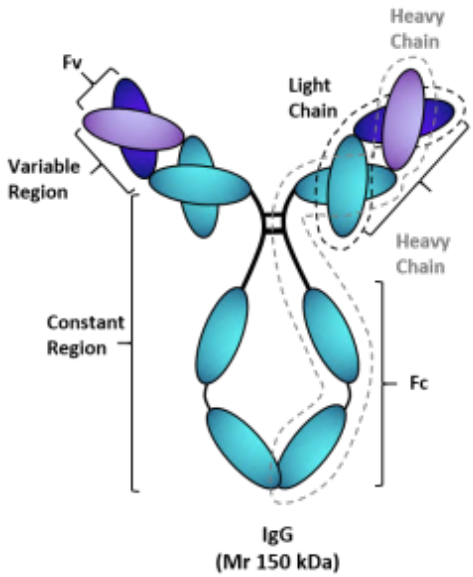

Figure 3: Scheme of monoclonal antibody structure with an indication of variable region and constant region.

Based on the type of heavy chain, antibodies can be separated into five distinct classes: IgA, IgD, IgE, IgG, and IgM. IgG is the most often used form in antibody therapy due to the fact that IgGs interact with their associated type of Fc receptor, FcγR, found on natural killer (NK) cells as well as neutrophils, monocytes, dendritic cells, and eosinophils to mediate specialized functions such as antibody-dependent cellular cytotoxicity (ADCC), complement-dependent cytotoxicity (CDC) and antibody-dependent cellular phagocytosis (ADCP).[17,18] These three functions represent the indirect mechanism of action of mAbs and require the engagement of components of the host immune system. On the other hand, direct action is the consequence of the binding of

the antibody to the receptor and leads to the inhibition of proliferation and survival pathways. In 1997 rituximab was the first FDA-approved mAb for the treatment of B-cell lymphoma.[19] By targeting antigens identified as overexpressed on solid tumor cells, more mAbs have since demonstrated efficacy as cancer therapeutics. Today, mAbs directed to such targets as EGFR and HER2 see wide use in the clinic for the treatment of colorectal and breast cancers respectively (Fig4).

Name	Antigen	Format	Indications (Year of First Approval) [1]
		Unconjugated Antibodies	
Atezolizumab	PD-L1	Humanized IgG1	Bladder, Non-small cell lung (2016), and Triple-negative breast (2019) cancers (2019)
Avelumab	PD-L1	Human IgG1	Urothelial Carcinoma (2017) and Merkel Cell Carcinoma (2017)
Bevacizumab	VEGF	Humanized IgG1	Colorectal (2004), Non-small cell lung (2006), Renal (2009), Glioblastoma (2009), and Ovarian (2018) Cancers
Cemiplimab	PD-1	Human IgG4	Cutaneous squamous-cell carcinoma (2018)
Cetuximab	EGFR	Chimeric IgG1	Colorectal cancer (2004) and Head and neck squamous cell carcinoma (2006)
Daratumumab	CD38	Human IgG1	Multiple Myeloma (2015)
Dinutuximab	GD2	Chimeric IgG1	Neuroblastoma (2015)
Durvalumab	PD-L1	Human IgG1	Bladder Cancer (2017)
Elotuzumab	SLAMF7	Humanized IgG1	Multiple Myeloma (2015)
Ipilimumab	CTLA-4	Human IgG1	Melanoma (2011) and Renal cell carcinoma (2018)
Isatuximab	CD38	Chimeric IgG1	Multiple Myeloma (2020)
Mogamulizumab	CCR4	Humanized IgG1	Cutaneous T-cell lymphoma (2018)
Necitumumab	EGFR	Human IgG1	Non-small cell lung cancer (2015)
Nivolumab	PD-1	Human IgG4	Melanoma (2014), Lung (2015), and Renal (2018) cancers
Obinutuzumab	CD20	Humanized IgG2	Chronic lymphocytic leukemia (2013)
Ofatumumab	CD20	Human IgG1	Chronic lymphocytic leukemia (2014)
Olaratumab	PDGFRα	Human IgG1	Sarcoma (2016)
Panitumumab	EGFR	Human IgG2	Colorectal Cancer (2006)
Pembrolizumab	PD-1	Humanized IgG4	Melanoma (2014), Various (2015-)
Pertuzumab	HER2	Humanized IgG1	Breast cancer (2012)
Ramucirumab	VEGFR2	Human IgG1	Gastric cancer (2014)
Rituximab	CD20	Chimeric IgG1	B-Cell Lymphoma (1997)
Trastuzumab	HER2	Humanized IgG1	Breast cancer (1998)

Figure 4: FDA unconjugated mAbs approved for the treatment of cancer. Reproduced with permission from the corresponding paper.[17]

In addition, there is currently a multitude of other ways in which mAbs are employed in cancer therapy including antibody-drug conjugates. The conjugation usually occurs between the Fc portion of the mAbs and chemotherapy drugs, radioactive particles, toxins or even enzymes that will in turn convert a prodrug in its active form only in the proximity of target cells. Hence, in the combined form mAbs are used as a drug delivery system to direct the active molecule straight to the target reducing systemic side effects.

Recently, the most successful mAb-based strategies have moved away from targeting tumor antigens and instead focused on targeting immune cells in order to enhance their anti-tumor capabilities. One example is blinatumomab a bispecific antibody that both targets the tumor antigen CD19 and the activating receptor CD3 on T cells thus combining the direct targeting of tumor cells with the recruitment of cytotoxic T cells into the tumor microenvironment.[17,20]

Name	Antigen	Format	Indications (Year of First Approval) [1]
Antibody–Drug Conjugates (ADCs)			
Gemtuzumab ozogamicin	CD33	Humanized ADC	Acute myeloid leukemia (2000)
Brentuximab vedotin	CD30	Chimeric ADC	Hodgkin's lymphoma and Anaplastic large-cell lymphoma (2011)
Trastuzumab emtansine	HER2	Humanized ADC	Breast cancer (2013)
Inotuzumab ozogamicin	CD22	Humanized ADC	Acute lymphoblastic leukemia (2017)
Polatuzumab vedotin	CD79B	Humanized ADC	B-Cell Lymphoma (2019)
Enfortumab vedotin	Nectin-4	Human ADC	Bladder cancer (2019)
Trastuzumab deruxtecan	HER2	Humanized ADC	Breast cancer (2019)
Sacituzumab govitecan	TROP2	Humanized ADC	Triple negative breast cancer (2020)
Moxetumomab pasudotox	CD22	Mouse ADC	Hairy-cell leukemia (2018)
Ibritumomab tiuxetan	CD20	Mouse IgG1-Y90 or In111	Non-Hodgkin's lymphoma (2002)
Iodine (I131) tositumomab	CD20	Mouse IgG2-I131	Non-Hodgkin's lymphoma (2003)
Blinatumomab	CD19, CD3	Mouse BiTE	Acute lymphoblastic leukemia (2014)

[1] Indications and year of first approval for each antibody were accessed using the FDA drug database

Figure 5: FDA-approved antibody-drug conjugates Reproduced with permission from the corresponding paper.[17]

Antibody-dependent cell-mediated cytotoxicity

First described in 1965 by Erna Möeller, Antibody-dependent cell-mediated cytotoxicity (ADCC) is an immune mechanism by which effector cells expressing Fc receptors recognize and kill antibody-coated target cells expressing tumor-derived or pathogen-derived antigens on their surface. After the binding, effector cells induce cancer cells death via cytotoxic granule release, Fas signaling, and initiation of reactive oxygen species (Fig6).[21]

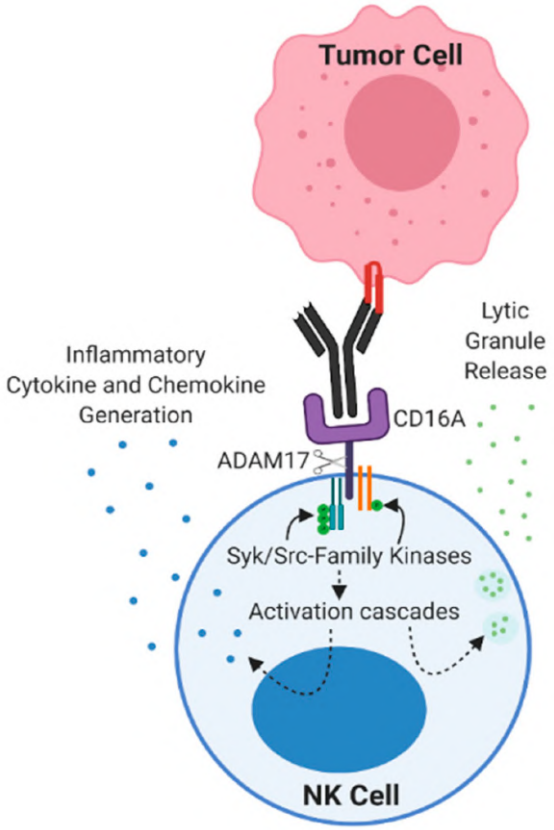

Figure 6: Schematic illustration of the antibody-dependent cell-mediated cytotoxicity mechanism. Reproduced with permission from the corresponding paper.[22]

Multiple myeloid lineage cells are capable of ADCC, however the major cell types known for catalyzing ADCC response are $CD56^{+}/CD3^{-}$ NK cells, neutrophils, monocytes and eosinophils. In the context of cancer immunotherapy, NK cells appear to be the main effector cell type *in vivo*. The clinical efficacy of many targeted mAb therapies has been demonstrated to be NK cell-dependent. NK bind the Fc portion of Abs through their Fc receptor CD16 (also called FcγRIII) which then triggers the degranulation of lytic granules, and the release of cytolytic perforin and granzymes, inducing target cell death.[23] Among monoclonal antibodies approved for clinical practice, trastuzumab, cetuximab, rituximab, and obinutuzumab are reported to elicit an effective ADCC response.[24]

Cetuximab

Cetuximab (CTX, trade name Erbitux®) is a human-mouse chimeric monoclonal antibody that is approved for the treatment of EGFR-expressing metastatic colorectal cancer (mCRC), metastatic non-small cell lung cancer, and head and neck cancer. CTX binds to the extracellular domain of EGFR with high affinity and competes with endogenous ligand binding. This competition, which results in the blockade of receptor-dependent signal transduction pathways, provides antitumor effects including cell-cycle arrest, induction of apoptosis, inhibition of angiogenesis, inhibition of metastasis, internalization and downregulation of the EGFR and enhancement of sensitivity to radio- or chemotherapy.[25] Moreover, CTX is also able to elicit the ADCC immune response which appears to be dependent on the EGFR expression. Clinical data confirm that CTX-mediated ADCC through NK cells may contribute to its anti-tumor activity *in vivo*.[24,26]

1.2.6 Immunotherapy strategies for glioblastoma and triple negative breast cancer

Glioblastoma induces significant systemic and intra-tumoral immunosuppression which led to disappointing results in phase III clinical studies with ICIs and vaccine therapy. The characterization of GBM as highly immunosuppressive with multiple mechanisms of immune evasion suggests that targeting only a single immunosuppressive pathway may not improve patient outcomes. Thus, many of the current studies are evaluating combinatorial strategies to find synergy between different immunotherapy approaches as well as between immunotherapy and the current standards of care for GBM (surgical resection, TMZ, and RT). Considering that GMB is highly heterogeneous, the second trend is focusing on personalized treatment. Among them, in 2019 two phase I trials have been conducted to explore a personalized patient-specific vaccine approach to treat glioblastoma.[27,28]

Several key characteristics make **triple negative breast cancer** more likely to respond to immunotherapy than other breast cancer subtypes. First TNBC has more tissue infiltrating lymphocytes, a higher level of PD-L1 expression on both tumor and immune cells and a greater number of non-synonymous mutations, which give rise to tumor-specific neoantigens that can be exploited for targeted therapies.[29] In recent years, agents targeting PD-1/PD-L1 axis have become the research focus for TNBC immunotherapy, and some PD-1/PD-L1 inhibitors, such as pembrolizumab and atezolizumab have shown encouraging clinical activity. At present several clinical studies are exploring the potential to combine immune checkpoint inhibitors and chemotherapy to treat both metastatic and early-stage TNBC. In 2019 FDA approved the combination of Atezolizumab and nab-Paclitaxel for therapy-naïve patients with PD-L1-positive advanced

TNBC.[30,31] Others immunotherapy strategies include CTLA-4 inhibitors, CAR-T cell therapy and tumor vaccines. Up to now, critical areas in need of development include immunotherapies for PD-L1–negative metastatic TNBC and TNBC refractory to prior PD-1/L1 therapies, as well as strategies that minimize immune-related toxicity (Fig7).[29]

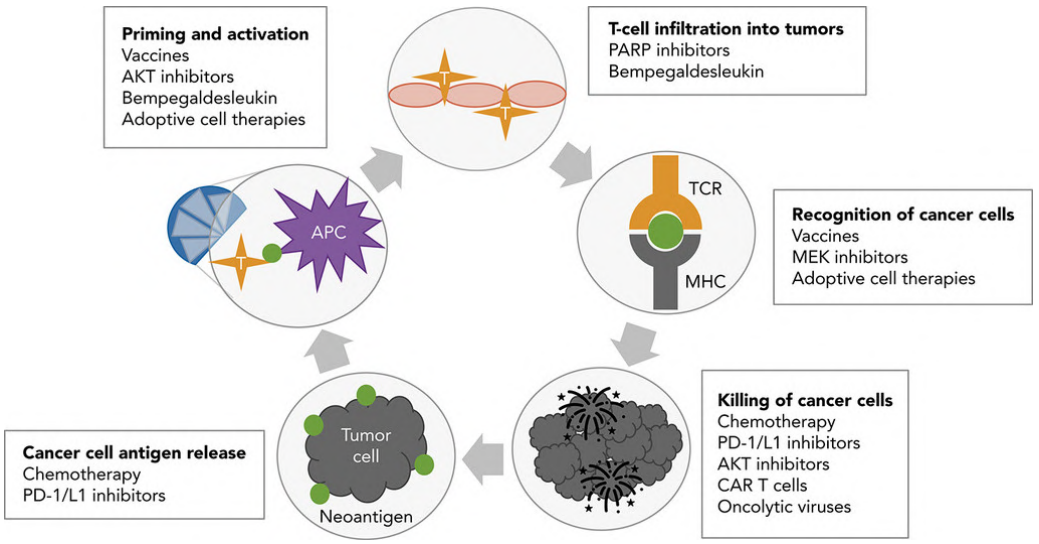

Figure 7: Immunotherapy and combination agents in triple-negative breast cancer. Reproduced with permission from the corresponding paper.[29]

1.3 3D cultures

Currently, the majority of cell-based high-throughput screening is being carried out on cultured cells propagated in two dimensions (2D) on plastic surfaces optimized for tissue culture. Even if 2D cultures represent an essential first step for preliminary tests and results as they are the most straightforward and low-cost approach, compelling evidence suggests that cells cultured in these non-physiological conditions are not representative of cells residing in the complex

microenvironment of a tissue. For this reason, 3D cell cultures have acquired considerable attention over the last two decades becoming a versatile tool, especially for cancer research, due to their intrinsic capacity to better mimic the tumor microenvironment complexity. 3D models are widely used also in the investigation of intracellular interactions and cell differentiation, evaluation of substance toxicity, efficacy of potential drugs and examination of nanoparticles.[32] Currently, the growth of 3D cell cultures can be generated using several protocols, which allows 3D models to be classified into scaffold- and non-scaffold-based approaches as well as hybrid 3D culture models in which formed spheroids are incorporated into a 3D polymeric scaffold. Considering that each one of these systems has its own strengths and limitations one will need to choose the most appropriate 3D cell culture model for a specific application. The scaffold-based 3D cultures require an external support to be engineered to mimic the extracellular matrix, and this allows cells to anchor to the support, to proliferate, and migrate across scaffold interstices. Thanks to these characteristics, cells acquire typical *in vivo* tumor hallmarks, along with the specific distribution of an *in vivo* setting. Scaffolds can be of biological origin or they can be synthetically engineered to mimic key properties of ECM such as stiffness, charge or adhesive moieties. Synthetic materials that could be applied as hydrogels are polyethylene glycol (PEG), polyvinyl alcohol (PVA), poly(hydroxyethyl methacrylate) (polyHEMA), and polycaprolactone (PCL). Furthermore, natural polymers and proteins can form hydrogels, e.g., alginate, collagen, chitosan, hyaluronan, dextran, and fibrin.[33,34]

In non-scaffold-based platforms, tumor cells can aggregate and form so-called tumor spheroids. This type of culture can promote cancer-cell self-assembly by increasing interactions between the cells, adhesion to the support, and by

amplifying cellular aggregation. Spheroids' size depends on the initial number of cells seeded and they can be grown to a size that can display characteristics similar to tumor tissue. Indeed, 3D models with diameters above 400 µm possess gradients of O_2 and nutrients similar to those that exist in tumors, with O_2 and nutrient supply progressively diminishing with distance from the outer layers. These gradients result in different environmental conditions that significantly influences metabolic state, proliferative capacity, drug resistance, and tumor potential. As a direct consequence of the gradients present in tumors, and reflected in 3D models, cancer cells exist in a more proliferative state in the outer layers; however, cancer cells of the inner layers can exist in quiescent or necrotic states (Fig8).[32,35]

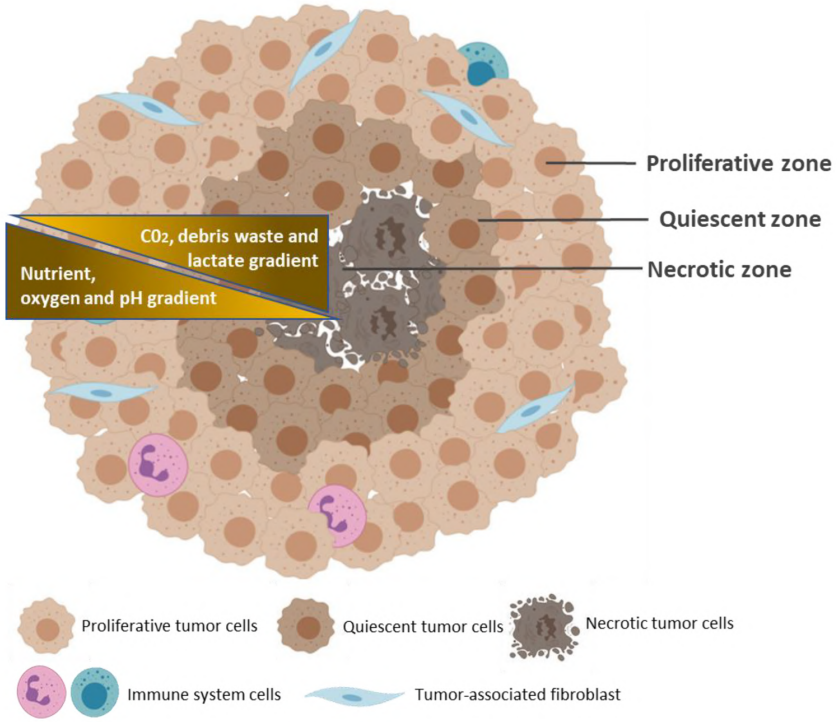

Figure 8: Typical structure of a multicellular tumor spheroid. The geometric rearrangement of the cells within the spheroid forms three concentric zones of

heterogeneous cell populations: an external proliferating zone (Proliferative zone); a middle zone of quiescent cells (Quiescent zone), and an internal zone of necrotic cells (Necrotic zone). These cell layers are caused by the gradients of nutrients, oxygen, and pH (yellow), from the outside to the center of the spheroid, and by the gradients of CO_2, waste, and lactate, from the center to the outside. Reproduced with permission from the corresponding paper.[36]

Tumor spheroids model can derive from established cell lines or can be obtained through *ex vivo* propagation of tumors from individual patients forming the so-called organoids. They can be obtained with different culture techniques that result in self-organizing, self-renewing 3D cultures derived from primary tissue, embryonic stem cells, or induced pluripotent stem cells that have similar functionalities as the tissue from which the cells originate. Organoids derived from patients retain their genome over time and can be used to perform drug screens and facilitate drug development in a patient-centered manner.[34,37]
Microfluidic devices and micropatterned plates with ECM components, and cultures in which formed spheroids or organoids are embedded in ECM scaffolds, can form hybrid culture systems that combine the advantages of both systems to form a complex microenvironment for 3D cell culture.[34]

2. Aim of the project

In this project, we exploit the external residues of a recombinant form of human apoferritin, all made of H-chains subunits (HFn) for the conjugation of the monoclonal antibody cetuximab. After demonstrating that HFn is an efficient carrier to enhance the blood-brain barrier (BBB) crossing of mAbs without the loss of their antitumoral activity in 2D tumor models[38], in this study we focus on the evaluation of the anticancer activity of HFn-CTX nanoconjugate in 3D cellular models. As a 3D model, we choose to use spheroids because they are able to closely mimic the main features of human solid tumors, namely their spatial architecture, cellular layered assembling, physiological responses, and nutrient gradients.[36]

The aims of this work were to produce a recombinant form of human apoferritin with a reduced endotoxin content; to obtain a reproducible 3D cancer model out of two different cell lines, one of glioblastoma and the other of triple negative breast cancer; to optimize the fluorescence labeling protocol of HFn-CTX in order to study its penetration and biodistribution through *in vitro* and *in vivo* models and, finally, to investigate the ability of HFn-CTX to trigger cancer cells apoptosis after the activation of the ADCC response in the presence of immune systems cells.

3. Materials and Methods

Production of HFn in E. coli and purification

The production of heavy chain apoferritin (HFn) was carried out following a protocol set up in our lab.[39] Briefly, Escherichia coli ClearColi® BL21(DE3) strain (Lucigen Ltd. UK) was transformed with pET30b/HFn plasmid and grown at 37 °C in Luria Bertani kanamycin medium until optical density (OD)600nm = 0.6. Then, the cells were induced with 1 mM of isopropyl β-D-1-tiogalactopiranoside (IPTG) for 3h. After they were collected, washed with phosphate-buffered saline (PBS), and resuspended in a lysis buffer with lysozyme and DNase I. After the sonication, the crude extract was heated at 70 °C for 15 min and centrifuged. The supernatant was loaded onto diethylaminoethanol (DEAE) Sepharose anion exchange resin, pre-equilibrated with 2-(N-Morpholino)ethanesulfonic acid potassium salt (K-MES) 20 mM, pH 6.0. In order to elute the purified protein, a stepwise NaCl gradient was used. The fractions were analyzed by Sodium Dodecyl Sulphate - PolyAcrylamide Gel Electrophoresis (SDS-PAGE) using 12% (v/v) polyacrylamide gels. Various step of washing with PBS were carried out using Amicon filter (100 kDa MWCO) to obtain pure HFn. Protein concentration was determined by both using the Comassie Plus Protein Assay Reagent (Thermo Fisher Scientific, MA, USA) and measuring absorbance at 280 nm. The purity of the preparation was assessed by measuring the absorbance ratio 260/280 with a UV-vis spectrophotometer (NanoDrop™ 2000 Spectrophotometer, Thermo Fisher Scientific, MA, USA).

LAL test

To test the endotoxin (ETX) content in the different protein preparations it was used the Limulus Amebocyte Lysate (LAL) kinetic turbidimetric assay according to the manufacturer's instruction (Charles River Microbial Solutions Ltd., Dublin, Ireland). A standard curve was prepared fresh before every analysis by using standard ETX (E120, Charles River Microbial Solutions Ltd., Dublin, Ireland) in the range between 50 and 0.005 EU mL^{-1}. Different sample dilutions were prepared in pyrogen-free tested water according to the initial ETX content: the purpose was to obtain samples with a final ETX content falling within this range. Results were considered reliable only when spike recoveries were between 50% and 200% (spike value = 5 EU mL^{-1}). The same pyrogen-free tested water used for dilutions served also as blank, while PBS was tested to exclude any interference with the LAL readings.

HFn-CTX conjugation reaction

The conjugation reaction was performed by adapting the protocol by *Falvo et al* to our purpose.[40] Briefly, amine-containing CTX and sulfhydryl-containing HFn were covalently conjugated together by a heterobifunctional crosslinker with N-hydroxysuccinimide (NHS) ester and maleimide (Mal) groups (Malhex-CONH-PEG-NHS, 5 kDa, Rapp Polymere Gmbh, Tubingen). mAb molecules reacted first with a 20-fold molar excess of the crosslinker in phosphate buffer (PBS) pH 7.5 at room temperature for 1 h. After the incubation time, unreacted species were removed by washing with PBS buffer in 50 kDa centrifugal filter devices (Amicon, Millipore Corporate) and finally refine on size exclusion chromatography column (Zeba™ Spin Desalting Columns, Thermo Fisher Scientific, MA, USA).

Then, HFn molecules were added at a final HFn:mAb molar ratio of 1:1 and incubated overnight at 4 °C under stirring. At the end of the reaction, large aggregates produced were removed by centrifugation (12,000xg for 30 min at 4 °C), while the nanoconjugate-containing supernatant was collected and purified using a size exclusion chromatography (SEC-FPLC) equipped with a Superose 6 increased 10/300 GL column (GE Healthcare) equilibrated with PBS. The eluted fractions were then characterized by SDS-PAGE analysis, western blot and dynamic light scattering (DLS).

Fluorescence labeling of HFn-CTX

To obtain a double-labeled nanoconjugate CTX and HFn were labeled with Alexa Fluor™-647 NHS Ester (AF647, Thermo Fisher Scientific, MA, USA) and Alexa Fluor™-488-5-TFP-ester (AF488, Thermo Fisher Scientific, MA, USA) respectively.

HFn labeling with AF488: Following manufacturer instructions, a Zeba™ Spin desalting column (7 kDa) was used to exchange HFn buffer to 0.1 M $NaHCO_3$ pH 8.0. Then, Alexa Fluor™-488-5-TFP-ester (20 mg mL^{-1} in DMSO) (Thermo Fisher Scientific, Waltham, MA, USA) was added to the HFn solution (5 mg mL^{-1}) to obtain a molar dye/protein ratio of 50 and kept under stirring for 30 min at RT and then at 4 °C overnight. At the end of the incubation, the unreacted dye was removed with a Zeba™ Dye and Biotin Removal Columns (7 kDa, Thermo Fisher Scientific, Waltham, MA, USA), using 50 mM potassium phosphate, pH 7.2, and 150 mM NaCl as the final buffer. To complete protein purification, HFn-AF488 was also run onto a size exclusion gel filtration chromatography (SEC-FPLC). The degree of labeling was calculated as dye concentration (M)/protein concentration (M), based on UV–Vis spectroscopy; 280 nm and 488 nm

absorbances were used, respectively, for the quantification of the protein and the dye, using the following formulas that subtract the contribution of the dye at 280 nm:

$$\text{Protein concentration (M)} = \frac{[A_{280} - (A_{max} * 0.11)] * df}{\varepsilon_{HFn} * l}$$

where Amax is absorbance (A) of a dye solution measured at the wavelength maximum (λmax) for the dye molecule, 0.11 is the correction factor recommended by the supplier to remove the contribution of Alexa Fluor™-488-5-TFP-ester from the 280 nm absorbance, df is the dilution factor which represent the extent (if any) to which the protein:dye sample was diluted for absorbance measurement, l (optical path length) is 0.1 cm and εHFn is 458,340 M^{-1} cm^{-1} (calculated by ProtParam).[41]

$$\text{Degree of labelling (DOL)} = \frac{\text{moles Alexa 488}}{\text{moles HFn}} = \frac{A_{max} * df}{\varepsilon_{Alexa\ 488} * l * M}$$

where εAlexa488 (molar extinction coefficient of Alexa Fluor™-488-5-TFP-ester) is 71,000 cm^{-1} M^{-1}, l is 0.1 cm and M is the protein concentration.

CTX labeling with AF647: A Zeba™ Spin desalting column (7 kDa, Thermo Fisher Scientific, Waltham, MA, USA) was used to exchange CTX buffer to 0.1 M $NaHCO_3$ pH 8.0. Then, Alexa Fluor™-647-NHS-ester (10 mg mL^{-1} in DMSO) (Thermo Fisher Scientific, Waltham, MA, USA) was added to the CTX solution (5 mg mL^{-1}) to obtain a molar dye/protein ratio of 10. Before starting the reaction, a 20-fold molar excess of the PEG crosslinker was added to the reaction mix because both AF647 and PEG crosslinker compete to bind to the amine groups of CTX. Then the reaction was kept under stirring for 2.5 hours at RT. At the end of the incubation, the unreacted dye was removed with a Zeba™ Dye and Biotin Removal Columns (7 kDa, Thermo Fisher Scientific, Waltham, MA, USA), using

50 mM potassium phosphate, pH 7.2, and 150 mM NaCl as final buffer. To complete protein purification and remove the excess of PEG, a size exclusion gel filtration chromatography (SEC-FPLC) was performed. The degree of labeling was calculated as dye concentration (M)/protein concentration (M), based on UV–Vis spectroscopy; 280 nm and 647 nm absorbances were used, respectively, for the quantification of the protein and the dye, using the formulas reported above (0.03 is the correction factor recommended by the supplier to remove the contribution of Alexa Fluor™-647-NHS-ester from the 280 nm absorbance, εCTX is 217,440 M^{-1} cm^{-1} and εAlexa647 is 239,000 M^{-1} cm^{-1} as calculated by ProtParam).

Cell cultures

U-87 MG cell line was used as EGFR-positive models of glioblastoma primary brain cancer, while MDA-MB-231 cell line was used as EGFR-positive model of metastatic triple negative breast cancer.

U-87 MG was cultured in Dulbecco's Modified Eagle's Medium (DMEM) supplemented with 10% fetal bovine serum (FBS), 2mM L-glutamine, penicillin (50 UI mL^{-1}) and streptomycin (50 mg mL^{-1}). MDA-MB-231 cells were cultured in Minimum Essential Medium (MEM), supplemented with 10% FBS, 2mM L-glutamine, penicillin (50 UI mL^{-1}) and streptomycin (50 mg mL^{-1}).

All cell lines were maintained at 37 °C in humidified atmosphere containing 5% CO_2 and sub-cultured prior to confluence using trypsin-EDTA (Euroclone®).

Spheroids generation

U-87 MG: Monolayer cells were detached with trypsin-EDTA to generate a single-cell suspension. The cell number was determined using a Bürker

chamber, and the cell suspension was diluted in complete medium to $6x10^4$ cells mL^{-1}. A volume of 100 µl (=6000 cells) of the cell suspension was added to each well of an ultra-low attachment Nunclon™ Sphera™ 96-well plate (Thermo Fisher Scientific, MA, USA). The spheroid formation was initiated by centrifugation of the plates at 340xg for 10 min using an Eppendorf 5810 centrifuge (Eppendorf AG, Hamburg) with swinging buckets. The plates were incubated under standard cell culture conditions at 37 ˚C and 5% CO_2 in humidified incubators for 5 days.

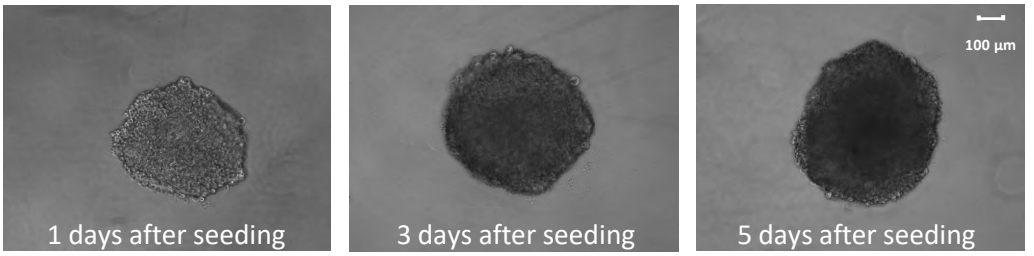

Figure 1: U-87 MG spheroids 1, 3 and 5 days after seeding. Images acquired with PAULA Cell Imager (Leica Microsystems).

MDA-MB-231: Monolayer cells were detached with trypsin-EDTA to generate a single-cell suspension. The cell number was determined using a Bürker chamber, and the cell suspension was diluted in ice-cold medium to $2.5x10^4$ cells mL^{-1}. The Cultrex® (3-D Culture Matrix Reduced Growth Factor BME, R&D SYSTEM) was thawed on ice overnight and added at a final concentration of 2.5% with ice-cold pipette tips to the cell suspension. A volume of 200 µl (=5000 cells) of the cell suspension was added to each well of an ultra-low attachment Nunclon™ Sphera™ 96-well plate (Thermo Fisher Scientific, MA, USA). The spheroid formation was initiated by centrifugation of the plates at 340xg for 10 min using an Eppendorf 5810 centrifuge (Eppendorf AG, Hamburg) with

swinging buckets. The plates were incubated under standard cell culture conditions at 37 ˚C and 5% CO_2 in humidified incubators for 5 days.

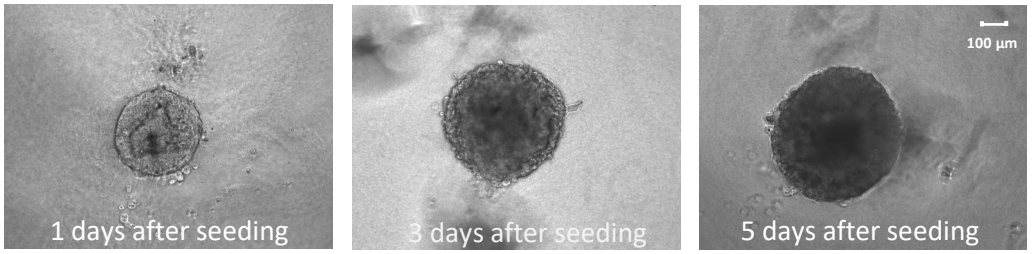

Figure 2: MDA-MB-231 spheroids 1, 3 and 5 days after seeding. Images acquired with PAULA Cell Imager (Leica Microsystems).

Effector cells isolation

Peripheral blood mononuclear cells (PBMCs) were obtained by centrifugation on Ficoll-Paque of blood samples from healthy donors (30 min at 1,500 rpm without brakes). At the end the PBMCs layer was carefully transferred to a new 50 mL tube, diluted with PBS and centrifuged for 6 min at 1,400 rpm. Then the supernatant was eliminated to remove platelets and the procedure was repeated four times decreasing the centrifugation speed up to 1,000 rpm. Washed PBMCs were resuspended in RPMI-1640 medium with 10% of decomplemented FBS and 1,000 U mL^{-1} IL-2 (BioLegend, San Diego, CA, USA) for 24 h at 37 °C. The described procedure was approved by Ethical Committee of the University of Milano-Bicocca (prot. 0138485/21, 15th November 2021) after the submission of the project together with informed consent by the healthy volunteers.

Live image microscopy of ADCC

First spheroids were transferred from an ultra-low attachment plate to 1.5 mL Eppendorf tubes (4 spheroids/tube). Then culture medium was removed, and spheroids were incubated with 10 µM Höechst (Thermo Fisher Scientific, MA, USA) solution for 30 min at 37 °C. After the incubation Höechst solution was removed, and spheroids were washed with 500 µL of PBS before adding 50 µL of RPMI culture medium without FBS containing 10 µg mL^{-1} of CTX or HFn-CTX. The content of each eppendorf tube was transferred into a 96-well black plate and incubated at 4 °C for 30 min. Then CellTracker™ Deep Red Dye (Thermo Fisher Scientific, MA, USA) pre-stained effectors cells were added to each well maintaining an effector:target (E:T) ratio of 2:1. Before the acquisition, 2 µM CellEvent™ Caspase-3/7 Green Detection Reagent (Thermo Fisher Scientific, MA, USA) was added to each well and images were acquired every 1 h for 52 h using Operetta CLS High Content Analysis System (Perkin Elmer, Walthman, MA, USA). The green fluorescence intensity related to the caspase production was then quantified using Harmony software connected to the instrument.

Endpoint ADCC assay

The ADCC apoptosis effect on target cells was quantitatively evaluated using The Caspase-Glo® 3/7 3D (Promega Corporation, Madison, WI, USA). After 5 days of growth in the ultra-low attachment plate wells, spheroids were first coated with free or nanoformulated CTX (10 µg mL^{-1}) or with HFn (34 µg mL^{-1}) for 30 min at 4 °C in RPMI culture medium without FBS. After coating, IL-2-activated PBMCs were added onto target cells at an effector:target (E:T) ratio of 2:1 and incubated 24, 30 or 48 h at 37 °C. Then 100 µL of Caspase-Glo® 3/7 3D Reagent

were added to each well and the plate was incubated at room temperature for at least 30 minutes. At the end of the incubation luminescence, which is proportional to the amount of caspase activity present, was measured by EnSight™ multimode plate reader (Perkin Elmer, Walthman, MA, USA).

CD16 shedding assay

After 5 days of growing, twelve U-87 MG and MDA-MB-231 spheroids for each condition were transferred in eppendorf tubes to remove culture medium which was then replaced with RPMI culture medium without FBS with 10 µg mL^{-1} of CTX or HFn-CTX or with 34 µg mL^{-1} of HFn. The content of each tube was then transferred in a 48-well plate and incubated for 30 min at 4°C. After the incubation, IL- 2-activated PMBCs were added at an effector:target (E:T) ratio of 2:1 and incubated for 48 h at 37 °C. Then the volume contained in each well was transferred again in eppendorf tubes to better separate spheroids from effectors cells. The supernatant containing effectors was collected and transferred in FACS tubes. Effector cells were centrifuged for 5 min at 1,300 rpm and washed once with PBS before adding the AlexaFluor 488 anti-human CD16 antibody (clone 3G8; BioLegend) and the Pacific Blue™ anti-human CD45 antibody (clone 2D; BioLegend) with a dilution of 1:100. The antibody was incubated 5 minutes in the dark. The amount of the not cleaved CD16 on effector cells was evaluated by cytofluorimetric analysis. 10,000 events were acquired for each sample, using flow cytometry equipped with a doublet discriminator module (Gallios™ Flow Cytometer - Beckman Coulter Inc.) and data were analyzed by Kaluza analysis software.

Uptake experiments

For the confocal live imaging experiment twelve spheroids for each condition were transferred from an ultra-low attachment plate to 1.5 mL Eppendorf tubes. Then culture medium was removed, and spheroids were incubated with 10 µg mL^{-1} of labeled CTX or HFn-CTX or 34 µg mL^{-1} of HFn for 3.5 hours at 37 °C. At the end of the incubation, the culture medium was removed, and spheroids were incubated with 10 µM Höechst (Thermo Fisher Scientific, MA, USA) solution for 30 min at 37 °C. After the incubation, Höechst solution was removed, spheroids were washed with 500 µL of PBS and transferred to petri dishes with glass bottoms (Greiner Bio-One). Images were acquired using a Nikon confocal microscope (A1 series).

For the cytofluorimetric uptake experiment twelve spheroids for each condition were transferred from an ultra-low attachment plate to 1.5 mL Eppendorf tubes. Then culture medium was removed, and spheroids were incubated with 10 µg mL^{-1} of labeled CTX or HFn-CTX or 34 µg mL^{-1} of HFn for 3.5 hours at 37 °C. At the end of the incubation, spheroids were trypsinized to obtain a single cells suspension and analyzed by flow cytometry. 10,000 events were acquired for each sample, using flow cytometry equipped with a doublet discriminator module (Gallios™ Flow Cytometer - Beckman Coulter Inc.) and data were analyzed by Kaluza analysis software.

Animals and tumor xenograft production

For the *in vivo* preliminary experiment, five female NOD/scid common gamma chain-deficient mice (NSG mice) purchased by Envigo (Bresso, Italy) were maintained in a fully equipped facility and their conditions were observed daily.

Animals were cared according to the guidelines of the Italian Ministry of Health. All experiments were conducted under an approved protocol (authorization n° 92/2022-PR). Luciferase-transfected MDA-MB-231 cells were cultured in DMEM high glucose supplemented with 10% fetal bovine serum, 2 mM L-glutamine, penicillin (50 IU/mL) and streptomycin (50 mg/mL), 0.1 mM MEM Non-essential Amino acids (NEAA) and then inoculated subcutaneously into the mammary fat pad of each mouse in a mixture (1:1 volume) of $3x10^6$ cells and Matrigel (Corning® Matrigel® Growth Factor Reduced (GFR) Basement Membrane Matrix, Phenol Red-free, LDEV-free) with a final volume of 100 µL. The state of health and behavior of each animal was observed daily, and the weight was monitored every three days until the tumors reached a dimension around 150 mm^3 after 4 weeks from inoculation, measured by caliber.

Xenografts growth was also evaluated by Bioluminescence (BLI) *in vivo*, using an IVIS Lumina II imaging system (Perkin Elmer), with an exposure time of 5 s. BLI images were acquired 5, 8 and 11 min after the peritoneal injection of 260 µg kg^{-1} luciferin (D-Luciferin potassium salt, Perkin Elmer).

Tumor targeting and biodistribution of HFn-Alexa488-CTX-Alexa647 *in vivo* and *ex vivo*

To observe the biodistribution of HFn-CTX into the mice body, the nanoconjugate was labeled as previously described. NSG mice bearing MDA-MB-231-L cells were immobilized in a restrainer (2 biological instruments) to be injected in the tail vein with HFn-AF488-CTX-AF647 nanovector (5 mg kg^{-1} body weight). PBS was used as a control. Epifluorescence images were obtained 3 h post-injection by placing the anesthetized animals in the IVIS system at 37 °C.

Images were acquired with a Cy5.5 emission filter, while excitation was scanned from 570 to 640, and mice autofluorescence was removed by spectral unmixing. The instrument setup for FLI acquisition is Fstop 4 and medium binning, T exposure 10 sec. After *in vivo* acquisitions, mice were sacrificed, and organs were dissected and analyzed in IVIS system. All the epifluorescence (Epf) intensity values were normalized after subtracting Epf values obtained by mice injected with PBS. Final results are expressed as mean ± s.e.

Statistical analysis

Statistical analyses were conducted using either one-way or two-way Anova. All plots show mean values ± standard deviation (s.d.) or standard errors (s.e.). All tests assumed normal distribution and the statistical significance threshold was set at $p<0.05$.

4. Results

HFn production and characterization

The H monomer of human ferritin was cloned and expressed in E. coli ClearColi™ BL21(DE3) strain as previously reported.[39] According to the producer, these cells have a modified lipopolysaccharide (LPS) named Lipid IV_A that does not trigger the endotoxic response in human cells. ClearColi cells lack outer membrane agonists for human Toll-like receptor/myeloid differentiation factor 2 (hTLR4/MD-2) activation; therefore, activation of hTLR4/MD-2 signaling by ClearColi is several orders of magnitude lower compared to E. coli wild-type cells. In ClearColi cells, two of the secondary acyl chains of the normally hexa-acylated LPS have been deleted, eliminating a key determinant of endotoxicity in eukaryotic cells (Fig.1). The six acyl chains of the LPS are the trigger that is recognized by the Toll-like receptor 4 (TLR4) in complex with myeloid differentiation factor 2 (MD-2), causing activation of NF-ƙB and production of proinflammatory cytokines.[42] This strain has therefore been shown in multiple studies to be “endotoxin free” and can be used to produce therapeutics without downstream endotoxin removal steps.[43,44]

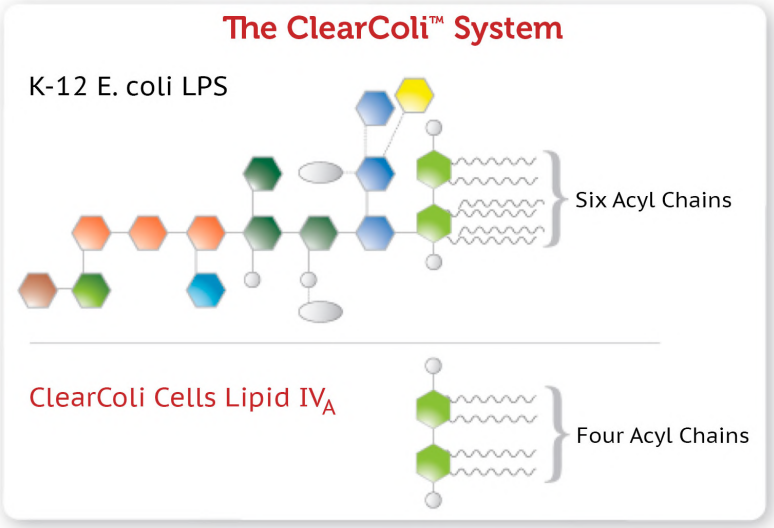

Figure 1: The LPS of normal E. coli cells compared to the genetically modified Lipid IV_A from ClearColi cells. In ClearColi, the oligosaccharide chain is deleted, and two of the six acyl chains are removed to disable the endotoxin signal.[42]

After plasmid insertion, ClearColi cell culture conditions were optimized testing different Isopropyl β-D-1-thiogalactopyranoside (IPTG) concentrations (0.5 mM and 1 mM) and induction period (2, 3 or 5 hours). After a sodium dodecyl sulfate-polyacrylamide gel electrophoresis (SDS-PAGE) and Western Blot performed to verify the presence of HFn, the selected conditions were IPTG 1 mM and 3h of growing before harvesting the cells (Fig.2).

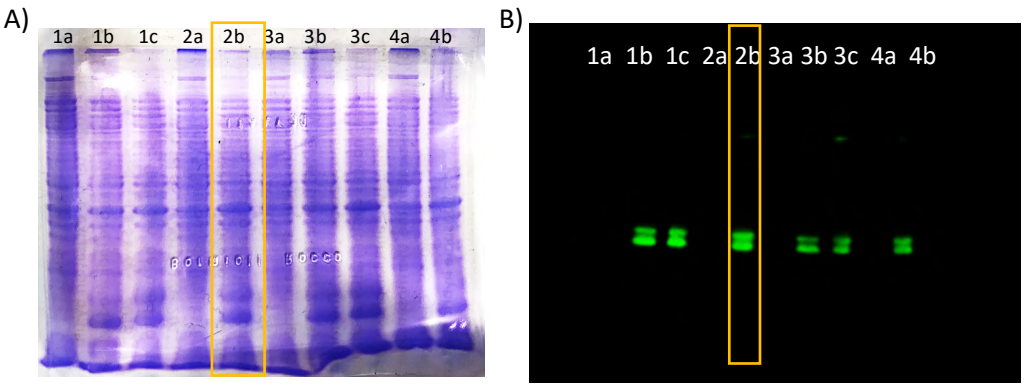

Figure 2: Culture condition optimization. A) The presence of HFn after the different culture conditions tested was checked via 12% SDS-PAGE separation. **1a)** OD_{600} 0.8 sample 1; **1b)** 2h IPTG 1 mM; **1c)** 5h IPTG 1 mM; **2a)** OD_{600} 0.8 sample 2; **2b)** 3h IPTG 1 mM; **3a)** OD_{600} 0.8 sample 3; **3b)** 2h IPTG 0.5 mM; **3c)** 5h IPTG 0.5 mM; **4a)** OD_{600} 0.8 saple 4; **4b)** 3h IPTG 0.5 mM. B) Western Blot analysis. For this analysis membranes were incubated overnight with rabbit-monoclonal antibody against ferritin heavy chain (EPR3005Y; Abcam) at 1:1000 dilution in 5% BSA in TBS with 0.1% tween 20. After, membranes were washed thrice with TBS with 0.1% tween 20 and reacted 1 h with rabbit polyclonal anti-human IgG secondary antibody (A80-118P; Bethyl) at 1:20000 dilution in 5% BSA in TBS with 0.1% tween 20. After washing the membranes again, the bound antibodies were revealed using ECL star reagent (Euroclone) and the chemiluminescence signal was detected using Odyssey Fc Imaging System (Licor). In both figures, the yellow rectangle identifies the selected condition of IPTG 1 mM for 3h.

Then HFn was purified as reported in the Methods section. A good level of purity was observed in purified fractions showing a 21 kDa band in 12% SDS-PAGE corresponding to HFn monomer (Fig3). To confirm that the HFn obtained was safe to use in presence of human immune systems cells, a Limulus amebocyte lysate (LAL) assay was performed. The LAL assay is an FDA-approved method for

the detection of endotoxins and is the most common assay used. It is based on the ability of a particular molecule found in the amebocytes of the Limulus species to react with endotoxin.[45] However, the LAL assay is an inappropriate method to discriminate between endotoxically active LPS and endotoxically inactive lipid IV_A. As such, false positive results are due to the lack of specificity of the assay that recognizes a wider spectrum of LPS/lipid A variants than the central cellular endotoxin sensor system of the human immune cell system.[42,43] Considering that endotoxins concentration is generally extremely low if compared to the concentration of the target protein, the overall amount of endotoxin is normally expressed in EU (endotoxins unit), where 1 EU approximately corresponds to 0.1/0.2 ng.[45] The results of the test showed that HFn produced with ClearColi technology had an endotoxic content of 0.46 EU μg^{-1} of protein, in line with the endotoxin content obtained by the producer of the strain.[42] This residual EU measurement could be due to the non-specific nature of the assay and even in the presence of EU levels above normal thresholds recommended by FDA, the actual stimulating effects from ClearColi-derived proteins were not significant. This statement will be further verified with a measurement of TLR stimulation as assessed by NF-ƙB activation in HEK293 cells or Human Macrophage assays prior to performing *in vivo* ADCC experiments. If HFn turns out to be immunogenic, the residual endotoxin content will be removed with Triton X-114 as described in the literature.[45]

However, the endotoxin content of HFn obtained with ClearColi strain is much lower than that of a HFn produced with an unmodified coli strain (HFn STD) (Fig.3).

A) KDa

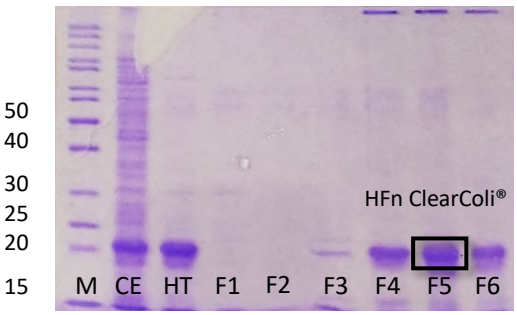

B)

Samples	EU/µg
HFn STD	89.27
HFn ClearColi®	0.46

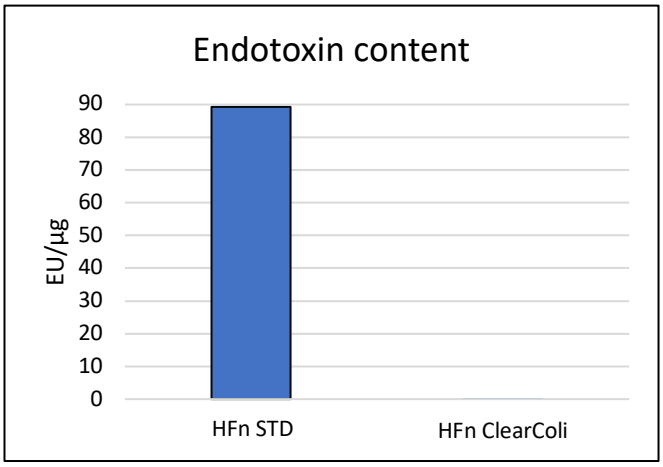

Figure 3: HFn purification and LAL test results. A) SDS-PAGE obtained after HFn purification, starting from the left: protein marker (first lane), crude extract (CE, second lane), heat treated (HT, third lane), fraction 1 to 6 (lane 4 to 9). B) endotoxin quantification obtained with LAL assay.

Synthesis and characterization of mAbs-conjugated HFn nanoparticles

After purification, HFn nanocages were used for the conjugation with the monoclonal antibody cetuximab (CTX), as previously reported.[38,40] Briefly, a PEG-based heterobifunctional crosslinker (MW_{PEG} ≈ 5000 Da) was used to

anchor the monoclonal antibody on HFn surface in a two steps reaction. In the first step, mAb react with a molar excess of PEG, which binds to the amine residues on mAb molecules thanks to the N-hydroxysuccinimide (NHS) ester group. In the second step, after the addition of HFn to the reaction mix, the PEG linker anchors the mAb on HFn surface thanks to the binding between PEG maleimide (Mal) groups and sulfhydryl residues on HFn (Fig1). Next, reaction products were separated and characterized by size exclusion chromatography (SEC-FPLC) that allowed identifying a peak for protein complex and others for each unreacted species. After FPLC elution we qualitatively confirmed the presence of both protein species inside our complex by SDS-PAGE electrophoresis gel and western blot analysis and we performed a DLS analysis to measure the hydrodynamic diameter of HFn-mAb nanoconjugate obtaining an overall size below 30 nm (HFn-CTX = 28.8 ± 10.8 nm). Moreover, the presence of 1 non-oriented CTX immobilized on the surface of HFn was confirmed using fluorescence calibration curves.[38]

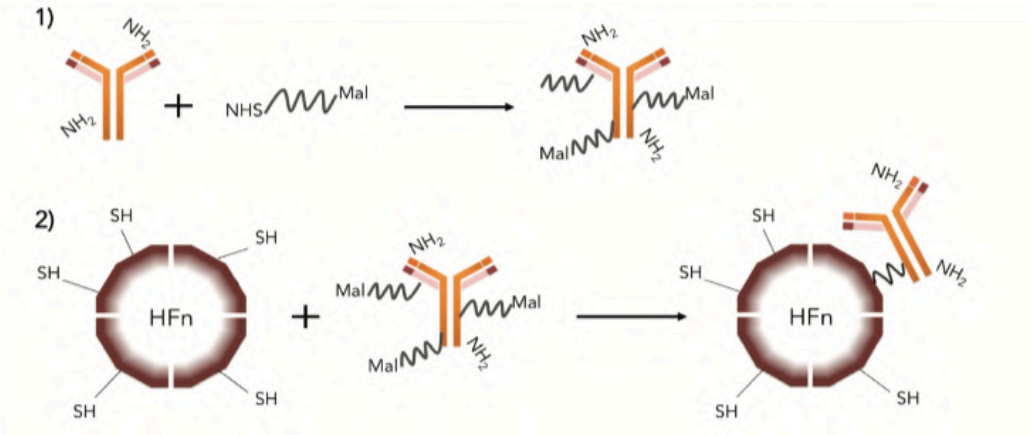

Figure 1: Schematic representation of the two steps reaction used for NPs synthesis. First PEGylation of the mAb occurs (1) followed by conjugation with HFn nanoparticles (2).[38]

Fluorescence labeling of HFn and CTX

In order to evaluate the nanoconjugate penetration *in vivo* and *in vitro,* we decided to label HFn and CTX with two fluorophores to follow the penetration of both protein species simultaneously. CTX and HFn were labeled with AlexaFluor647 (AF647) and AlexaFluor488 (AF488), respectively, before performing the conjugation reaction described above. These dyes were selected to prevent interferences with each other because of the almost total absence of spectra overlapping; in addition, they are resistant to photobleaching and pH-insensitive over a wide concentration range (Fig.2).

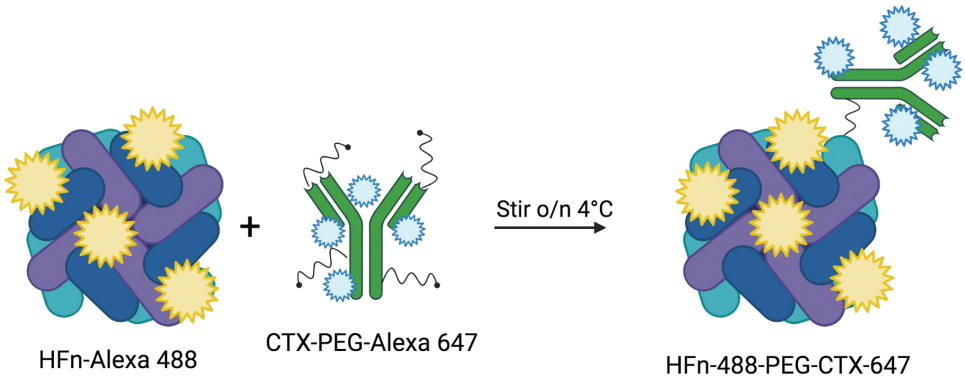

Figure 2: Schematic representation of reaction used for double label HFn-CTX nanoconjugate.

HFn fluorescence labeling optimization

To find the optimal labeling condition, we explored different HFn/Alexa fluorophores molar ratios, different protein concentrations in the reaction mix, and different reaction conditions. In particular, tests were carried out with a molar ratio of 1:2.5, 1:6, 1:30, 1:50 and 1:100. Protein concentration was set at 2 mg mL^{-1} or at 5 mg mL^{-1} and the reaction mix was maintained for 3 hours at room temperature with continuous stirring or for 30 minutes at room

temperature and then at 4 °C overnight always with continuous stirring. All the reactions were performed using sodium bicarbonate buffer ($NaHCO_3$, 0,1 M, pH 8.0). Table 1 summarizes the reaction condition tested.

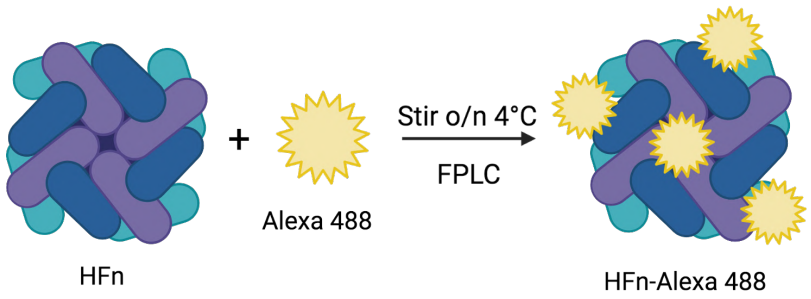

Figure 3: Schematic representation of HFn labeling reaction

Table 1: HFn fluorescence labeling optimization. Summary of the different conditions tested.

Reaction	HFn:AF488 (molar ratio)	Protein concentration (mg mL^{-1})	Reaction conditions
1	1:2.5	2	2 h RT
2	1:6	2	2 h RT
3	1:30	2	30 min RT then o/n 4 °C
4	1:50	5	30 min RT then o/n 4 °C
5	1:100	2	30 min RT then o/n 4 °C

After incubation, the free dye was removed using a Zeba™ Dye and Biotin Removal Spin Column (Thermo Fisher Scientific, MA, USA) and refined using fast protein size-exclusion liquid chromatography (SEC-FPLC). At the end of the run, the degree of labeling (DOL) of the sample was determined to find the optimum

labeling condition. The DOL obtained for the different reactions are summarized in Table 2.

Table 2: Degree of labeling (DOL) obtained in the different reactions performed.

Reaction	HFn:AF488 (molar ratio)	Protein concentration (mg mL^{-1})	Reaction conditions	DOL
1	1:2.5	2	2 h RT	0.15
2	1:6	2	2 h RT	0.3
3	1:30	2	30 min RT then o/n 4 °C	1.5
4	1:50	5	30 min RT then o/n 4°C	3.9
5	1:100	2	30 min RT then o/n 4 °C	4

According to the AlexaFluor488 manufacturer instructions, the acceptable degree of labeling ranges between 4 and 9. We obtained a DOL of 4 in reactions 4 and 5 and, for future labeling we decided to maintain the reaction condition of reaction number 4 because we obtained almost the same DOL as reaction 5 but using half of the fluorophore. The difference in the DOL obtained in reactions 4 and 5 was very low, despite the fact that the HFn/AF488 molar ratio was double in the second case. This result could be explained considering that saturation of the lysins available for binding to the surface of HFn occurs already using a molar ratio of 1:50. Therefore, even increasing the ratio between the fluorescent molecules and the HFn, the number of bounded molecules (DOL) could not increase. The kinetic and success of the reactions were highly concentration dependent. The higher concentration (5 mg mL^{-1}) proved to be the best condition probably because a higher protein concentration results in a

greater probability for the molecules of the two species to collide in the reaction solution and therefore to form the link. Likewise, the reaction is favored when the species are kept under stirring for a longer time.

CTX fluorescence labeling optimization

At the same time, we also optimized the labeling condition of CTX and AlexaFluor647. As for HFn we tested different protein concentrations in the reaction mix and different reaction conditions. In particular, tests were carried out with a molar ratio between HFn and AlexaFluor647 of 1:8.9, 1:10, 1:15 and 1:20. Protein concentration was set at 2 mg mL^{-1} or at 5 mg mL^{-1} and the reaction mix was maintained for 1 hour at room temperature with continuous stirring or for 2.5 hours at room temperature always with continuous stirring. All the reactions were performed using sodium bicarbonate buffer ($NaHCO_3$, 0,1 M, pH 9.0). In this case PEG was also added to the reaction mix because this linker competes with AlexaFluo647 for the binding to the amine groups of the CTX. We maintained a CTX:PEG molar ratio of 1:20. Table 3 summarizes the reaction conditions tested.



Figure 4: Schematic representation of CTX labeling reaction

Table 3**: HFn fluorescence labeling optimization.** Summary of the different conditions tested.

Reaction	CTX:AF647 (molar ratio)	Protein concentration (mg mL^{-1})	Reaction conditions	PEG presence?
1	1:8.9	2	1 h RT	yes
2	1:10	5	2.5 h RT	yes
3	1:15	5	2.5 h RT	yes
3a	1:15	5	2.5 h RT	no
4	1:20	2	1 h RT	yes

At the end of the incubation time, the free dye was removed using a Zeba™ Dye and Biotin Removal Spin Column (Thermo Fisher Scientific, MA, USA) and refined using fast protein size-exclusion liquid chromatography (SEC-FPLC). Then the degree of labeling (DOL) of the obtained sample was determined in order to find the optimum labeling condition. The DOL obtained for the different reaction are summarized in the following table (Table 4):

Table 4: Degree of labeling (DOL) obtained in the different reactions performed.

Reaction	Molar ratio CTX:AF647	Protein concentration (mg mL^{-1})	Reaction conditions	PEG presence?	DOL
1	1:8.9	2	1 h RT	yes	1.1
2	1:20	2	1 h RT	yes	2.1
3	1:10	5	2.5 h RT	yes	4.6
4	1:15	5	2.5 h RT	yes	7.9
4a	1:15	5	2.5 h RT	no	9.1

According to the AlexaFluor647 manufacturer guidelines, the acceptable degree of labeling varies between 3 and 7. The conditions to obtain the recommended DOL are those of reaction 2. Also, in the case of CTX a higher concentration of proteins corresponds to a higher number of AlexaFluor647 molecules bonded. Considering reactions 3 and 3a, it can be seen how the presence of PEG causes a decrease in DOL, suggesting an effective competition between the two molecules for the amino residues of the protein. In this case, the DOL obtained exceeded the one recommended. Although conjugates with a high number of attached dye molecules could be acceptable for use, over-labeling could cause aggregation of the protein conjugate and also reduce the antibody's specificity for its antigen, both of which might lead to nonspecific staining.

In vitro experiments

Evaluation of ADCC induced by HFn-CTX treatment by live imaging fluorescence microscopy

mAbs can elicit anticancer activity through two different mechanisms, namely direct or indirect. The direct effect is mediated just by the physical interaction between the mAb and its specific receptor, while the indirect one is the antibody-dependent cell-mediated cytotoxicity (ADCC) and requires the recruitment of immune effector cells to be activated. The importance of the interaction between the Fc portion of mAbs and its receptor (FcγR, CD16) has been investigated in several studies so that now it is considered to be crucial for the *in vivo* antitumor effects of certain monoclonal antibodies.[46] However, it is known that not all monoclonal antibodies are able to elicit the same immune response, due to differences in their affinity for CD16.[47] For CTX there are evidence that ADCC activation contributes to its overall anticancer

activity.[24,26,48] To evaluate the amount of ADCC response induced by HFn-CTX treatment on cancer cells, we incubated 3D cancer spheroids with freshly isolated PBMCs, containing around 5 to 15% of NK cells, at an effector-to-target cell (E:T) ratio of 2:1 and we performed a live image fluorescence microscopy analysis. Before running the experiment, PBMCs were incubated 24 h with IL-2 to allow their activation. Spheroids of U-87 MG and MDA-MB-231 were pre-incubated with 10 μg mL^{-1} of CTX and HFn-CTX at 4 °C for 30 minutes, before the addition of activated PBMCs. These live imaging experiments were conducted using a fluorescence microscope named Operetta CLS High content analysis system, recording frames every hour for up to 50 hours to monitor the ADCC activation. In order to visualize tumors and effectors cells, 3D cancer spheroids were stained with Höechst before adding 4 spheroids to each well of a 96 wells plate. At the same time, IL-2 activated effectors cells were stained with CellTracker™ Deep Red Dye before adding them to the spheroids-containing wells. In the images below spheroids appear as a blue mass while PBMCs appeared as red spots smaller in size compared to cancer cells. In order to investigate the effect of the ADCC activation we added the CellEvent™ Caspase-3/7 Green Detection reagent to visualize apoptosis as a green signal.

At the beginning of the experiments, as shown in the figure below (Fig5) for the U-87 MG, the green signal can be barely seen meaning that both the effectors and cancer cells are alive. Moreover, the PBMCs appear widespread in all the tested wells.

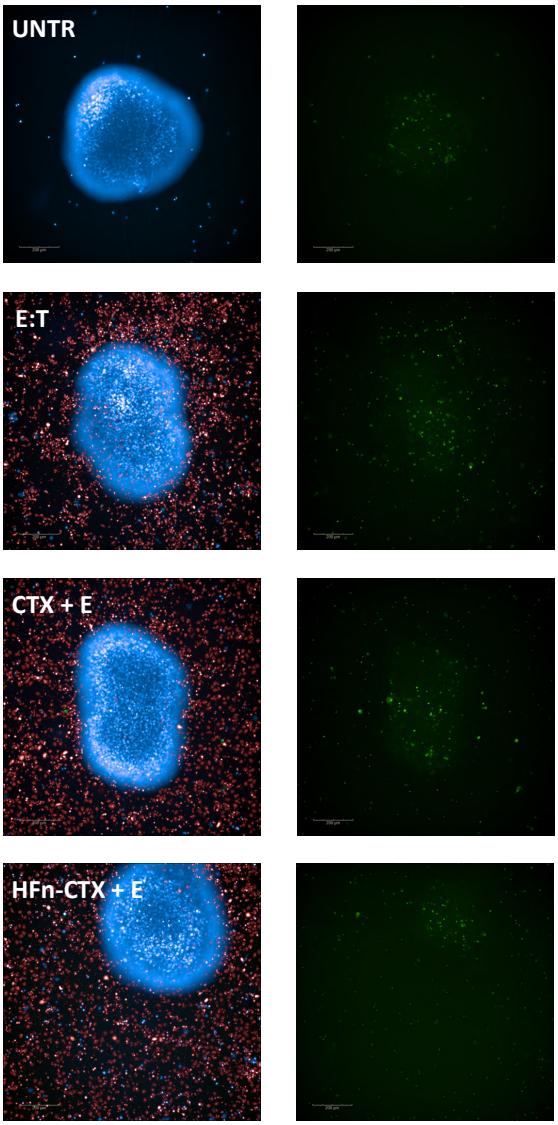

Figure 5: Live imaging ADCC experiment (beginning of the incubation). U-87 MG cancer spheroids were stained with Höechst (blue signal) before incubating them for 30 minutes at 4 °C with 10 µg mL^{-1} of CTX or HFn-CTX. CellTracker™ Deep Red pre-stained effectors were added to the wells and images were acquired every 1 hour for 52 hours. During this period of time, we evaluated the apoptosis with the CellEvent™ Caspase-3/7 Green Detection reagent (green signal). These images are representative

of 3 treated spheroids for each condition. E = effectors cells; T = target cancer cells. Scale bar = 200 µm.

The green fluorescence signal is significantly higher after 50 hours from the beginning of the experiments, meaning that a higher number of cells underwent programmed cell death, especially inside the spheroids. Comparing the different treatments, we saw that the green signal is higher in the presence of monoclonal antibodies compared to controls, both unconjugated and conjugated to ferritin. Furthermore, in the wells where the spheroids were treated with CTX and HFn-CTX we noticed that effector cells accumulate near the surface of the spheroid and probably invade the tumor mass. This accumulation occurs to a lesser extent in the absence of the treatments. In particular, the migration of the ADCC-performing effectors is more visible and conspicuous in the well where the spheroids are treated with the HFn-CTX nanoconjugate (Fig6).

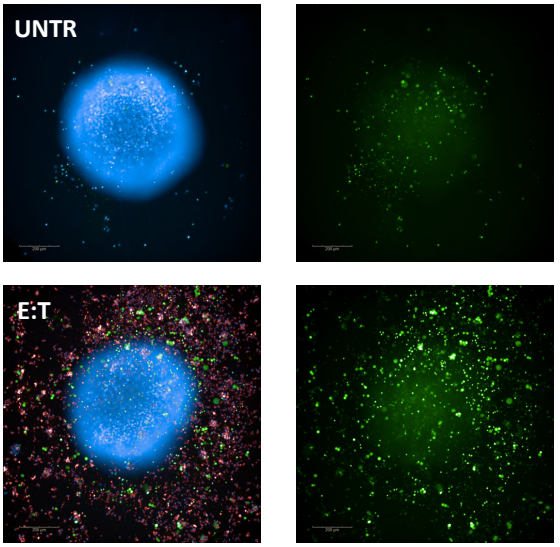

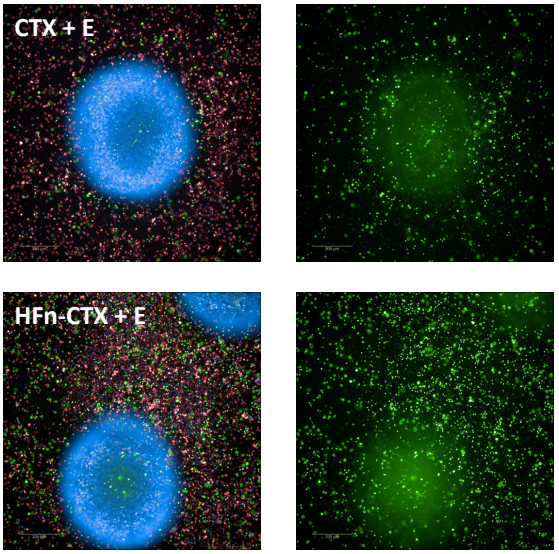

Figure 6: Live imaging ADCC experiment (52 hours of incubation). U-87 MG cancer spheroids were stained with Höechst (blue signal) before incubating them for 30 minutes at 4 °C with 10 µg mL^{-1} of CTX or HFn-CTX. CellTracker™ Deep Red pre-stained effectors were added to the wells and images were acquired every 1 hour for 52 hours. During this period of time, we evaluated the apoptosis with the CellEvent™ Caspase-3/7 Green Detection reagent (green signal). These images are representative of 3 treated spheroids for each condition. E = effectors cells; T = target cancer cells. Scale bar = 200 µm.

Exploiting the Harmony software applied to the microscope we decided to quantify the green fluorescence intensity related to the caspase activity inside the treated and untreated spheroids. The caspase production increases over time in all the spheroids analyzed but, in particular, in the presence of IL-2 activated effectors and after 50 hours of incubation with CTX and HFn-CTX. Moreover, the conjugated CTX seems to promote caspase production slightly more than CTX alone (Fig7).

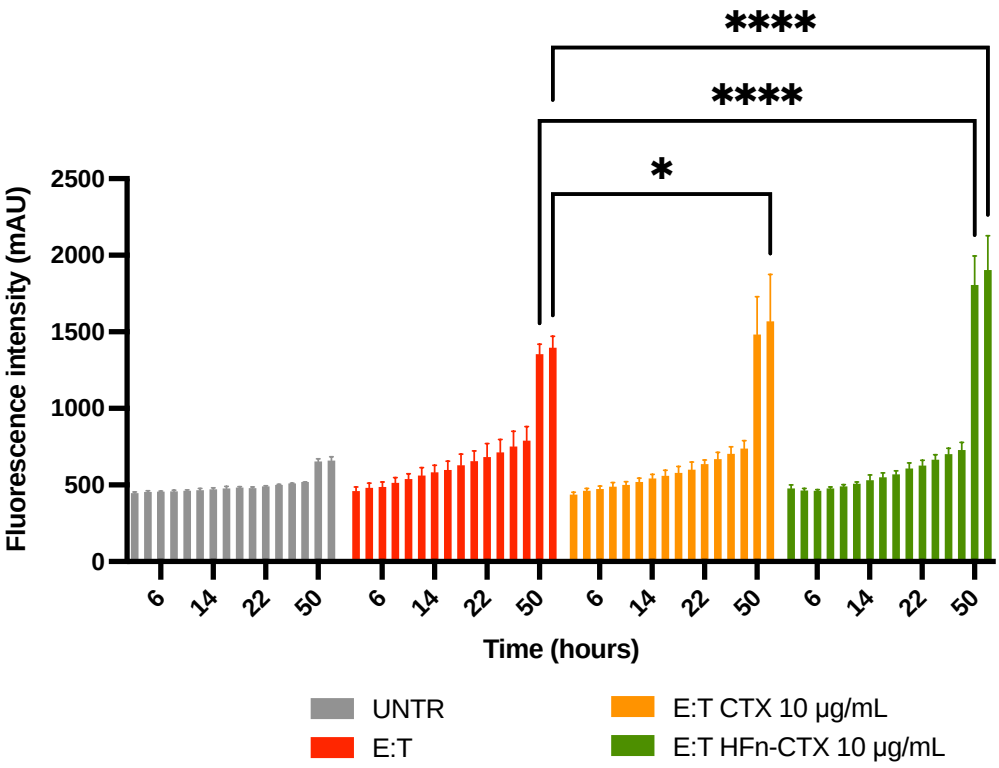

Figure 7: Caspase activation inside spheroids. Fluorescence intensity quantification revealed that especially after 50 h of incubation with effectors, CTX and HFn-CTX were able to determine the apoptosis of cancer cells. Reported values are means of 3 spheroids ± s.d. Statistical significance of treatments *vs.* non-treated cells (E:T), * = $p < 0.05$, **** = $p < 0.0001$. (2way ANOVA).

As for the U-87 MG, also for the MDA-MB-231 at the beginning of the experiments (Fig8), the green signal can be barely seen meaning that both the effectors and cancer cells are alive. Moreover, the PBMCs appear widespread in all the tested wells.

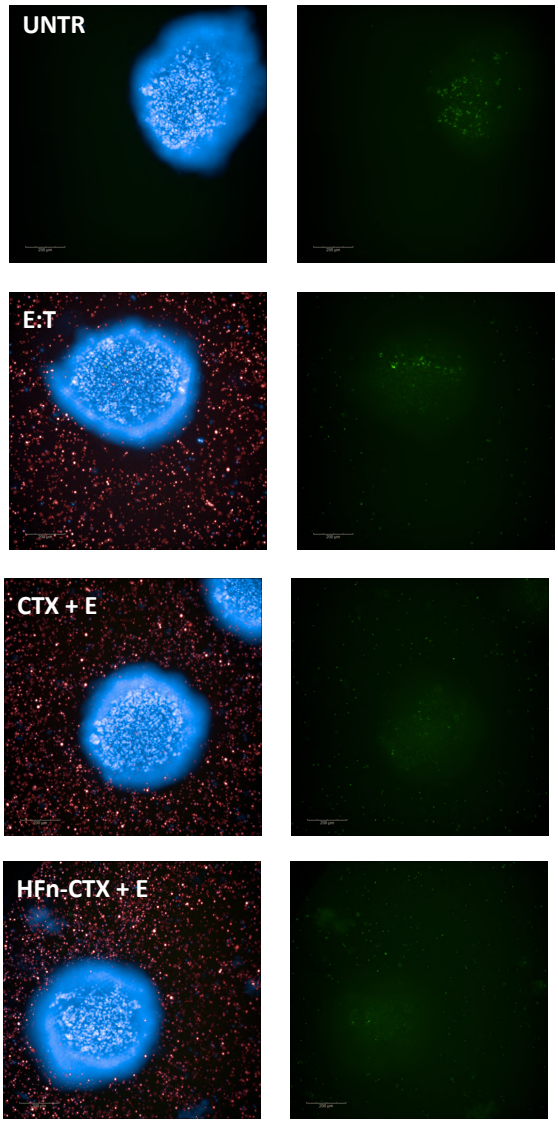

Figure 8: Live imaging ADCC experiment (beginning of the incubation). MDA-MB-231 cancer spheroids were stained with Höechst (blue signal) before incubating them for 30 minutes at 4 °C with 10 µg mL^{-1} of CTX or HFn-CTX. CellTracker™ Deep Red pre-stained effectors were added to the wells and images were acquired every 1 hour for 51 hours. During this period of time, we evaluated the apoptosis with the CellEvent™ Caspase-3/7 Green Detection reagent (green signal). These images are representative

of 3 treated spheroids for each condition. E = effectors cells; T = target cancer cells. Scale bar = 200 µm.

Both the caspase 3/7 green signal and the number of effectors cells around spheroids greatly increase over time especially in the presence of HFn-CTX. Moreover, after 51 hours of incubation the green signal is higher in the spheroids treated with HFn-CTX (Fig9).

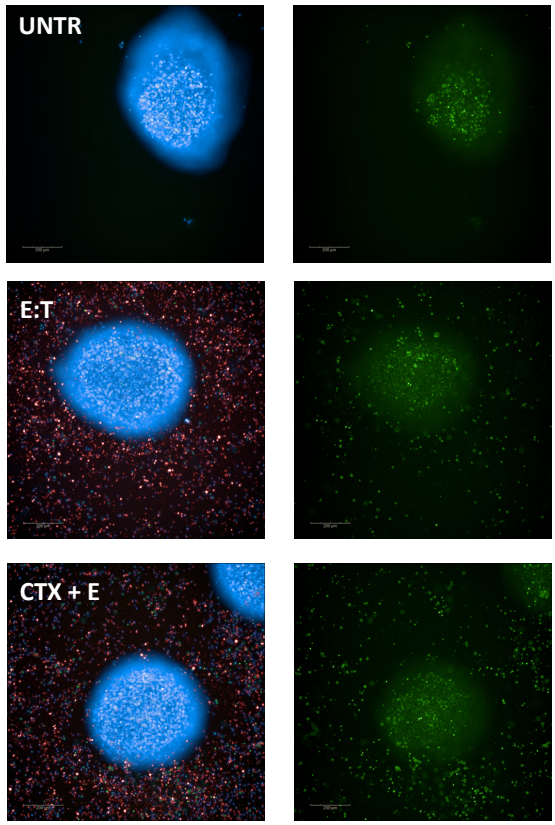

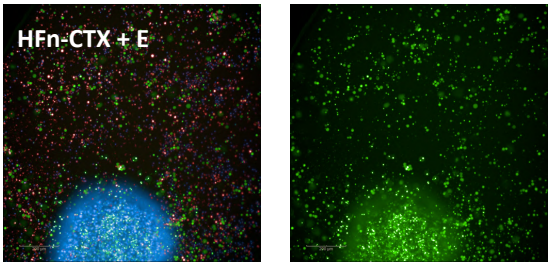

Figure 9: Live imaging ADCC experiment (51 hours of incubation). MDA-MB-231 cancer spheroids were stained with Höechst (blue signal) before incubating them for 30 minutes at 4 °C with 10 µg mL^{-1} of CTX or HFn-CTX. CellTracker™ Deep Red pre-stained effectors were added to the wells and images were acquired every 1 hour for 51 hours. During this period of time, we evaluated the apoptosis with the CellEvent™ Caspase-3/7 Green Detection reagent (green signal). These images are representative of 3 treated spheroids for each condition. E = effectors cells; T = target cancer cells. Scale bar = 200 µm.

Once again, we quantified the green fluorescence intensity as a direct measure of the apoptosis of target cells inside the spheroids. Even with the MDA-MB-231 cell line the caspase production increases over time in all the spheroids analyzed but, in particular, in the presence of IL-2 activated effectors and after 50 hours of incubation with HFn-CTX. Surprisingly, CTX alone didn't almost show any sign of caspase 3/7 activation (Fig10). Considering that the PBMCs isolation, which has to be repeated for every experiment, leads to high variability in the obtained results, we are considering repeating these ADCC experiments using a commercial cell line that constitutively expresses the Fc gamma receptor. If these data will be verified the molecular mechanism behind this greater effect of nanoconjugated CTX will be evaluated. Moreover, this experiment quantifies the caspase 3-7 that can be produced also after the cell cycle blockade caused

by the direct effect of CTX. However, MDA-MB-231 mutations in KRAS and BRAF made this cell line resistant to CTX.[49] This led us to speculate that the CTX nanoconjugation could determine long-lasting sequestration of EGFR thus altering its recycling process and reverting the resistance mechanism as previously shown with other nanoparticles.[50] Hence, the higher apoptotic effect observed in the presence of HFn-CTX could be attributable both to the ADCC activation and to the direct action of CTX after the binding to the EGFR receptor.

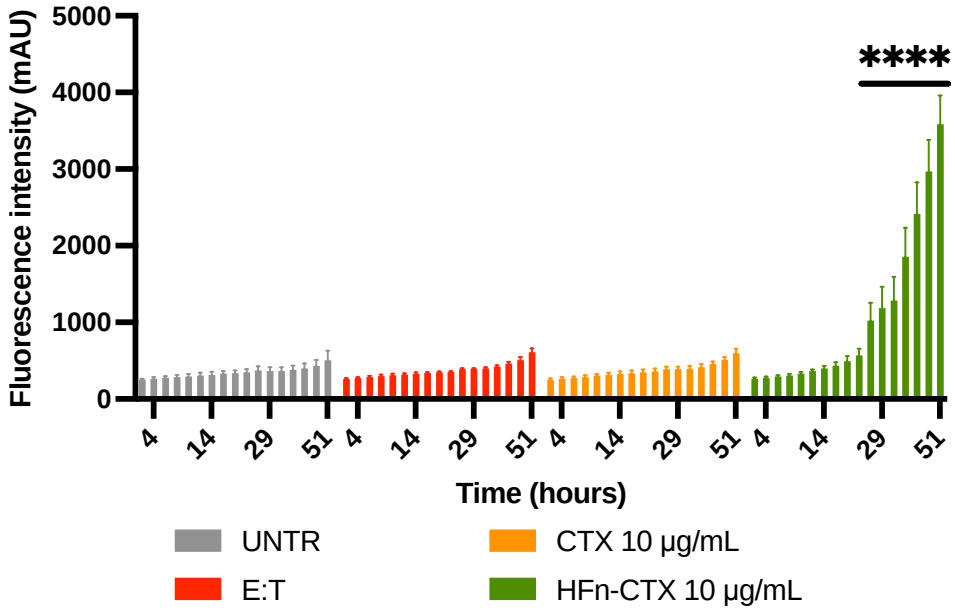

Figure 10: Caspase activation inside spheroids. Fluorescence intensity quantification revealed that especially after 48 h of incubation with effectors HFn-CTX was able to determine the apoptosis of cancer cells. Reported values are means of 3 spheroids ± s.d. Statistical significance of treatments *vs.* non-treated cells (E:T), **** = $p < 0.0001$. (2way ANOVA).

Quantitatively endpoint evaluation of ADCC induced by HFn-CTX

Considering that the quantitative analysis obtained from the images acquired with the Operetta system is somehow dependent on the labeling conditions of the spheroids, we decided to perform an endpoint ADCC assay to have another quantitative measure of the nanoformulation capability to activate the immune cells and promote apoptosis. To quantify the apoptosis, we used a commercial kit named The Caspase-Glo® 3/7 3D Assay (Promega) which correlates the caspase-3 and -7 activities present in apoptotic cells with the production of a luminescence signal. Upon activation, effector cells such as NK cells polarize and exocytose their granules in a calcium-dependent manner. Perforin and Granzyme B work in concert to induce cell death. Perforins create pores in the cell membrane that facilitate granzyme B entry into the target cell, resulting in DNA fragmentation and apoptosis.[23] In particular, after the delivery mediated by Perforin, Granzyme B acts as a serine protease causing the cleavage of procaspase 8/10 which then led to the activation of caspase 3/7 and to apoptosis.[51] Adding the reagent given by the kit results in cell lysis followed by caspase release, cleavage of the substrate and generation of a luminescent signal, produced by luciferase. Luminescence is proportional to the amount of caspase activity present. To evaluate the amount of caspase produced by the treated spheroids we incubated single spheroids with freshly isolated PBMCs at an effector-to-target cells (E:T) ratio of 2:1. Before running the experiment, PBMCs were incubated 24 h with IL-2 to allow their activation. Spheroids of U-87 MG and MDA-MB-231 were pre-incubated with 10 μg mL^{-1} of CTX or HFn-CTX and with 34 μg mL^{-1} of HFn at 4 °C for 30 minutes, before the addition of activated PBMCs. After 24, 30 and 48 hours of incubation spheroids were lysed, and the caspase amount was quantified according to the kit protocol. Observing

the luminescence intensity that directly correlates with spheroids apoptosis at different incubation times, for the glioblastoma cell line we obtained that caspase production increases over time in all the spheroids tested, both treated and untreated with conjugated and unconjugated CTX. Considering spheroids treated with CTX and HFn-CTX nanoconjugate, it can be observed that, at each incubation time, there is a greater production of caspase in the case of the spheroids treated with the nanoconjugate. This result confirms the one that was obtained with fluorescence microscopy: the conjugation of CTX to HFn seems to improve its ability to activate ADCC in the presence of pre-activated innate immunity cells and 3D cultures of glioblastoma. Similar behavior was also observed for breast cancer spheroids. MDA-MB-231 cells treated with HFn-CTX showed a higher caspase activation than those treated with unconjugated CTX, thus confirming the quantification obtained after the live imaging experiment. For both cell lines, the monoclonal antibody Trastuzumab (Tz) and HFn alone were used as negative controls. Regarding HFn, spheroids were treated with 34 $\mu g\ mL^{-1}$ of nanoparticle because 10 $\mu g\ mL^{-1}$ of CTX in the nanoconjugate formulation correspond to 34 $\mu g\ mL^{-1}$ of HFn considering that the two protein species have a molar ratio of 1:1 (Fig.11).

A)

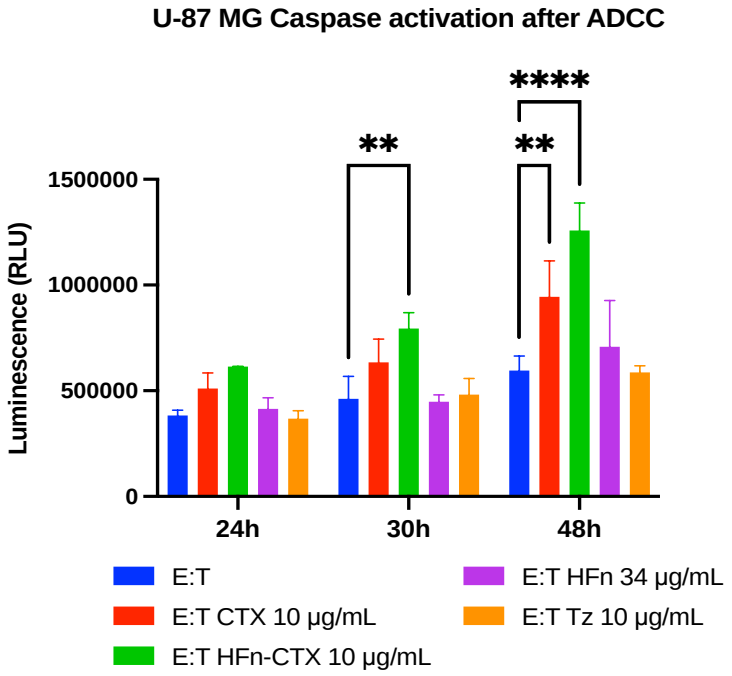

B)

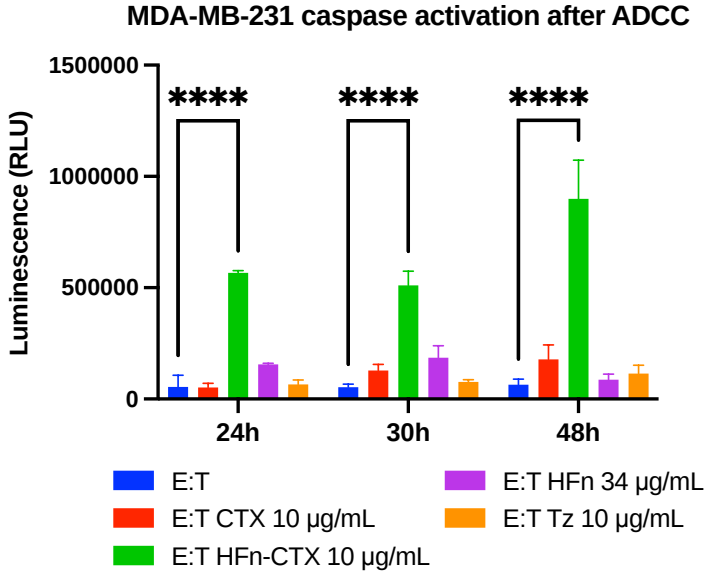

Figure 11: Caspase production after ADCC activation. U-87 MG (A) and MDA-MB-231 (B) spheroids were pre-coated with 10 µg mL^{-1} of CTX, HFn-CTX or Tz or with 34 µg mL^{-}

[1] of HFn at 4 °C for 30 min. Next, IL-2-activated PBMCs were added to the target cells with a E:T ratio of 2:1 and incubated for 24, 30 and 48 h at 37 °C. Graphs represent the mean luminescence intensity ± s.d. (n=3). Statistical significance of treatments *vs.* non-treated cells (E:T), ** = $p < 0.005$; **** = $p < 0.0001$ (2way ANOVA).

Shedding of CD16 receptor

Effector cells that mediate ADCC include natural killer (NK) cells, monocytes, macrophages, neutrophils, eosinophils and dendritic cells.[52] Even if NK cells represent only the 5-15% of circulating lymphocytes in humans they are considered the main ADCC effectors even if, unless appropriately activated, naïve NK cells exhibit limited cytotoxicity.[53] Indeed, NK cells express many receptors that can activate or inhibit their cytotoxic and secretory functions. Even if CD16 is one of the most potent activating receptors on this type of cells, it undergoes a rapid downregulation in expression by a proteolytic process following NK cell activation with various stimuli.[54,55] One of these processes involves the proteolytic cleavage of the CD16 receptor mediated by a metalloproteinase expressed on NK surface, ADAM17, which is activated upon the interaction of Fc with CD16. This inactivation process is also called CD16 shedding and represents one of the strongest limitations for NK-based therapies.[55]

In order to better investigate the cytotoxic effect induced by our nanoformulation we checked the amount of CD16 shedding. So, if with the ADCC assay we evaluated the effect of our treatment on target cells, now we can appreciate the effect of the same treatment on effector cells. A schematic representation of the CD16 shedding mechanism is reported in Figure 13: after the recruitment, NK cells bind to the Fc portion of mAbs through the CD16, which in turn promotes the ADCC and activates ADAM17 metalloproteinase,

leading to the cleavage of CD16 and the inhibition of the cytotoxic response. Briefly, U-87 and MDA-MB-231 spheroids were transferred in a 48-well plate and treated with CTX or HFn-CTX samples at the same concentrations used for the ADCC assay. After 30 minutes of coating, IL-2 activated PBMCs (E:T ratio of 2:1) were added and the co-cultures were incubated for 48h at 37 °C. Then the effectors-containing medium was collected and incubated with AF488 anti-human CD16 antibody before cytofluorimetric analysis. We observed that effectors previously incubated with glioblastoma and breast cancer cells induced a lower reduction of CD16 expression, compared to HFn-CTX treatment (Fig12). Our results showed that the nanoformulation tested was able to significantly reduce the amount of extracellular CD16 on effectors cells membrane, thus confirming that the result obtained in ADCC assays was indeed attributable to NK activation.

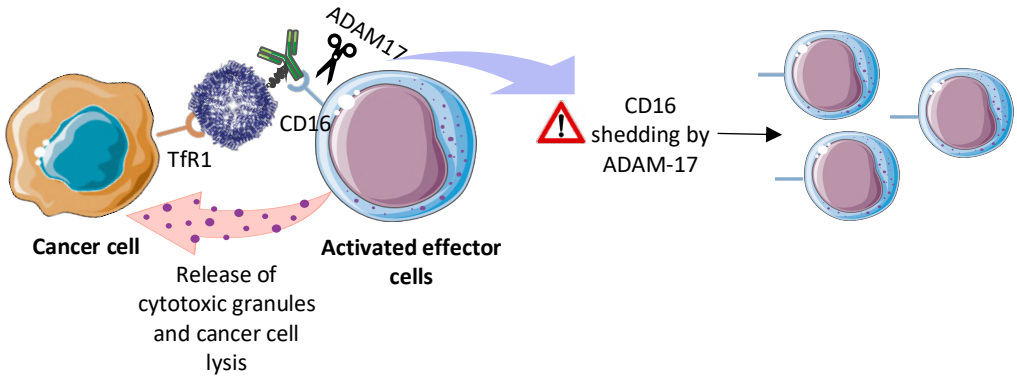

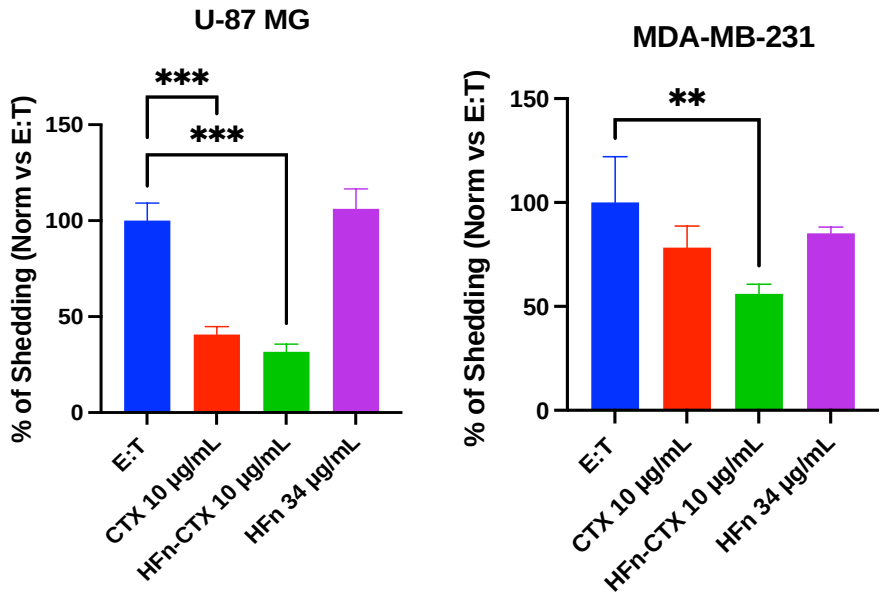

Figure 12: Evaluation of CD16 shedding. (Above) Schematic illustration of the process of ADCC inactivation, mediated by the cleavage of CD16. (Below) U-87 MG and MDA-MB-231 cells were treated with HFn-CTX, free CTX and HFn as previously described for ADCC assay. After incubation with PBMCs, the medium was collected and incubated with labeled anti-human CD16 antibody. Cytofluorimetric analysis revealed that the nanoformulation was able to significantly reduce CD16 expression on effector cells. E:T sample was used to set the positive region and the singlet gate. Reported values are means of 3 replicates ± s.d. ** = $p < 0.01$; *** = $p < 0.0005$ (One-way ANOVA).

Uptake experiments

As a possible explanation of the different apoptotic effects observed in the ADCC experiments for CTX and HFn-CTX we hypothesized that they could have a different penetration inside spheroids. We first analyze CTX and HFn-CTX penetration by confocal live imaging microscopy to validate this hypothesis. U-87 MG spheroids were labeled with Höechst while free and conjugated CTX were labeled with fluorescein isothiocyanate (FITC) following the same protocol

described above for the labeling with Alexa fluorophores. After 3.5h of incubation with 10 μg mL^{-1} of CTX or HFn-CTX, confocal images of the spheroids at different optical sections were acquired. However, considering that the spheroids' diameter is 600/700 μm, the confocal laser can't reach their core (Fig13) thus making it difficult to quantitatively study nanoparticles penetration.

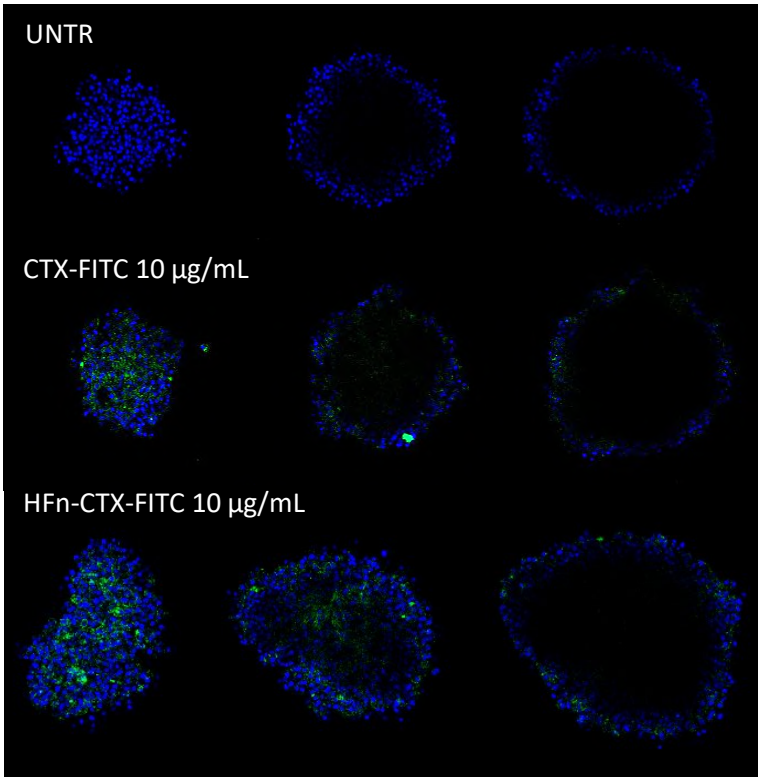

Figure 13: Confocal images of U-87 MG spheroids representing different optical sections acquired for each treatment. Spheroids were incubated with medium only (UNTR) or with medium containing 10 μg mL^{-1} of CTX-FITC or HFn-CTX-FITC (green signal). Images were acquired after 3.5h from the beginning of the incubation.

As a possible solution, spheroids could be fixed and cut but, considering that it is tedious to cut histological sections to derive data from the whole spheroid

routinely and that confocal microscopy imaging of spheroids suffers from an increasing quenching of fluorescence with increasing depth from spheroid surface, we decided to use the cytofluorimeter to check the ability of our nanoconjugate to bind and enter the spheroid in a specific way.

For these experiments, twelve spheroids were incubated with CTX-AF647, HFn-AF488 or double-labeled HFn-AF488-CTX-AF647 for 3h and 30 minutes at 37 °C. At the end of the incubation, spheroids were trypsinized to obtain a single cells suspension and analyzed by flow cytometry. Considering CTX-AF647 fluorescence (Fig14), after 3.5h of incubation CTX and HFn-CTX are taken up by ~99% of U-87 MG cancer cells. This experiment demonstrates that free and conjugated CTX are capable to penetrate through the spheroids in the same way at the incubation time tested. Moving to the HFn-AF488 fluorescence, HFn is taken up by ~60% of U-87 MG cancer cells while HFn-CTX is taken up by ~70% of cells. It must be noted that the percentage of HFn-positive cells could be underestimated by the used gate settings. Indeed, the AF488 fluorescence distribution of HFn-treated cells is a unimodal distribution that is shifted toward higher fluorescence values compared to AF488 fluorescence distribution of untreated cells but partially overlapped with this one. For this reason, the HFn-AF488-positivity gate set could not include all the cells that have taken up HFn/HFn-CTX. This could explain the apparently contradictory HFn-CTX nanoconjugate-related data. As a matter of fact, U-87 MG cancer cells seem to be ~99% positive or ~70% positive for nanoconjugate uptake if CTX-AF647 fluorescence or HFn-AF488 fluorescence is considered, respectively. However, by shifting the attention from the percentage of HFn/CTX-positive cells to the AF488 and AF647 fluorescence values, we can speculate that CTX and HFn are effectively conjugated and the uptake of nanoconjugate-associated HFn-AF488

is underestimated. We obtained the same results also with MDA-MB-231 spheroids (FigS1) which led us to conclude that there is no difference in terms of spheroids penetration between free and conjugated CTX at the selected time point (Fig14 B).

A)

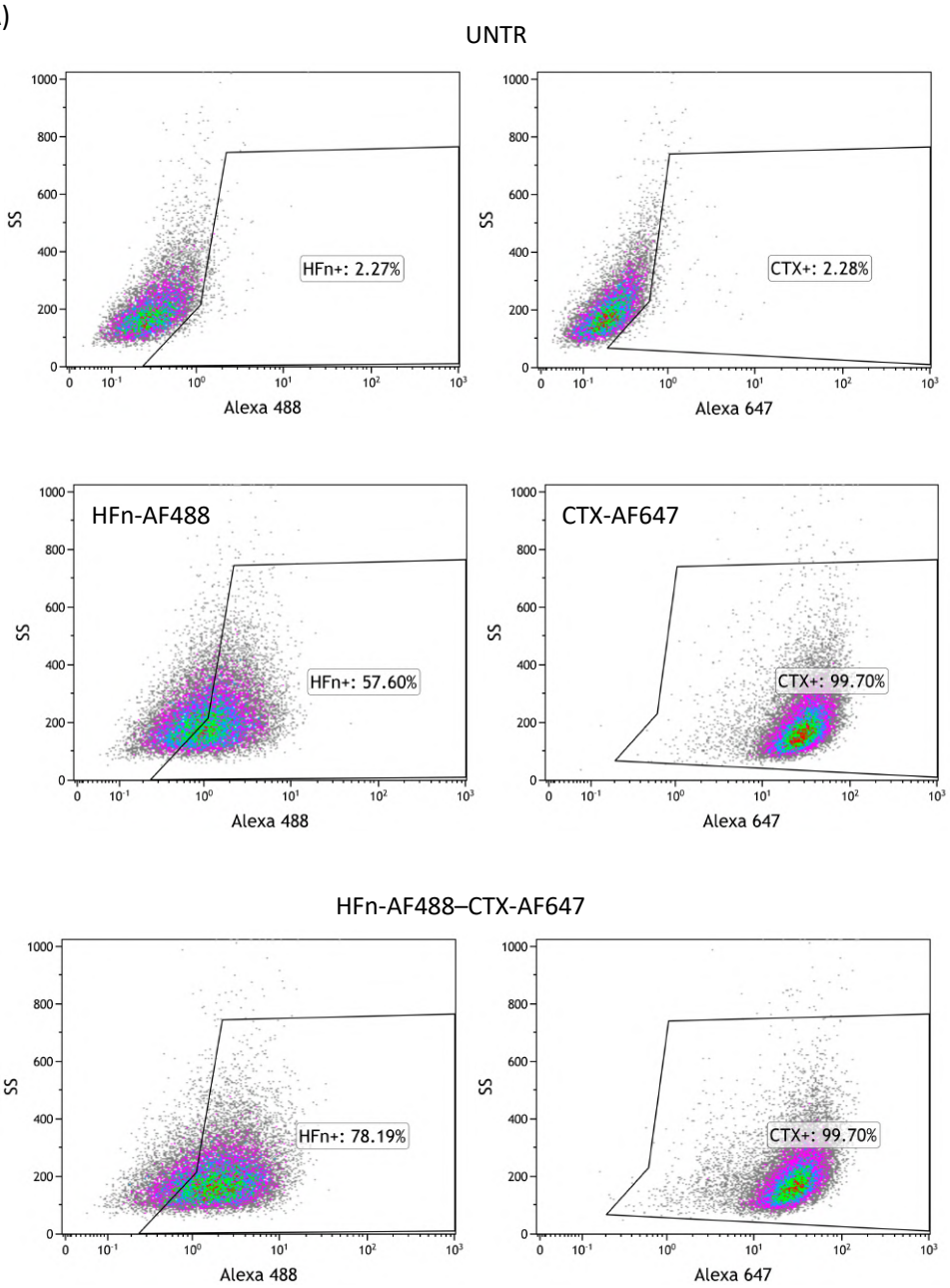

B)

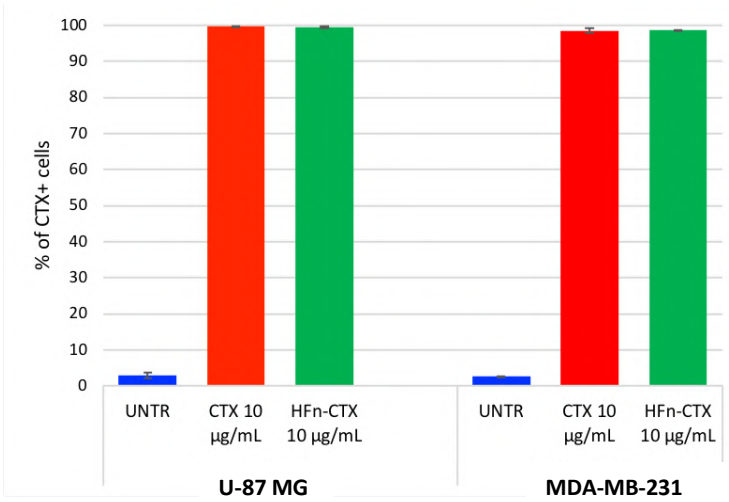

Figure 14: Cytofluorimetric uptake experiment. A) Representative population density plot of U-87 MG spheroids. The gates were set starting from untreated cells to show positive and negative fluorescence-stained cells. Each figure is representative of 3 replicates. Spheroids were incubated with 10 µg mL^{-1} of CTX-AF647, HFn-AF488-CTX-AF647 or with 34 µg mL^{-1} of HFn-AF488 for 3.5 hours at 37 °C. At the end of incubation, spheroids were trypsinized to obtain a single cells suspension before performing a cytofluorimetric analysis. B) % of CTX-647 positive cells for U-87 MG and MDA-MB-231 cell lines. Reported values are means of 3 replicates ± s.d.

In order to validate these data, we performed others uptake experiments incubating spheroids with single labeled HFn-CTX-FITC or CTX-FITC. Considering that FITC and Alexa 488 have the same fluorescence spectrum and consequently undergo the same underestimation against untreated cells described above, after 3.5 h of incubation we obtained a % of CTX positive cells for HFn-CTX-FITC that is closer to the one obtained looking at the Alexa488 fluorescence observed for HFn-488-CTX-647 for both cell lines. Again, we didn't observe any differences

in terms of spheroids penetration between free and conjugated CTX at the selected time point (FigS2).

Preliminary *in vivo* experiment

In order to evaluate the biodistribution of our nanoconjugate *in vivo*, luciferase-transfected MDA-MB-231 (MDA-MB-231-L) breast cancer cells were subcutaneously inoculated into female NOD/scid common gamma chain-deficient mice (NSG mice). The reliability of the model was confirmed by following tumor progression by bioluminescence intensity (BLI) monitored by IVIS imaging over 20 days after intraperitoneal injection of luciferin (Ln) (Fig.15).

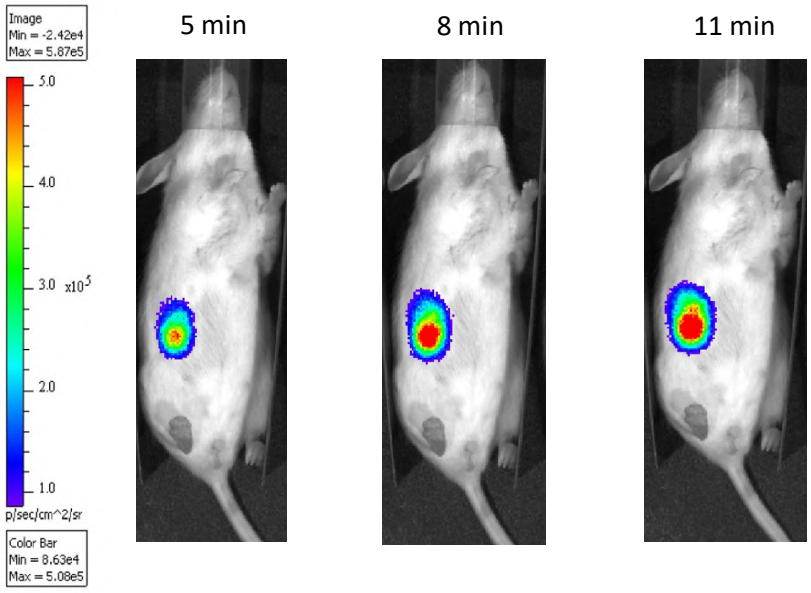

Figure 15: Tumor growth of MDA-MB-231-L breast cancer model. NSG female mice were injected into the mammary fat pad with $3x10^6$ cells/mouse. Bioluminescence intensity emitted upon intraperitoneal injection of luciferin was acquired 28 days after tumor implantation. The luciferin bioluminescent signal was higher after 11 minutes from the luciferin injection.

After four weeks, the tumors reached 0.16 cm^2 size and mice were injected into the tail vein with the doubled labeled nanoconjugate HFn-Alexa488-CTX-Alexa647 (HFn-AF488-CTX-AF647) at 5 mg kg^{-1} and monitored by live fluorescence imaging at 3 h post injection. Monitoring the CTX-AF647 fluorescence, an intense epifluorescence signal (Epf) at the tumor was detected which displayed an efficient tumor uptake. Unfortunately, it was not possible to detect HFn-AF488 signal because of the high tissue autofluorescence at this wavelength of emission which could not be distinguished from the nanoconjugate signal. Epifluorescence of excised tumors 3 h after HFn-AF488-CTX-AF647 injection confirmed the accumulation of the nanoconjugate at the tumor site (Figure 16).

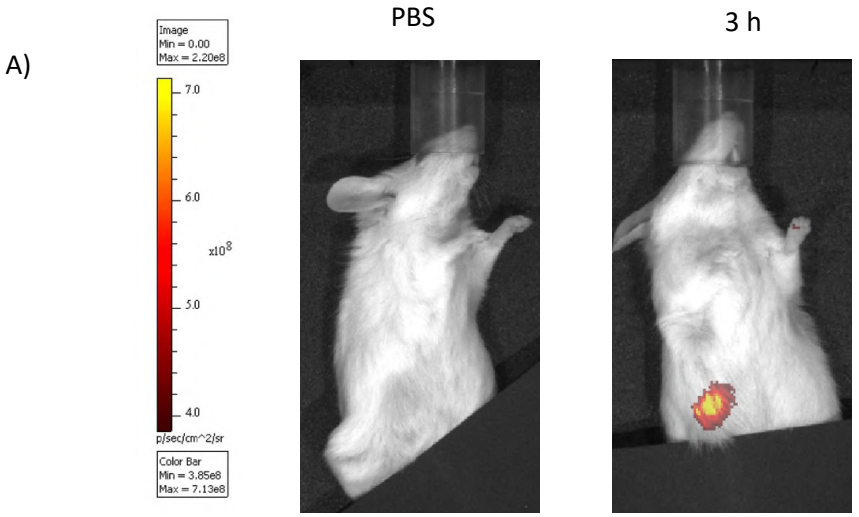

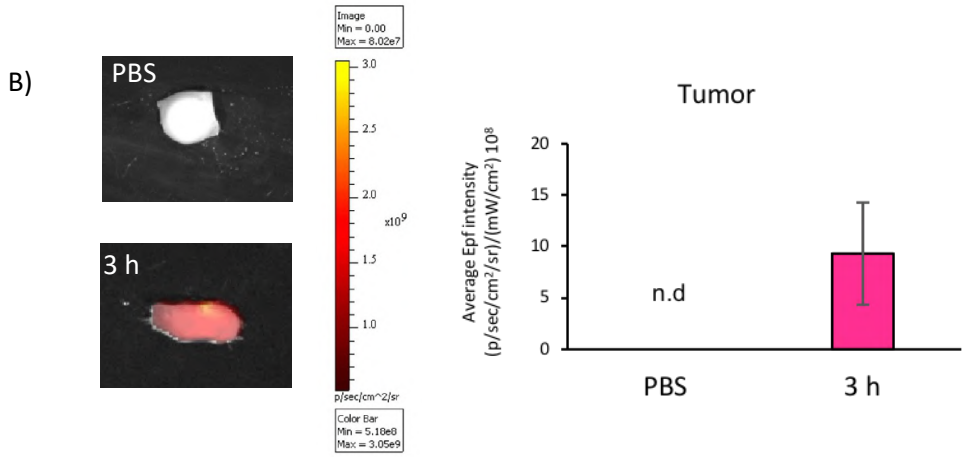

Figure 16: *In vivo* targeting and distribution of HFn-CTX. A) Epifluorescence (Epf) images of mice bearing MDA-MB-231-L tumors acquired 3 h after intravenous (i.v.) injection into the tail vein of 5 mg kg^{-1} HFn-AF488-CTX-AF647. B) Epf of isolated MDA-MB-231 tumors and averaged Epf intensity of tumor ROI acquired 3h after exposure to HFn-AF488-CTX-AF647. The color scale indicates the averaged epifluorescence expressed as radiant efficiency [(p/sec/cm^2/sr)/(mW/cm^2)], where p/sec/cm^2/sr is the number of photons per second that leave a square centimeter of tissue and radiate into a solid angle of one steradian (sr). Values reported are the mean of three mice ± s.e. PBS was administered as a control (n.d. = not detectable).

Moreover, non-target organs (liver, spleen, kidneys, lung and heart) dissected from mice were analyzed *ex vivo* and quantified by measuring the Epf intensity. The major accumulation of nanoparticles was observed in liver, in agreement with the detoxification role of this organ (Fig17).[56]

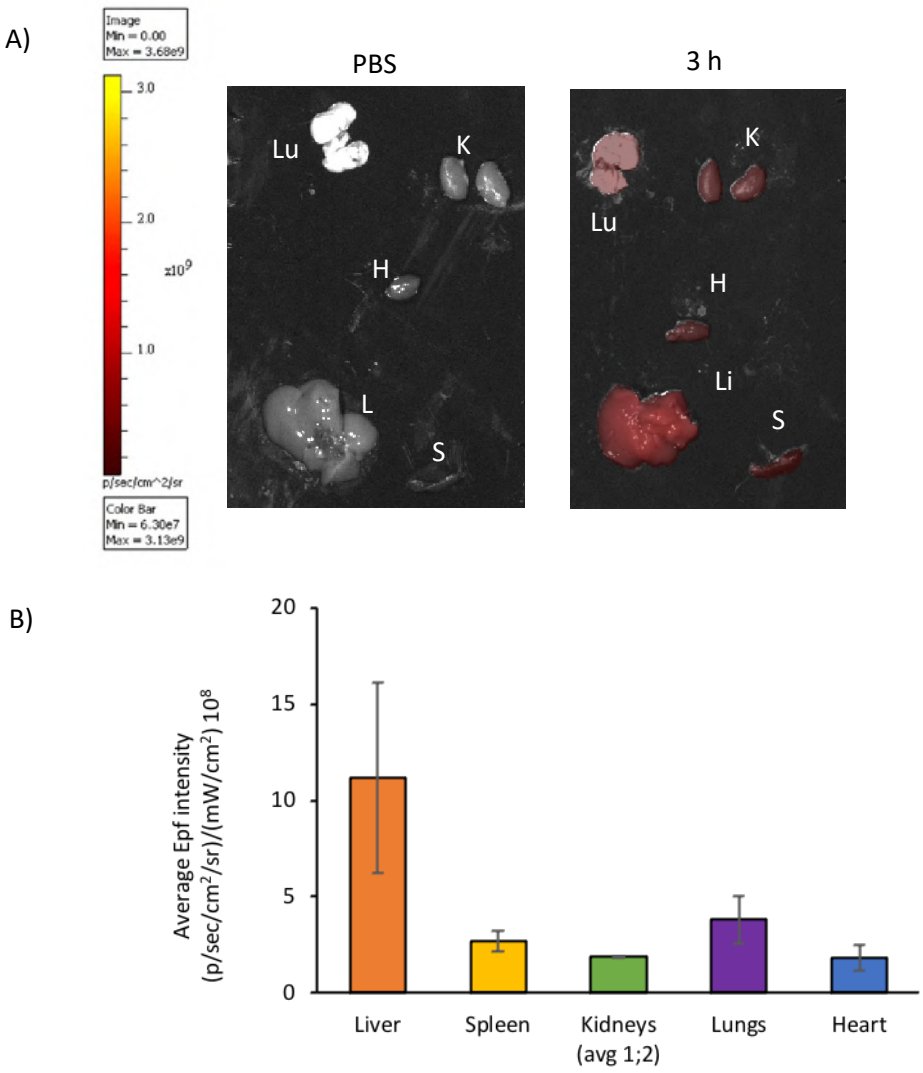

Figure 17: A) Epf of isolated spleen (S), kidneys (K), liver (L), brain (B), heart (H), lungs (Lu) after intravenous injection into the tail vein of PBS and 5 mg Kg^{-1} of HFn-AF488-CTX-AF647 respectively. The color scale indicates the averaged epifluorescence expressed as radiant efficiency [(p/sec/cm^2/sr)/ (mW/cm^2)], where p/sec/cm^2/sr is the number of photons per second that leave a square centimeter of tissue and radiate into a solid angle of one steradian (sr). B) Averaged Epf intensity of the ROI obtained *ex vivo* after exposure to HFn-AF488-CTX-AF647. Values reported are the mean of three mice ± s.e., normalized subtracting Epf values of PBS administered as control.

This *in vivo* preliminary experiment showed that HFn-CTX nanoconjugate correctly accumulate at the tumor site. Further experiments will be conducted to confirm this result, replacing AF488 with another more detectable fluorophore in order to monitor the signal of both proteins in the nanoconjugate. Moreover, in the next months, the *in vivo* antitumor efficacy of HFn-CTX will be evaluated by intravenously injecting NK cells isolated from buffy coats into tumor-burdened mice.

5. Discussion

In this study, we first produced a recombinant form of human apoferritin in a modified E.Coli strain, which allowed us not only to considerably reduce the level of detected endotoxin in the final HFn preparation, but also to probably obtain a residual level of endotoxin which is not able to activate human immune system cells. After synthesis, purification and characterization, the external surface of H-chain apoferritin was monofunctionalized with CTX. The choice of having only one monoclonal antibody immobilized on HFn surface was made to preserve the specificity of both proteins for their targets. Indeed, the interaction between the Fc portion of the monoclonal antibody and its receptor should be well-maintained to promote the ADCC activation and exert cytotoxic activity, as well as HFn-TfR1 interaction, which determines both the tumor cells recognition and the BBB crossing of the nanoconjugate as previously demonstrated.[38] Since HFn-CTX has shown the ability to cross BBB while maintaining its anticancer activity in 2D tumor models, we focused on studying its effect and interaction with 3D tumor models. For this study, we first developed 3D cancer spheroids made by a glioblastoma cell line (U-87 MG) and a triple-negative breast cancer cell line (MDA-MB-231). For both cell lines we obtained spheroids with a reproducible size and shape, adding for breast cancer cells an external structural scaffold to promote cellular aggregation. To evaluate the uptake of HFn-CTX nanoconjugate both *in vitro* and *in vivo* we optimized a labeling protocol to stain HFn and CTX with two fluorophores thus obtaining a double-labeled nanonconjugate. The uptake experiments revealed that, for both cell lines, there is no difference in the uptake penetration between CTX and HFn-CTX: both protein species, after 3 hours and 30 minutes, manage to reach almost all the

cells that form the spheroids. Next, we moved to the evaluation of HFn-CTX apoptotic effect. A well-known mechanism of action of monoclonal antibodies is the cytotoxicity mediated by immune cells. Even though ADCC is not induced by all monoclonal antibodies, for CTX there are lots of evidences. Thus, we checked if this mechanism was preserved both for CTX and HFn-CTX in presence of cancer spheroids. We performed a live imaging ADCC and an endpoint experiment, which were united by the caspase 3/7 production visualization and quantification as a direct measure of cell apoptosis. Our results showed that, in presence of U-87 MG spheroids, HFn-CTX and CTX were able to promote apoptosis in a similar way. With MDA-MB-231 HFn-CTX apoptotic effect not only was maintained but was also higher than the one obtained with CTX, which on the contrary didn't show any effects. The CTX ineffectiveness will be further verified and other analyses will be performed to distinguish between the direct and indirect apoptotic effect of CTX. At the moment, considering the intrinsic CTX resistance of MDA-MB-231, we can only speculate that the greater apoptotic effect of HFn-CTX can be due to the nanoconjugate potential to revert CTX resistance thus determining apoptosis both by cell cycle blockade and by effectors cells activation. The activation of the ADCC performing effectors was also confirmed by the evaluation of CD16 shedding, in which HFn-CTX showed its ability to reduce the percentage of CD16 positive cells, meaning that the effectors cells were previously activated by the treatment.

To conclude, we also performed a preliminary *in vivo* experiment to evaluate the biodistribution of HFn-CTX. After the establishment of an *in vivo* model of triple negative breast cancer, the injection of double-labeled HFn-CTX was followed by a preferential accumulation of the nanoconjugate at the tumor site. These preliminary data show that HFn-CTX nanoconjugate maintains the ability

to promote cancer cell apoptosis also in a 3D tumor model thus representing a promising approach for brain and breast cancer treatment. The next steps of this project will involve immunological *in vivo* experiments that will be performed to determine the cytotoxic activity of HFn-CTX in tumor-burden mice injected with human NK cells.

6. Supporting information

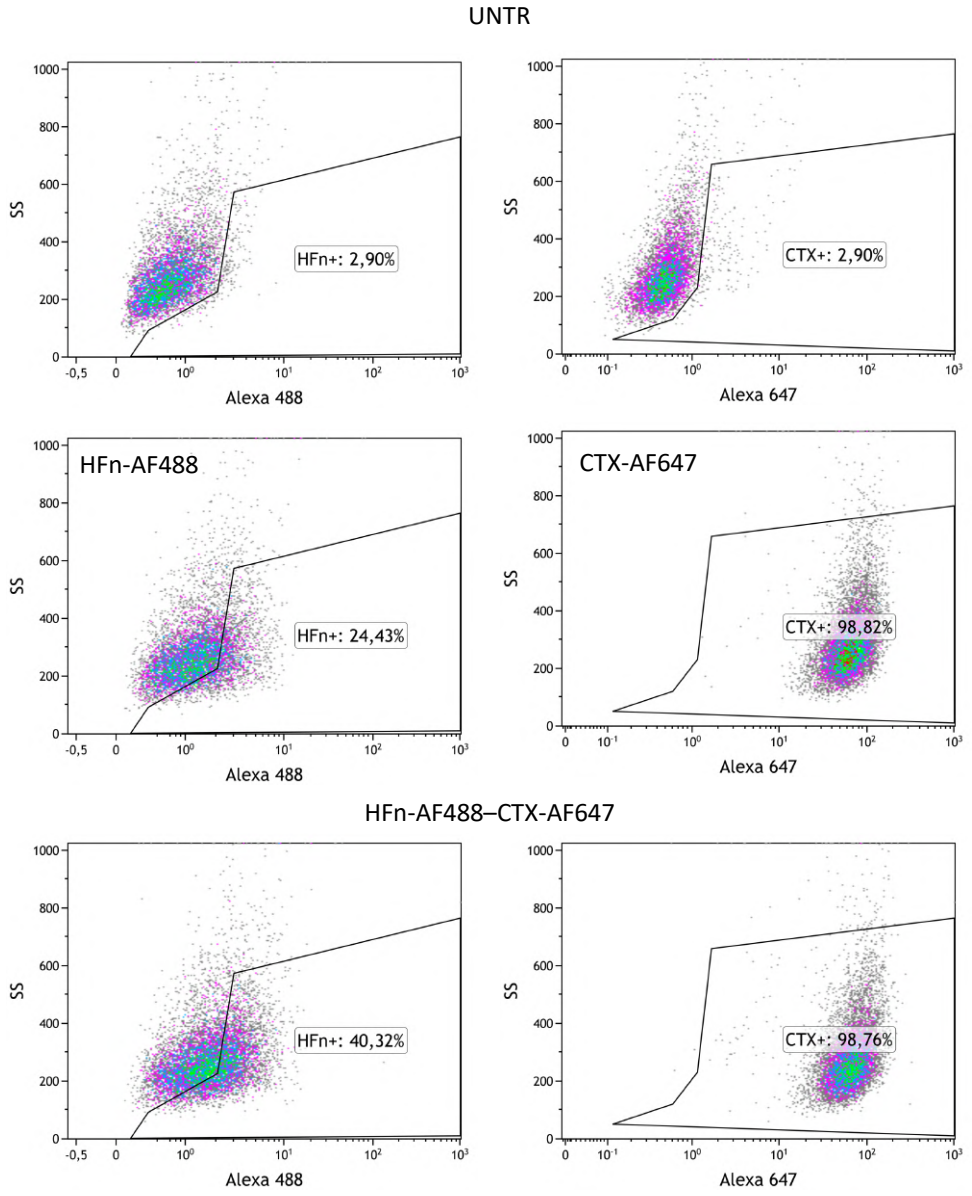

Figure S1: Representative population density plot of MDA-MB-231 spheroids. The gates were set starting from untreated cells to show positive and negative fluorescence-stained cells. Each figure is representative of 3 replicates. Spheroids were

incubated with 10 µg mL^{-1} of CTX-AF647, HFn-AF488-CTX-AF647 or with 34 µg mL^{-1} of HFn-AF488 for 3.5 hours at 37 °C. At the end of incubation, spheroids were trypsinized to obtain a single cells suspension before performing a cytofluorimetric analysis.

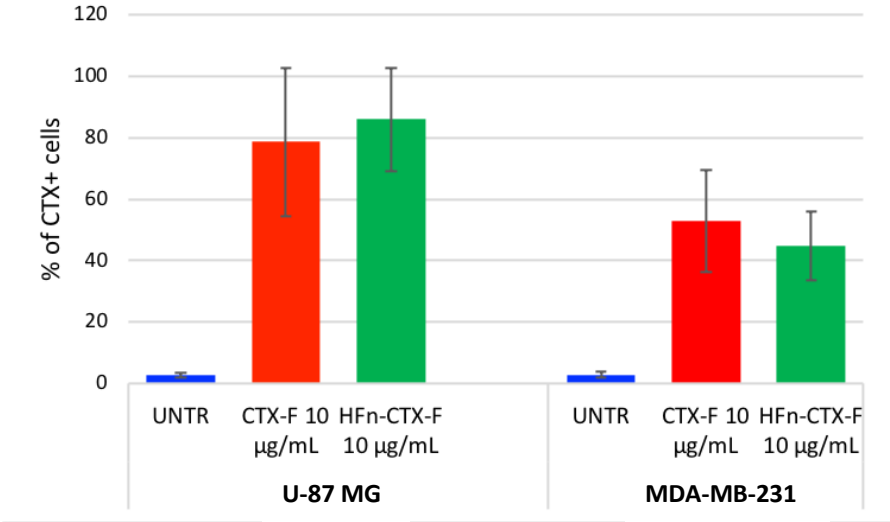

Figure S2: Uptake experiment with CTX-FITC and HFn-CTX-FITC on U-87 MG and MDA-MB-231 spheroids. Spheroids were incubated with 10 µg mL^{-1} of CTX-FITC or HFn-CTX-FITC for 3.5 hours at 37 °C. At the end of incubation, spheroids were trypsinized to obtain a single cells suspension before performing a cytofluorimetric analysis. The graphics show the % of CTX-FITC positive cells for U-87 MG and MDA-MB-231 spheroids. Reported values are means of 3 replicates ± s.d.

7. References

1. Coley, W. B. II. Contribution to the Knowledge of Sarcoma. *Ann Surg* **14**, 199 (1891).
2. Adams, J. L., Smothers, J., Srinivasan, R. & Hoos, A. Big opportunities for small molecules in immuno-oncology. *Nat Rev Drug Discov* **14**, 603–622 (2015).
3. Decker, W. K. *et al.* Cancer immunotherapy: Historical perspective of a clinical revolution and emerging preclinical animal models. *Front Immunol* **8**, (2017).
4. Dobosz, P. & Dzieciątkowski, T. The Intriguing History of Cancer Immunotherapy. *Front Immunol* **10**, (2019).
5. Oiseth, S. J. & Aziz, M. S. Cancer immunotherapy: a brief review of the history, possibilities, and challenges ahead. *J Cancer Metastasis Treat* **3**, 250–61 (2017).
6. Schreiber, R. D., Old, L. J. & Smyth, M. J. Cancer immunoediting: Integrating immunity's roles in cancer suppression and promotion. *Science (1979)* **331**, 1565–1570 (2011).
7. Smyth, M. J., Dunn, G. P. & Schreiber, R. D. Cancer Immunosurveillance and Immunoediting: The Roles of Immunity in Suppressing Tumor Development and Shaping Tumor Immunogenicity. *Adv Immunol* **90**, 1–50 (2006).
8. Zhang, Y. & Zhang, Z. The history and advances in cancer immunotherapy: understanding the characteristics of tumor-infiltrating immune cells and their therapeutic implications. *Cell Mol Immunol* **17**, 807–821 (2020).

9. Abbott, M. & Ustoyev, Y. Cancer and the Immune System: The History and Background of Immunotherapy. *Semin Oncol Nurs* **35**, 150923 (2019).
10. Russell, S. J., Peng, K. W. & Bell, J. C. Oncolytic virotherapy. *Nat Biotechnol* **30**, 658–670 (2012).
11. Kaur, K. & Khatik, G. L. Cancer Immunotherapy: An Effective Tool in Cancer Control and Treatment. *Curr Cancer Ther Rev* **16**, 62–69 (2019).
12. Andtbacka, R. H. I. *et al.* Talimogene Laherparepvec Improves Durable Response Rate in Patients With Advanced Melanoma. *J Clin Oncol* **33**, 2780–2788 (2015).
13. Melief, C. J. M., van Hall, T., Arens, R., Ossendorp, F. & van der Burg, S. H. Therapeutic cancer vaccines. *J Clin Invest* **125**, 3401–3412 (2015).
14. Farkona, S., Diamandis, E. P. & Blasutig, I. M. Cancer immunotherapy: The beginning of the end of cancer? *BMC Med* **14**, 1–18 (2016).
15. Sengsayadeth, S., Savani, B. N., Oluwole, O. & Dholaria, B. Overview of approved CAR-T therapies, ongoing clinical trials, and its impact on clinical practice. *EJHaem* **3**, 6–10 (2022).
16. Sterner, R. C. & Sterner, R. M. CAR-T cell therapy: current limitations and potential strategies. *Blood Cancer Journal 2021 11:4* **11**, 1–11 (2021).
17. Zahavi, D. & Weiner, L. Monoclonal Antibodies in Cancer Therapy. *Antibodies 2020, Vol. 9, Page 34* **9**, 34 (2020).
18. Papaioannou, N. E., Beniata, O. v, Vitsos, P., Tsitsilonis, O. & Samara, P. Harnessing the immune system to improve cancer therapy. *Ann Transl Med* **4**, 261 (2016).
19. Plosker, G. L. & Figgitt, D. P. Rituximab: A review of its use in non-Hodgkin's lymphoma and chronic lymphocytic leukaemia. *Drugs* **63**, 803–843 (2003).

20. May, C., Sapra, P. & Gerber, H. P. Advances in bispecific biotherapeutics for the treatment of cancer. *Biochem Pharmacol* **84**, 1105–1112 (2012).
21. Narvekar, A., Pardeshi, A., Jain, R. & Dandekar, P. ADCC enhancement: A conundrum or a boon to mAb therapy? *Biologicals* **79**, (2022).
22. Dixon, K. J., Wu, J. & Walcheck, B. Engineering Anti-Tumor Monoclonal Antibodies and Fc Receptors to Enhance ADCC by Human NK Cells. *Cancers 2021, Vol. 13, Page 312* **13**, 312 (2021).
23. Weiner, L. M., Zahavi, D., Aldeghaither, D. & O'connell, A. Enhancing antibody-dependent cell-mediated cytotoxicity: a strategy for improving antibody-based immunotherapy. *Antib Ther* **1**, (2018).
24. Wang, W., Erbe, A. K., Hank, J. A., Morris, Z. S. & Sondel, P. M. NK cell-mediated antibody-dependent cellular cytotoxicity in cancer immunotherapy. *Front Immunol* **6**, (2015).
25. Blick, S. K. A. & Scott, L. J. Cetuximab: a review of its use in squamous cell carcinoma of the head and neck and metastatic colorectal cancer. *Drugs* **67**, 2585–2607 (2007).
26. lo Nigro, C. *et al.* Evaluation of antibody-dependent cell-mediated cytotoxicity activity and cetuximab response in KRAS wild-type metastatic colorectal cancer patients. *World J Gastrointest Oncol* **8**, 222–230 (2016).
27. Medikonda, R., Dunn, G., Rahman, M., Fecci, P. & Lim, M. A review of glioblastoma immunotherapy. *J Neurooncol* **151**, 41–53 (2021).
28. Yu, M. W. & Quail, D. F. Immunotherapy for Glioblastoma: Current Progress and Challenge. *Front Immunol* **12**, (2021).
29. Keenan, T. E. & Tolaney, S. M. Role of Immunotherapy in Triple-Negative Breast Cancer. *J Natl Compr Canc Netw* **18**, 479–489 (2020).

30. Zhu, Y., Zhu, X., Tang, C., Guan, X. & Zhang, W. Progress and challenges of immunotherapy in triple-negative breast cancer. *Biochim Biophys Acta Rev Cancer* **1876**, (2021).

31. Narayan, P. *et al.* FDA Approval Summary: Atezolizumab plus Paclitaxel Protein-bound for the Treatment of Patients with Advanced or Metastatic TNBC Whose Tumors Express PD-L1. *Clinical Cancer Research* **26**, 2284–2289 (2020).

32. Białkowska, K., Komorowski, P., Bryszewska, M. & Miłowska, K. Spheroids as a Type of Three-Dimensional Cell Cultures-Examples of Methods of Preparation and the Most Important Application. *Int J Mol Sci* **21**, 1–17 (2020).

33. Foglietta, F., Serpe, L. & Canaparo, R. The Effective Combination between 3D Cancer Models and Stimuli-Responsive Nanoscale Drug Delivery Systems. *Cells* **10**, (2021).

34. Langhans, S. A. Three-dimensional in vitro cell culture models in drug discovery and drug repositioning. *Front Pharmacol* **9**, (2018).

35. Boix-Montesinos, P., Soriano-Teruel, P. M., Armiñán, A., Orzáez, M. & Vicent, M. J. The past, present, and future of breast cancer models for nanomedicine development. *Adv Drug Deliv Rev* **173**, 306–330 (2021).

36. Pinto, B., Henriques, A. C., Silva, P. M. A. & Bousbaa, H. Three-Dimensional Spheroids as In Vitro Preclinical Models for Cancer Research. *Pharmaceutics 2020, Vol. 12, Page 1186* **12**, 1186 (2020).

37. Rossi, G., Manfrin, A. & Lutolf, M. P. Progress and potential in organoid research. *Nature Reviews Genetics 2018 19:11* **19**, 671–687 (2018).

38. Rizzuto, M. A. *et al.* H-Ferritin nanoparticle-mediated delivery of antibodies across a BBB in vitro model for treatment of brain malignancies. *Biomater Sci* **9**, 2032–2042 (2021).

39. Bellini, M. *et al.* Protein nanocages for self-triggered nuclear delivery of DNA-targeted chemotherapeutics in Cancer Cells. *Journal of Controlled Release* **196**, 184–196 (2014).

40. Falvo, E. *et al.* Antibody-drug conjugates: targeting melanoma with cisplatin encapsulated in protein-cage nanoparticles based on human ferritin. *Nanoscale* **5**, 12278–12285 (2013).

41. Wilkins, M. R. *et al.* Protein identification and analysis tools in the ExPASy server. *Methods Mol Biol* **112**, 531–552 (1999).

42. Lucigen Corporation ClearColi BL21(DE3) Electrocompetent Cells, 12 Rxns | Fisher Scientific. https://www.fishersci.com/shop/products/cleancol-bl21-de3-electrocomp/NC0487614.

43. Wilding, K. M. *et al.* Endotoxin-Free E. coli-Based Cell-Free Protein Synthesis: Pre-Expression Endotoxin Removal Approaches for on-Demand Cancer Therapeutic Production. *Biotechnol J* **14**, (2019).

44. Mamat, U. *et al.* Detoxifying Escherichia coli for endotoxin-free production of recombinant proteins. *Microb Cell Fact* **14**, 57 (2015).

45. Silva, F. *et al.* Combined Method to Remove Endotoxins from Protein Nanocages for Drug Delivery Applications: The Case of Human Ferritin. *Pharmaceutics* **13**, 1–18 (2021).

46. Rogers, L. M., Veeramani, S. & Weiner, G. J. Complement in monoclonal antibody therapy of cancer. *Immunol Res* **59**, 203–210 (2014).

47. Mellor, J. D., Brown, M. P., Irving, H. R., Zalcberg, J. R. & Dobrovic, A. A critical review of the role of Fc gamma receptor polymorphisms in the response to monoclonal antibodies in cancer. *J Hematol Oncol* **6**, (2013).

48. Monteverde, M. *et al.* The relevance of ADCC for EGFR targeting: A review of the literature and a clinically-applicable method of assessment in patients. *Crit Rev Oncol Hematol* **95**, 179–190 (2015).

49. Hsu, H. C. *et al.* Mutations of KRAS/NRAS/BRAF predict cetuximab resistance in metastatic colorectal cancer patients. *Oncotarget* **7**, 22257–22270 (2016).

50. Colombo, M. *et al.* Half-Chain Cetuximab Nanoconjugates Allow Multitarget Therapy of Triple Negative Breast Cancer. *Bioconjug Chem* **29**, 3817–3832 (2018).

51. Metkar, S. S. *et al.* Granzyme B activates procaspase-3 which signals a mitochondrial amplification loop for maximal apoptosis. *J Cell Biol* **160**, 875–885 (2003).

52. Teillaud, J.-L. Antibody-dependent Cellular Cytotoxicity (ADCC). *eLS* (2012).

53. Liu, S. *et al.* NK cell-based cancer immunotherapy: from basic biology to clinical development. *Journal of Hematology & Oncology 2021 14:1* **14**, 1–17 (2021).

54. Kumar, S. Natural killer cell cytotoxicity and its regulation by inhibitory receptors. *Immunology* **154**, 383 (2018).

55. Ho Park, M. *et al.* Effects of ADAM10 and ADAM17 Inhibitors on Natural Killer Cell Expansion and Antibody-dependent Cellular Cytotoxicity Against Breast Cancer Cells In Vitro. *Anticancer Res* **37**, 5507–5513 (2017).

56. Mazzucchelli, S. *et al.* Nanometronomic treatment of 4T1 breast cancer with nanocaged doxorubicin prevents drug resistance and circumvents cardiotoxicity. *Oncotarget* **8**, 8383–8396 (2016).

CHAPTER TWO

Cisplatin loading inside HFn: a two methods comparison

1. Introduction

1.1 Cisplatin

Cisplatin or (SP-4-2)-diamminedichloridoplatinum(II) is one of the first metal-based chemotherapeutic drugs. In fact, it was first approved by the US Food and Drug Administration (FDA) for testicular and ovarian cancer in 1978.[1] As shown in Fig1, it is a metallic (platinum) coordination compound with a square planar geometry. Platinum ions are surrounded by four ligands: amine ligands on the left forming stronger interactions with the platinum ion, and the chloride ligands on the right forming leaving groups allowing the platinum ion to form bonds with DNA bases.[2]

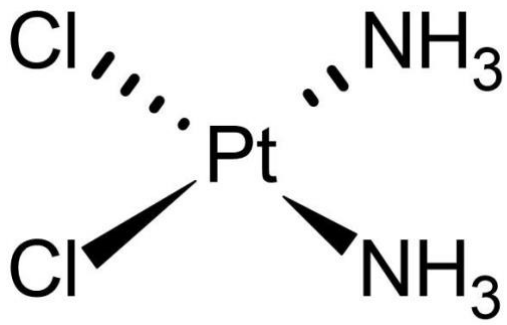

Figure 1: cisplatin chemical structure

Cisplatin is clinically proven to combat different types of cancers including sarcomas, cancers of soft tissue, bones, muscles, and blood vessels, and breast cancer. Cisplatin is also considered an alternative therapy for the management of several solid tumors, including gastric, liver and brain carcinomas.[3] It is administered intravenously to the patients as a sterile saline solution, but it is reported that a very little amount of cisplatin enters the tumor cells by passive

diffusion through the plasma membrane or after the uptake mediated by the copper transporter CTR1.[4] Once cisplatin enters into the cell it becomes activated by replacing one of the chloride ligands into water ligand. This hydrolyzed product is a potent electrophile that can react, for example, with sulfhydryl groups on proteins and nitrogen donor atoms on nucleic acids. This binding can lead to DNA damage in cancer cells, blocking cell division and resulting in apoptotic cell death. Cisplatin cytotoxic effect is the result of several molecular mechanisms of action such as induction of oxidative stress as characterized by reactive oxygen species production and lipid peroxidation, induction of p53 signaling and cell cycle arrest, down-regulation of proto-oncogenes and anti-apoptotic proteins, and activation of both intrinsic and extrinsic pathways of apoptosis.[2,5]

Even if cisplatin is very successful for the treatment of certain type of cancer, such as testicular and ovarian, it induces a large number of toxic side effects such as myelotoxicity, gastrointestinal toxicity, neurotoxicity, ototoxicity, cardiotoxicity and nephrotoxicity.[6] These side effects are determined by a nonselective distribution of the drug between normal and tumor tissue which results to be dose dependent. Moreover, the therapeutic ratio is further compressed by tumors that display intrinsic cisplatin resistance or acquire resistance over the course of treatment. [7]

To overcome these limitations, a wide range of nanoparticles has been tested as a drug delivery system for cisplatin to promote accumulation preferentially in cancer cells and thereby reduce adverse side effects. A variety of carriers, including organic (polymeric micelles, dendrimers, and liposomes) inorganic (ferromagnetic NPs, gold NPs, and mesoporous silica NPs), and hybrid NPs have been adapted to facilitate the delivery of platinum-based drugs.[8] Among them,

many liposomal-based nano-formulations are at the stage of clinical trials as summarized in Table 1. For example, Lipoplatin (Regulon, Inc.), a liposome-based platinum formulation, is now under phase III clinical trial to be used for the treatment of pancreatic cancer. This formulation has proved to reduce the overall systemic toxicity compared to cisplatin, thus allowing a higher dose to be administered.[9]

Table 1: Summary of cisplatin nano-formulations under clinical trials in 2019. Reproduced with permission from the corresponding paper.[9]

Brand name	Formulation type	Administration route	Manufacturing company	Therapeutic use	Clinical trial phase
Lipoplatin	PEGylated liposome	i.v.	Regulon Inc.	Various cancer	III
SPI-077	PEGylated liposome	i.v.	Alza Corporation	Head, neck lung cancer	II
NC-6004 Nanoplatin™	Polymeric Micelles	i.v.	Nano Carrier Co. Ltd. Japan	Advance or metastatic pancreatic cancer	II
L-NDDP Aroplatin™	Liposomes	i.v.	New York University School of Medicine, USA	Malignant pleural mesothelioma	II

1.2 Drug loading inside HFn

As previously mentioned, apoferritin has an inner cavity that has been exploited for the encapsulation of different small-molecule compounds such as doxorubicin, curcumin, paclitaxel mitoxantrone and also platinum-based drugs.[10]

Cisplatin encapsulation inside ferritin was first reported in 2007 by Guo and co-workers who exploited the ability of ferritin to disassemble and reassemble in response to pH alteration.[11] Ferritin subunits are able to disassemble at extreme (low or high) pH and re-assemble with a shape memory fashion when the environmental conditions return to neutral pH.[12] If the molecules of interest are added to the buffer during this process, they will remain entrapped into the cavity at the same time as when the protein will return to its normal quaternary structure. Ferritin nanocages are also disassembled by urea and reassembled following stepwise urea removal.[13] In the past ten years drug loading methods based on dissociation have become the preferred. For example, Huang and his group successfully encapsulate cisplatin inside apoferritin dissociating protein subunits at pH 13 and then reconstituting them at pH 7.[14]

The main problem of this protocol is that extreme pH values can damage both the protein cage and the cargo, significantly reducing the efficiency of the encapsulation process. This process, in fact, is not fully reversible, leading to the formation of soluble aggregates and insoluble precipitates. The main drawback of the pH method is that only 50–60% of disassociated protein molecules could reassemble into a properly folded protein nanocage.[15] However the disassembly/reassembly method allows the encapsulation inside ferritin of large molecule compounds which can't be loaded otherwise.

To overcome these limitations, in recent years researchers have set their sights on drug loading while maintaining the ferritin cage structure. Recently a natural drug entry channel on the surface of human HFn nanocages has been identified whose diameter can be expanded to more than 1.0 nm *via* thermal fluctuation allowing the small-molecule drugs to enter the cavity of ferritin across the opened channel, through passive diffusion.[10,16] To date doxorubicin, epirubicin,

cisplatin and oxaliplatin have been loaded into HFn nanocages exploiting this method. For example, Jiang and colleagues developed a methodology that is able to provide high loading of DOX and high recovery of ferritin by incubating DOX with HFn at 60 °C for 4 h.[17]

Lastly, when ferritin is incubated with a metal ion source since its inner cavity has a strong negative charge, positively charged metal ions such as gold and copper can easily migrate through the pores of ferritin nanocages and accumulate in the cavity.[18] Molecular cargoes can be complexed with these metal ions to be loaded inside ferritin (Fig2).[19]

1) Drug loading through dissociation and reconstruction

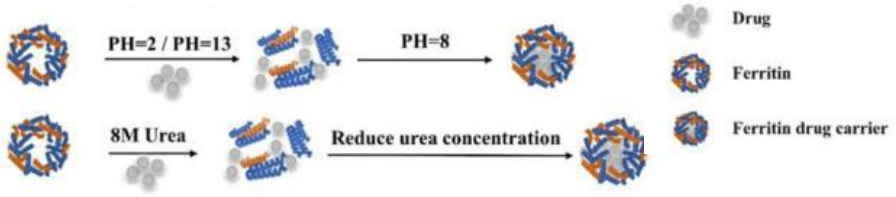

2) Drug loading through high temperature



3) Drug loading through hydrophilic and hydrophobic channels



Figure 2: Biochemical strategies used to load different cargoes into ferritin nanoparticles. 1) pH or urea-mediated disassembly–reassembly methodology; 2) thermal fluctuation loading strategy; 3) passive diffusion loading strategy. Reproduced with permission from the corresponding paper.[18]

2. Aim of the project

Cisplatin has been used for more than three decades in standard chemotherapy regimens. However, its clinical application has been largely restricted by its high toxicity to healthy cells.[6] To overcome these limitations, a wide range of nanoparticles has been tested as a drug delivery system for cisplatin to promote accumulation preferentially in cancer cells and thereby reduce adverse side effects.[8] Among them, we chose to use human H-ferritin nanoparticles exploiting two characteristics of this protein: 1) the inner cavity of H-ferritin can be easily used for the loading of a wide range of molecules; 2) HFn is expected to recognize tumor cells sensitively and selectively by exploiting its binding capability to transferrin receptor 1, overexpressed on the surface of the majority of solid tumors.[10]

The aim of this work is to compare two general encapsulation methods described in the literature for loading drugs inside the HFn cavity to define an optimal strategy for cisplatin delivery. The first method takes advantage of the pH-dependent disassembly-reassembly of HFn, while the second one is based on the presence of a natural entry channel on the surface of HFn whose diameter can be expanded *via* thermal fluctuation allowing the small-molecule drugs to enter the inner cavity of the protein.

3. Materials and methods

Synthesis of HFn(CISP)

pH-based cisplatin loading method: a solution of HFn 0.5 mg mL^{-1} in 0.15 M of NaCl was prepared and then cisplatin was added maintaining a 1:300 molar ratio between HFn and cisplatin. The pH of the reaction mix was measured and then slowly adjusted to 13 by 1 M of NaOH and maintained for about 15 minutes to fully disassemble the HFn nanocages. Then the pH value was slowly adjusted to 7.5 using 0.1 M HCl and the resulting solution was stirred at 4 °C for 3 hours. To eliminate the free cisplatin from the solution, the sample was centrifuged with a centrifugal filter unit (100 kDa MWCO, Amicon, Millipore Corporate) and then passed through a size exclusion chromatography column (Zeba™ Spin Desalting Column, 7 kDa MWCO, Thermo Fisher Scientific, MA, USA) buffered with phosphate buffer saline (PBS), pH 7.4.

channel-based cisplatin loading method: cisplatin was added to a HFn solution (1 mg mL^{-1} in phosphate buffer pH 5.8 or Tris HCl 20 mM pH 8) maintaining either 1:300 or 1:600 molar ratio between HFn and cisplatin. The reaction mix was incubated at 40 °C or at 60 °C for 1 hour or at 60 °C for 4 hours. The solution was then centrifugated at 10,000xg for 10 minutes to separate the supernatant. Finally, the free cisplatin was removed from the supernatant by a size exclusion chromatography column (Zeba™ Spin Desalting Column, 7 kDa MWCO, Thermo Fisher Scientific, MA, USA) to get the purified Channel-HFn(CISP) in PBS buffer.

Characterization of HFn(CISP)

The protein was quantified by both measuring absorbance at 280 nm and using the Coomassie Plus Protein Assay Reagent (Thermo Fisher Scientific, MA, USA). The correct native structure was determined by native PAGE using 6% (v/v) polyacrylamide gels colored with Coomassie Blue staining. The hydrodynamic diameter was evaluated by dynamic light scattering (DLS) analysis using a Zetasizer Nano ZS ZEN3600 from Malvern Instruments Ltd (Worcestershire, UK). The protein was diluted in PBS, 0.5 mg mL^{-1}. The measurement occurred at 25 °C, operating at 4 mW of a HeNe 633 nm laser with a protein refractive index of 1.45, using a scattering angle of 90°. A disposable cuvette with 1 cm optical path length was used for the measurements. The results were expressed as mean ± standard deviation (SD) of three measurements.

To quantify the amount of cisplatin in the solutions, inductively coupled plasma-mass spectrometry (ICP-MS, Elan DRC II, Perkin Elmer) was used, applying the external calibration quantitative method. A three-point calibration curve was made for all measurements against Pt-containing solutions prepared by serial dilution of a certified reference standard. Each sample was diluted 1000 times in distilled water. The results are expressed as mean ± SD. Protein yield was calculated according to the following formula: yield = [weight of final protein /total weight of added protein] × 100%.

4. Results

Loading of cisplatin inside HFn

Ferritin is a round shape protein made by 24 self-assembling subunits that create a hollow cage-like structure able to internalize up to 4500 Fe(II) atoms. Producing a recombinant ferritin protein without the metallic core inside (apoferritin) makes it possible to load a wide range of active molecules inside the ferritin's cavity, acting either as MRI agents or as drug delivery systems for the diagnosis and treatment of tumors.[20] Among them, drugs based on metals, such as cisplatin, can be easily encapsulated into the ferritin shell. Cisplatin has been used for more than three decades in standard chemotherapy regimens either as a single therapeutic modality or in combination with other cytotoxic agents or radiotherapy.[21] However, heart disease and kidney disorders are among its side effects, and thus its clinical application has been largely restricted by high toxicity and tumor resistance.[22] The encapsulation inside HFn reduces cisplatin toxicity to healthy cells significantly, while maintaining its effects on cancer cells.

As mentioned above, the main methods used to encapsulate payloads into the ferritin protein cage are high-temperature loading, passive diffusion, protein structure disruption through denaturing buffer, and pH-mediated disassembly and reassembly, which exhibit varying degrees of success depending on the type of drug.[18] We focused on the optimization of cisplatin encapsulation *via* high temperature and pH-mediated loading.

pH-based cisplatin loading method

Ferritin can be disassembled by altering the buffer pH to extremely acidic or basic. However, the single subunits obtained maintain the ability to reconstitute the entire protein once the pH is restored to a neutral value. If this process is conducted in the presence of a drug in the reaction mix, a substantial amount of this active molecule will be entrapped inside the ferritin's cavity.

Considering that the pH-based encapsulation is studied and used since 2005 when Simsek and Kilic loaded doxorubicin inside a horse spleen apoferritin, we decide to follow an established protocol for cisplatin encapsulation.[23] Briefly, cisplatin was added to a HFn solution (0.5 mg mL^{-1} in 0.15 M of NaCl) maintaining a 1:300 molar ratio between HFn and cisplatin. The pH of the reaction mix was slowly adjusted to 13 by 1 M of NaOH and maintained for about 15 min. When the dissociation of HFn was completed, the pH value was increased up to 7.5 using 0.1 M HCl and the resulting solution was stirred at 4°C for 3 hours in order to give HFn time to reassemble encapsulating cisplatin inside the inner cavity. To eliminate cisplatin excess from the solution, the supernatant was centrifuged with a centrifugal filter unit (Amicon, 100 kDa MWCO) and then passed through a size exclusion chromatography column (Zeba™ Spin Desalting Column) changing the buffer to PBS to obtain pH-HFn(CISP) (Fig3).

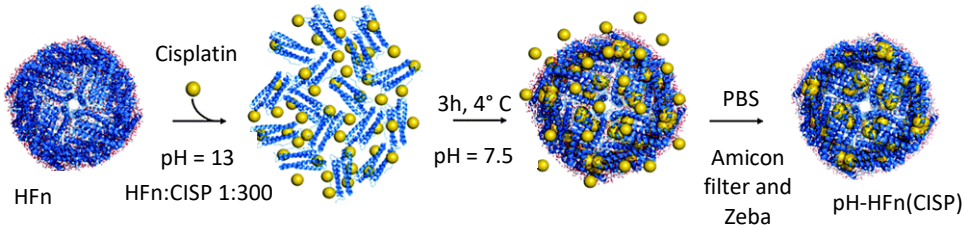

Figure 3: pH-HFn(CISP) synthesis reaction. HFn was dissociated at pH 13 using NaOH 1 M in the presence of cisplatin and then reconstituted at pH 7.5 using HCl 0.1 M. After

3 h of incubation, the steps of purification eliminated the undesired cisplatin outside the shell of the protein. Reproduced and modified with permission from the corresponding paper.[24]

The protein recovery efficiency was very different comparing the encapsulation reactions that we performed (Table 2). These results can be explained considering that at pH > 12 HFn is completely dissociated which often causes the formation of soluble aggregates and insoluble precipitates that damage the reassembly and recovery of HFn. For this reason, this process required accurate pH control during the encapsulation reaction. However, these recovery rates are in line with what was found in the literature.[25,26]

Table 2: Comparison of different HFn recovery rates and cisplatin encapsulation rates obtained with the pH-based method.

Reaction	Starting HFn (mg)	Starting CISP:HFn	HFn recovery rate (%)	Final CISP molecules per HFn
1	5	300:1	36.2	25.6
2	5	300:1	28	30.0
3	15	300:1	59.8	11.8
4	5	300:1	50.6	15.2
5	5	300:1	56.7	15.1
6	5	300:1	46.5	14.9
7	5	300:1	36.7	13.8

The amount of cisplatin loaded inside HFn was quantified by ICP-MS analysis that measure the amount of platinum present in the sample. The cisplatin:HFn molar ratio was estimated as 18.1 (± 6.9):1, a result that is in accordance with literature data that used the same encapsulation procedure.[11,14]

High temperature cisplatin loading strategy

Recently, a natural drug entry channel on the surface of the human HFn nanocage has been identified that could be opened by heating the system temperature, allowing the small-molecule drugs to enter the cavity of ferritin across the opened channel through passive diffusion. This channel-based loading strategy avoids denaturation of HFn nanocage and aims to obtain a higher drug loading efficiency and increase the HFn recovery rate.

Following the protocol described by Inoue et al., cisplatin was added to an HFn solution (1 mg mL^{-1}) maintaining a 1:300 molar ratio between HFn and cisplatin. As buffer, we chose to use phosphate at pH 5.8 because it was closer to the pKa of cisplatin (pKa = 5.06). According to the authors of the article, a pH closer to the pKa of the drug chosen for encapsulation promotes the deposition of the molecule inside the ferritin cavity.[16] The reaction mix was incubated at 40 °C or at 60 °C for 1 hour to let the ferritin channel become more flexible and cisplatin enter into the inner cavity. To eliminate cisplatin excess from the solution, the supernatant was passed through a size exclusion chromatography column (Zeba™ Spin Desalting Column) changing the buffer to PBS to obtain channel-HFn(CISP) (Fig4).

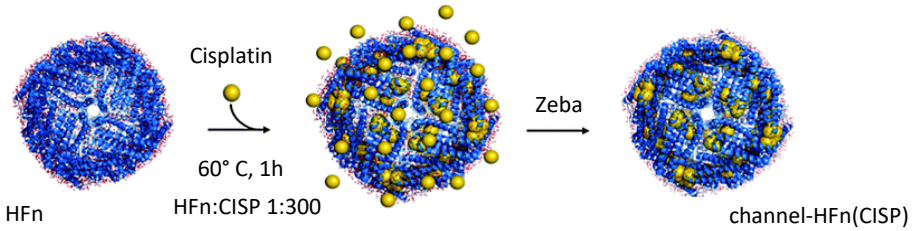

Figure 4: channel-HFn(CISP) synthesis reaction. A mix of HFn and cisplatin in phosphate buffer was left for 1 h at 60 °C. Then the undesired cisplatin outside the shell of the protein was removed using a size exclusion chromatography column. Reproduced and modified with permission from the corresponding paper.[24]

The protein recovery efficiency was 66.8% for the reaction conducted at 40 °C, while it slightly decreased to 53.6% (± 8.6%) when the temperature was set at 60 °C. The amount of cisplatin loaded inside HFn was quantified by ICP-MS analysis. The cisplatin:HFn molar ratio was estimated as 27.57:1 for the 40 °C reaction and as 63.77 (± 10.2):1 for the 60 °C reactions. Taken together these data show that the encapsulation rate increases with temperature, while the recovery efficiency shows the opposite behavior.

Table 3: Comparison of different HFn recovery rates and cisplatin encapsulation rates obtained with the channel-based method.

Reaction	Starting HFn (mg)	Starting CISP:HFn	Temperature	HFn recovery rate (%)	Final CISP molecules per HFn
1	5	300:1	60 °C	47.5	71
2	3.5	300:1	60 °C	59.7	56.53
3	3.5	300:1	40 °C	66.8	25.57

Comparing the results that we obtained with these two encapsulation methods, we found that channel-HFn(CISP) contained more than 60 cisplatin molecules per HFn protein which was significantly more than those of pH-HFn(CISP) (~20). Moreover, the HFn recovery rate of channel-HFn(CISP) (~50%) was also higher than those of pH-HFn(CISP) (~40%). However, looking at the stability of the HFn preparation, after one week at 4 °C in the case of channel-HFn(CISP) there was evidence of protein aggregation and precipitation that led to the loss of more than 50% of HFn (Fig5). Those aggregates were absent in the ph-HFn(CISP) preparation.

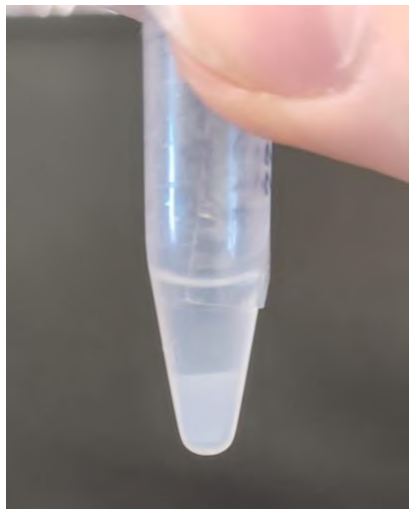

Figure 5: protein precipitation and aggregation after encapsulation of cisplatin inside HFn exploiting the high temperature-based method.

To evaluate the reasons for protein precipitation we repeated the same reaction protocol but without cisplatin. We left HFn (1 mg mL^{-1}) in phosphate buffer for 1 hour at 60 °C and then we changed the buffer to PBS using a size exclusion chromatography column. HFn didn't show any signs of precipitation even after

one month at 4 °C. Excluding temperature, the reasons for the instability can be the incubation time and the pH chosen for the reaction. After 1h of incubation, the drug entry channels could still be in a close state which led to the absorption of cisplatin on the surface of HFn which promoted the aggregation. Moreover, a pH of 5.8 is very close to the isoelectric point of HFn (5.4-5.5) causing a decrease in the solubility of the protein. For these reasons, we decide to follow a different encapsulation protocol.[17] Briefly, 1.5 mg of cisplatin was added to 2 mg mL^{-1} HFn solution in 2 mL of 20 mM Tris-HCl buffer (pH = 8). The mixture was incubated at 60 °C for 4 hours, then centrifugated at 10,000xg for 10 minutes to separate the supernatant. A size exclusion chromatography column was used to remove free cisplatin from the supernatant and to get the purified HFn(CISP) complex in PBS buffer. The protein recovery efficiency was around 90% but we noticed that the absorbance peak at 280 nm of channel-HFn(CISP) was different from the one of pH-HFn(CISP) and HFn alone (Fig6).

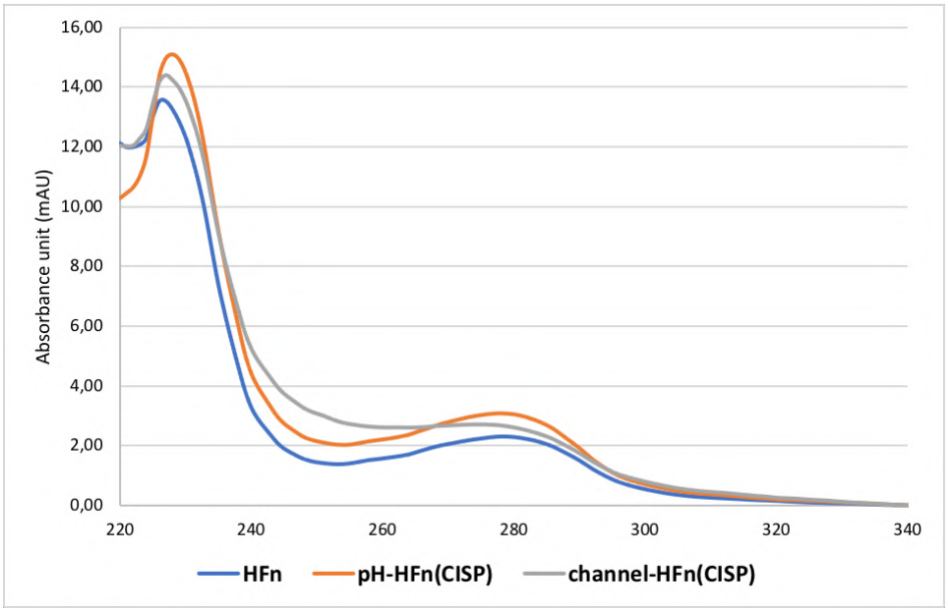

Figure 6: absorbance spectra of HFn, pH-HFn(CISP) and channel-HFn(CISP).

We repeated the same reaction twice and stored all the samples at -20 °C. Once again, when we defrosted them to quantify the encapsulated cisplatin there was evidence of protein aggregation and precipitation that led to the loss of more than 50% of HFn. In order to try to reduce HFn aggregation, we repeated the same reaction but, after the size exclusion chromatography, we left the sample in 20 mM Tris-HCl buffer and we stored it at 4°C. Also in this case we found out that the absorbance peak at 280 nm was different from the one of HFn and pH-HFn(CISP) as shown in the figure below (Fig7).

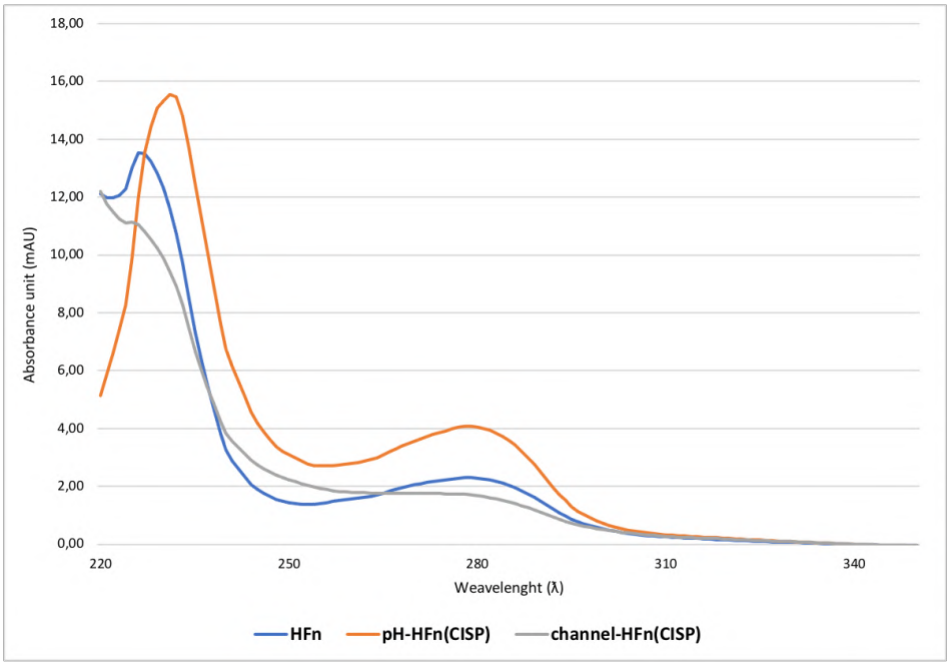

Figure 7: absorbance spectra of HFn, pH-HFn(CISP) and channel-HFn(CISP).

HFn(CISP) characterization

To verify that HFn maintained its original molecular weight even after the encapsulation procedure, we loaded the sample in a Native gel electrophoresis

(Fig8). As shown in figure 8 pH-HFn(CISP) retained the molecular weight of the standard HFn while channel-HFn(CISP) failed to maintain its structure which is in line with the aggregates that we saw and with the absorbance profile.

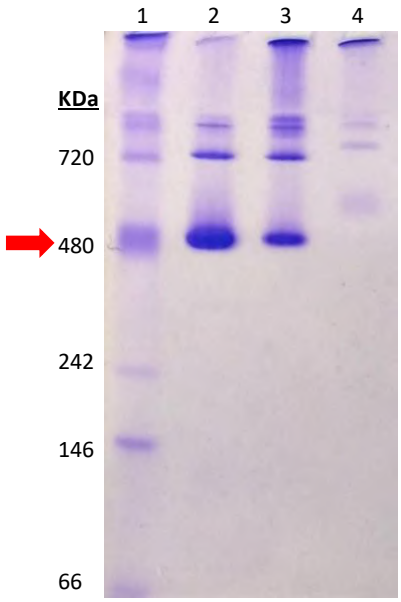

Figure 8: Native polyacrylamide gel 6% (v/v). Samples have been loaded in the following order: 1) marker, 2) HFn, 3) pH-HFn(CISP) and 4) channel-HFn(CISP).

The hydrodynamic diameter of pH-HFn(CISP) assessed by dynamic light scattering (DLS) analysis (10.9 ± 3.0 nm, Fig9) was consistent with the size reported for native ferritin (~12 nm).[27] On the contrary, the hydrodynamic diameter of channel-HFn(CISP) was 62.7 ± 14.4 nm which revealed the presence of proteins aggregates.

A)

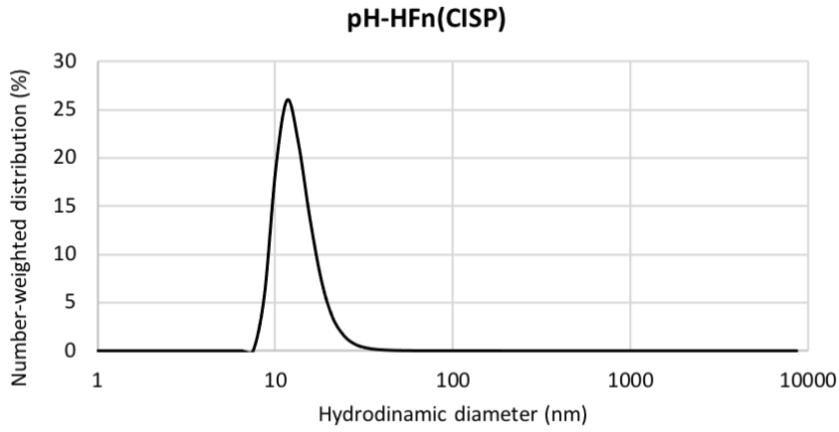

B)

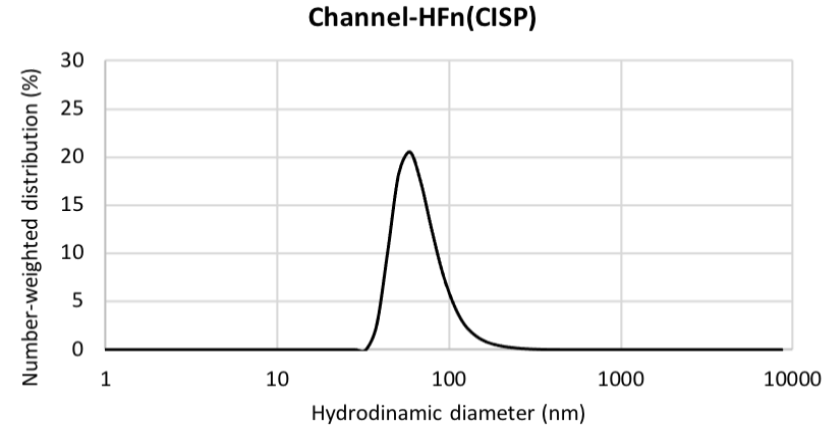

Figure 9: DLS analysis A) pH-HFn(CISP) size distribution detected by DLS analysis and a representative sample image. B) channel-HFn(CISP) size distribution detected by DLS analysis and a representative sample image.

5. Discussion

In this study, we compared two different methods to load cisplatin inside the HFn cavity. The first one is based on the ability of HFn to disassemble and reassemble after pH variation. HFn has pH stability in the 3 to 12 range but, in an acidic (pH<3) or basic (pH>13) pH environment the ferritin nanocage progressively becomes disassembled into its subunits. If, during this process, a drug molecule is added to the solution, when pH is restored to neutral values HFn is reassembled encapsulating the drug inside its inner cavity. Exploiting this method, we were able to encapsulate up to 18 cisplatin molecules for each HFn, obtaining a protein recovery rate of around 45%. Both encapsulation efficiency and protein recovery rate are in line with what was found in the literature and reveal the limitations of this process: incomplete reassembly of the ferritin structure which results in the formation of permanent hole defects on the ferritin nanocages. However, the product obtained maintains the same absorbance profile, molecular weight and dimensions as an untreated HFn.

The second method is based on the presence of a 4-fold channel with an average diameter of 0.9 on the surface of ferritin. *Via* thermal fluctuation its diameter could be expanded to more than 1.0 nm opening the possibility to load small drugs inside ferritin cavity through passive diffusion. The reason for applying thermal treatment in encapsulation is based on the evidence that the whole ferritin structure is stable against heat treatment (80 °C) for 10 minutes, while the ferritin channels are sensitive to experimental conditions, such as temperature changes. Indeed, high thermal fluctuations induce changes in the secondary structure of HFn which indicate that, above 70 °C, ferritin structure may be partially unfolded. At 60 °C ferritin channels are expanded to their

maximum and this can cause local domains to be partially uncoiled which precedes the whole structure changes of the protein.[28] We inferred that after 1 h incubation at 60 °C degrees the protein aggregation derives from the close state of the drug entry channels which determines cisplatin absorption on the external surface of the protein. In the case of the second protocol, we can speculate that maintaining HFn and cisplatin for 4 hours at 60 °C causes irreversible protein structural changes that lead to protein aggregation and precipitation when the temperature returns to 20 °C. Indeed, the product obtained with this loading procedure failed to maintain ferritin molecular weight, absorbance profile and dimensions. This result disagrees with those found in the literature where such protocol was efficient both in terms of cisplatin encapsulation and protein recovery. For this reason, in the future, we're planning to repeat this reaction at different incubation times and temperatures while studying the changes in the absorbance peak and molecular weight of the HFn(CISP) product in order to find the optimal condition to reduce protein aggregation.

In the meantime, in order to proceed with the *in vitro* experiments, we chose to use ph-HFn(CISP). Evaluation of the transcriptomic profile of treated and untreated MDA-MB-231 samples and viability assays in 2D MDA-MB-231 model and in patient-derived organoids (PDO) are currently ongoing.

6. References

1. Ghosh, S. Cisplatin: The first metal based anticancer drug. *Bioorg Chem* **88**, (2019).
2. Dasari, S. & Bernard Tchounwou, P. Cisplatin in cancer therapy: molecular mechanisms of action. *Eur J Pharmacol* **740**, 364–378 (2014).
3. Schaake-Koning, C. *et al.* Effects of concomitant cisplatin and radiotherapy on inoperable non-small-cell lung cancer. *N Engl J Med* **326**, 524–530 (1992).
4. Fuertes, M. A., Castilla, J., Alonso, C. & Prez, J. M. Cisplatin Biochemical Mechanism of Action: From Cytotoxicity to Induction of Cell Death Through Interconnections Between Apoptotic and Necrotic Pathways. *Curr Med Chem* **10**, 257–266 (2012).
5. Eastman, A. The Mechanism of Action of Cisplatin: From Adducts to Apoptosis. in *Cisplatin* 111–134 (2006).
6. Tchounwou, P. B., Dasari, S., Noubissi, F. K., Ray, P. & Kumar, S. Advances in Our Understanding of the Molecular Mechanisms of Action of Cisplatin in Cancer Therapy. *J Exp Pharmacol* **13**, 303 (2021).
7. Köberle, B., Tomicic, M. T., Usanova, S. & Kaina, B. Cisplatin resistance: Preclinical findings and clinical implications. *Biochimica et Biophysica Acta (BBA) - Reviews on Cancer* **1806**, 172–182 (2010).
8. Duan, X., He, C., Kron, S. J. & Lin, W. Nanoparticle formulations of cisplatin for cancer therapy. *Wiley Interdiscip Rev Nanomed Nanobiotechnol* **8**, 776–791 (2016).

9. Farooq, M. A. *et al.* Recent progress in nanotechnology-based novel drug delivery systems in designing of cisplatin for cancer therapy: an overview. *Artif Cells Nanomed Biotechnol* **47**, 1674–1692 (2019).
10. Song, N. *et al.* Ferritin: A Multifunctional Nanoplatform for Biological Detection, Imaging Diagnosis, and Drug Delivery. *Acc Chem Res* **54**, 3313–3325 (2021).
11. Yang, Z. *et al.* Encapsulation of platinum anticancer drugs by apoferritin. *Chem Commun (Camb),* **33**, 3453–5 (2007).
12. Kim, M. *et al.* pH-dependent structures of ferritin and apoferritin in solution: disassembly and reassembly. *Biomacromolecules* **12**, 1629–1640 (2011).
13. Liang, M. *et al.* H-ferritin-nanocaged doxorubicin nanoparticles specifically target and kill tumors with a single-dose injection. *Proc Natl Acad Sci U S A* **111**, 14900–14905 (2014).
14. Ji, X. T., Huang, L. & Huang, H. Q. Construction of nanometer cisplatin core-ferritin (NCC-F) and proteomic analysis of gastric cancer cell apoptosis induced with cisplatin released from the NCC-F. *J Proteomics* **75**, 3145–3157 (2012).
15. Palombarini, F., Fabio, E. di, Boffi, A., Macone, A. & Bonamore, A. Ferritin Nanocages for Protein Delivery to Tumor Cells. *Molecules* **25**, (2020).
16. Inoue, I. *et al.* One-step construction of ferritin encapsulation drugs for cancer chemotherapy. *Nanoscale* **13**, 1875–1883 (2021).
17. Jiang, B. *et al.* A natural drug entry channel in the ferritin nanocage. *Nano Today* **35**, 100948 (2020).
18. Sun, X., Hong, Y., Gong, Y., Zheng, S. & Xie, D. Bioengineered ferritin nanocarriers for cancer therapy. *Int J Mol Sci* **22**, (2021).

19. Zhen, Z. *et al.* RGD-modified apoferritin nanoparticles for efficient drug delivery to tumors. *ACS Nano* **7**, 4830–4837 (2013).
20. Arosio, P., Ingrassia, R. & Cavadini, P. Ferritins: a family of molecules for iron storage, antioxidation and more. *Biochim Biophys Acta* **1790**, 589–599 (2009).
21. Xiaoyong, W. & Zijian, G. Targeting and delivery of platinum-based anticancer drugs. *Chem Soc Rev* **42**, 202–224 (2012).
22. He, J., Fan, K. & Yan, X. Ferritin drug carrier (FDC) for tumor targeting therapy. *J Control Release* **311–312**, 288–300 (2019).
23. Simsek, E. & Akif Kilic, M. Magic ferritin: A novel chemotherapeutic encapsulation bullet. *J Magn Magn Mater* **293**, 509–513 (2005).
24. Ferraro, G. *et al.* Gold-based drug encapsulation within a ferritin nanocage: X-ray structure and biological evaluation as a potential anticancer agent of the Auoxo3-loaded protein. *Chemical Communications* **52**, 9518–9521 (2016).
25. Palombarini, F., Fabio, E. di, Boffi, A., Macone, A. & Bonamore, A. Ferritin Nanocages for Protein Delivery to Tumor Cells. *Molecules* **25**, (2020).
26. Kilic, M. A., Ozlu, E. & Calis, S. A novel protein-based anticancer drug encapsulating nanosphere: Apoferritin-doxorubicin complex. *J Biomed Nanotechnol* **8**, 508–514 (2012).
27. Ford, G. C. *et al.* Ferritin: design and formation of an iron-storage molecule. *Philos Trans R Soc Lond B Biol Sci* **304**, 551–565 (1984).
28. Yang, R. *et al.* Thermally Induced Encapsulation of Food Nutrients into Phytoferritin through the Flexible Channels without Additives. *J Agric Food Chem* **65**, 9950–9955 (2017).

List of publications

1) Rizzuto, M. A., Dal Magro, R., **Barbieri, L.**, Pandolfi, L., Sguazzini-Viscontini, A., Truffi, M., Salvioni, L., Corsi, F., Colombo, M., Re, F., & Prosperi, D., (2021). H-Ferritin nanoparticle-mediated delivery of antibodies across a BBB in vitro model for treatment of brain malignancies. *Biomaterials science*, *9*(6), 2032–2042.

2) Salvioni, L., Testa, F., **Barbieri, L.**, Giustra, M., Bertolini, J. A., Tomaino, G., Tortora, P., Prosperi, D., & Colombo, M. (2022). Saporin Toxin Delivered by Engineered Colloidal Nanoparticles Is Strongly Effective against Cancer Cells. *Pharmaceutics*, *14*(7), 1517.

3) Rotem, R., Giustra, M., Arrigoni, F., Bertolini, J. A., Garbujo, S., Rizzuto, M. A., Salvioni, L., **Barbieri, L.**, Bertini, L., De Gioia, L., Colombo, M., & Prosperi, D. (2022). Conjugation of gold nanoparticles with multidentate surfactants for enhanced stability and biological properties. *Journal of materials chemistry. B*, *11*(1), 61–71.

4) Rotem, R., Bertolini, J. A., Salvioni, L., **Barbieri, L**., Rizzuto, M. A., Tinelli, V., Gori, A., Adams, S., Colombo, M., & Prosperi, D. (2023). Direct quantification of cytosolic delivery of drug nanocarriers using FlAsH-EDT2. *Nanomedicine: nanotechnology, biology, and medicine*, *47*, 102626.

5) Tomaino, G., Pantaleoni, C., Ami, D., Pellecchia, F., Dutriaux, A., **Barbieri, L.**, Garbujo, S., Natalello, A., Tortora, P., & Frascotti, G. (2023). Addressing Critical Issues Related to Storage and Stability of the Vault Nanoparticle Expressed and Purified from *Komagataella phaffi*. *International journal of molecular sciences*, *24*(4), 4214.

6) Del Nero, M., Colombo, A., Garbujo, S., Baioni, C., **Barbieri, L.**, Innocenti, M., Prosperi, D., Colombo, M., & Fiandra, L. (2023) Advanced cell culture models illuminate the interplay between mammary tumor cells and activated fibroblasts. *Cancers.* Article under review.